

The Pennsylvania State University  
The Graduate School

DESIGN, ANALYSIS, AND APPLICATIONS OF CELLULAR  
CONTACT-AIDED COMPLIANT MECHANISMS

A Dissertation in  
Mechanical Engineering  
by  
Vipul Mehta

© 2010 Vipul Mehta

Submitted in Partial Fulfillment  
of the Requirements  
for the Degree of

Doctor of Philosophy

August 2010

The dissertation of Vipul Mehta was reviewed and approved\* by the following:

Mary Frecker  
Professor of Mechanical Engineering  
Dissertation Co-Advisor, Co-chair of Committee

George A. Lesieutre  
Professor of Aerospace Engineering  
Dissertation Co-Advisor, Co-chair of Committee

James H. Adair  
Professor of Material Science and Engineering

Christopher D. Rahn  
Professor of Mechanical Engineering

Timothy W. Simpson  
Professor of Mechanical and Industrial Engineering

Karen A. Thole  
Professor of Mechanical Engineering  
Department Head of Mechanical and Nuclear Engineering

\*Signatures are on file in the Graduate School.

# Abstract

A new class of compliant mechanisms utilizing the benefits of cellular geometry and contact are addressed in this work. The design, analysis, fabrication and testing of such structures for high-strain and high-strength applications is the focus of the present research.

Cellular structures have relatively good strength-to-weight ratios. They also have a higher strain capability than solid structures. Contact during deformation reduces failure-causing bending stresses through stress relief, thereby enabling such cellular structures to be stretched more than the corresponding structures without contact. Both analytical and numerical models are developed to represent one specific mechanism. Several candidate materials are investigated for such mechanisms. Although the allowable strain of all these materials is small, the overall strain of the contact-aided cellular mechanisms is at least an order of magnitude greater than that of the constitutive material. Application of contact to different materials yields an improvement in the global strain capacity by more than 100% relative to cellular structures without contact. Experiments are conducted to validate the models, and good agreement is found. Size optimization is carried out to maximize the stress relief and the overall strain.

Two main applications are considered in the present work. One application consists of a morphing aircraft skin for adaptive structures. Different material models such as linearly elastic and multi-linear elastic are examined. For linearly elastic materials, contact-induced stress-relief is advantageous and for nonlinear elastic materials, reduction of transverse deflection due to contact is useful. The proposed contact-aided skin structure is compared with a cellular skin without contact. The contact mechanism helps to increase the morphing capacity while decreasing the structural mass. Using contact-aided cellular mechanisms, the global strain capability is increased by as much as 37%. For a fixed global strain, the optimum contact-aided structure is 15% lighter than an optimum non-contact structure.

Another application involves investigation of meso-scaled cellular structures. Two different materials are considered – nanoparticulate zirconia and particulate stainless steel. The lost mold rapid infiltration forming process is utilized to fabricate free standing cellular mechanisms. The analytical model is employed to address the tradeoffs between the manufacturing constraints and to design suitable contact-aided cellular mechanisms. A custom rig is developed to test these meso-scaled parts. Force displacement characteristics are experimentally obtained and compared against those found using the analytical model.

Topology optimization tools are applied to the design of compliant cellular mechanisms with and without a contact mechanism. A two-step procedure is developed. For cellular structures without contact, an inverse homogenization method is employed. The compliant mechanism is optimized to yield prescribed elasticity coefficients and achieve a large effective elastic strain. To implement a contact mechanism in the second step, the continuum model of a non-contact structure is converted into a frame model. Only the non-overlapping designs are investigated exhaustively for stress relief. A differential evolution optimizer is used to maximize the stress relief. Four cell topologies are found for different effective properties corresponding to different structural requirements. For each such topology, a contact mechanism is devised that demonstrates stress relief. One such topology resulted a stress relief as high as 36%.

# Table of Contents

<b>List of Figures</b>	<b>viii</b>
<b>List of Tables</b>	<b>xiii</b>
<b>Acknowledgments</b>	<b>xiv</b>
<b>Chapter 1 Introduction</b>	<b>1</b>
1.1 Background . . . . .	1
1.2 Motivation . . . . .	3
1.2.1 Stress Relief . . . . .	4
1.2.2 Transverse Stiffening . . . . .	5
1.3 Research Objectives . . . . .	6
1.4 Outline of Dissertation . . . . .	8
<b>Chapter 2 Literature Review</b>	<b>9</b>
2.1 Introduction . . . . .	9
2.2 Cellular Structures . . . . .	9
2.3 Morphing Aircraft Skin . . . . .	13
2.4 Meso-Scaled Structures . . . . .	17
2.5 Contact Mechanisms . . . . .	21
2.6 Topology Optimization . . . . .	23
2.7 Summary . . . . .	25
<b>Chapter 3 Analysis of Cellular Contact-Aided Compliant Mechanisms</b>	<b>27</b>
3.1 Introduction . . . . .	27
3.2 Proposed Structure . . . . .	27
3.2.1 Geometry . . . . .	27

3.2.2	Finite Element Analysis . . . . .	28
3.2.3	Prototype . . . . .	31
3.3	Analytical Model . . . . .	32
3.3.1	Large Deflection Approximation . . . . .	32
3.3.2	Global Strain . . . . .	36
3.3.3	Contact Gap . . . . .	38
3.3.4	Maximum Global Strain . . . . .	39
3.4	Results for Maximum Global Strain . . . . .	40
3.4.1	Delrin . . . . .	41
3.4.2	Zirconia . . . . .	42
3.4.3	Validation . . . . .	44
3.5	Experiments . . . . .	46
3.5.1	Experimental Setup . . . . .	48
3.5.2	Results . . . . .	48
3.6	Extension of the Analytical Model . . . . .	51
3.7	Size Optimization . . . . .	54
3.7.1	Problem Formulation . . . . .	54
3.7.2	Results . . . . .	55
3.8	Summary . . . . .	59
<b>Chapter 4 Morphing Aircraft Skin</b>		<b>61</b>
4.1	Introduction . . . . .	61
4.2	Description . . . . .	61
4.2.1	Development of Constraints . . . . .	63
4.2.2	Optimization Problem . . . . .	66
4.2.3	Solution Algorithm . . . . .	67
4.3	Results . . . . .	69
4.4	Stiffness Comparison . . . . .	74
4.4.1	In-plane Stiffness . . . . .	74
4.4.2	Transverse Stiffness . . . . .	76
4.4.3	Silicone Sheet . . . . .	77
4.5	Prediction of Morphing Strain using Analytical Model . . . . .	78
4.5.1	Optimization . . . . .	80
4.6	Summary . . . . .	82
<b>Chapter 5 Meso-Scaled Cellular Structures</b>		<b>83</b>
5.1	Introduction . . . . .	83
5.2	Design for Meso-Scale Manufacturing . . . . .	83
5.3	Experiments . . . . .	88
5.3.1	Estimation of Elastic Modulus of 316L Stainless Steel . . . . .	89

5.3.2	Experimental Setup . . . . .	90
5.3.3	Force-Displacement Testing . . . . .	92
5.4	Summary . . . . .	100
<b>Chapter 6 Synthesis of Cellular Contact-Aided Compliant Mechanisms</b>		<b>101</b>
6.1	Introduction . . . . .	101
6.2	Topology Optimization of Non-Contact Structures . . . . .	103
6.2.1	Solid Isotropic Material with Penalization (SIMP) . . . . .	104
6.2.2	Homogenization . . . . .	105
6.2.3	Maximum Local Strain . . . . .	108
6.2.4	Optimization Problem . . . . .	109
6.2.5	Optimizer . . . . .	111
6.2.6	Filtering Technique . . . . .	112
6.3	Topology Optimization of Contact-Aided Mechanisms . . . . .	113
6.3.1	Frame Structure . . . . .	114
6.3.2	Optimization Problem . . . . .	115
6.3.3	Investigation of Stress Relieving Designs . . . . .	116
6.3.4	Differential Evolution . . . . .	118
6.4	Results . . . . .	119
6.4.1	Honeycomb-Similar Cell . . . . .	120
6.4.2	Auxetic Cell . . . . .	123
6.4.3	Diamond Cell . . . . .	125
6.4.4	Doubly Auxetic Cell . . . . .	128
6.5	Summary . . . . .	130
<b>Chapter 7 Conclusions</b>		<b>132</b>
7.1	Summary . . . . .	132
7.2	Contributions . . . . .	136
7.3	Recommendations for Future Work . . . . .	137
<b>Appendix A Sensitivity Analysis for Inverse Homogenization</b>		<b>140</b>
<b>Appendix B Non-Overlapping Constraint</b>		<b>142</b>
<b>Bibliography</b>		<b>144</b>

# List of Figures

1.1	Plot of elastic modulus against the maximum elastic modulus for different materials. Materials are grouped together by their deformation mechanism [2] . . . . .	2
1.2	An example of contact-aided cellular mechanism showing a contact mechanism inside a cellular cell [5]. The cellular cell without the contact mechanism is non-contact cellular structure . . . . .	3
1.3	Illustration of stress-relief . . . . .	5
1.4	Variation of maximum bending stress against the contact load . . .	6
1.5	Variation of transverse stiffness against the tensile contact load . . .	7
2.1	Honeycombs made of different materials . . . . .	10
2.2	Undeformed and deformed shapes of a re-entrant honeycomb [16] .	11
2.3	Examples of auxetic materials (adapted from [16]) . . . . .	12
2.4	Zero Poisson's ratio cellular structures. The structure on left is called "hybrid", while that on right side is called "accordion" [22] .	12
2.5	Spider-plot showing the performance of an aircraft (Firebee) for two types of wing morphing. The radial distance represents the flight efficiency for the type of mission considered [25] . . . . .	13
2.6	(a) Nextgen Aeronautics bat-wing [35] (b) Lockheed Martin folding Z-wing [36] . . . . .	15
2.7	Morphing wings with integrated aluminum alloy skins . . . . .	16
2.8	Composite passive morphing skins: (a) Corrugated [44] and (b) Flexible matrix [27] . . . . .	17
2.9	Lithography layer sequence used to make the molds [60] . . . . .	18
2.10	A cross-sectional view of machine augmented composite [63] . . . .	19
2.11	Schematic representation microstructure of microporous polymeric materials: (a) undeformed and (b) deformed [65] . . . . .	20
2.12	MEMS cantilever beam composed of cellular structures [21] . . . . .	20
2.13	A contact-aided revolute joint. The flexures rotate with the cam surfaces and contacts the desired surface reducing the stress concentration in the flexures [68] . . . . .	21



2.14	Examples of compliant joint enhanced by contact formation [8] . . .	22
2.15	Contact-aided compliant mechanism to generate nonlinear, non-smooth path [67, 69] . . . . .	22
2.16	Cellular topologies obtained using inverse homogenization approach and frame elements (left) [76] and planar elements (right) [78] . . .	24
3.1	Geometry and nomenclature of a contact-aided compliant unit cell .	28
3.2	Cellular structure and boundary conditions applied for FE simulation	30
3.3	Stress history for non-contact and contact-aided cellular structure .	31
3.4	Delrin prototype of the contact-aided compliant structure: Left photo shows initial configuration and right photo shows deformed configuration and contact . . . . .	32
3.5	Free body diagrams of the cell walls . . . . .	33
3.6	Variation of global strain per unit material strain with cell angle for Delrin (solid line - contact-aided structure, dashed like - non-contact structure) . . . . .	42
3.7	Variation of global strain per unit material strain with cell angle for Zirconia (solid line - contact-aided structure, dashed like - non-contact structure) . . . . .	43
3.8	Comparison of deformed shapes from analytical model with finite element analysis . . . . .	45
3.9	Experimental setup and the aluminum models, without (left) and with (right) the contact mechanism . . . . .	49
3.10	Variation of residual strain with global strain. The kink in the contact-aided plot occurs when contact takes place . . . . .	50
3.11	Variation of non-dimensional reaction load vs. non-dimensional extension . . . . .	51
3.12	Stress history plots for various test cases using both analytical model and FEA . . . . .	53
3.13	Normalized measure of convergence as a function of the number of generations . . . . .	56
3.14	Pareto curves for various values of $\sigma_{all}/E$ for optimization problem given in Eqn. 3.33. The square boxes indicates the end points for each Pareto curve . . . . .	57
3.15	Pareto curves for various values of $\sigma_{all}/E$ for optimization problem given in Eqn. 3.34. The square boxes indicates the end points for each Pareto curve . . . . .	58
4.1	A variable span morphing wing with notation . . . . .	62

4.2	Example of nomenclature used for skin element and other integer variables . . . . .	64
4.3	Demonstration of constraint $r \sim 0.3$ . . . . .	65
4.4	Stress-strain characteristics for Delrin 100st . . . . .	69
4.5	Bar chart showing the total mass for non-contact cells as well as for contact-aided cells . . . . .	72
4.6	Reduction of required out-of-plane thickness while using contact . .	73
4.7	Maximum stress and structural mass with cell density . . . . .	73
4.8	Schematic representation of the optimized cell shapes for morphing skin . . . . .	75
4.9	Equivalent in-plane stiffness of skin . . . . .	75
4.10	Variation of the maximum perturbation against the morphing strain	77
4.11	Comparison of maximum global strain for non-contact and contact-aided cellular skin for various data points . . . . .	79
4.12	Plot showing the trade-off between the structural mass and the maximum global strain . . . . .	81
5.1	Contour plot of the effective strain and the non-dimensional initial contact gap for different unit cell geometries . . . . .	85
5.2	The overall length of a single cell for different aspect ratios and minimum possible initial contact gaps . . . . .	88
5.3	The overall width of a single cell for different aspect ratios and minimum possible initial contact gaps . . . . .	89
5.4	Photos of fabricated components (a) using composite 316L stainless steel with 3YSZ (b) using 316L stainless steel only . . . . .	91
5.5	A 316L stainless steel bar that is used for the determination of the elastic modulus . . . . .	92
5.6	Experimental setup to estimate the elastic modulus of 316L stainless steel . . . . .	93
5.7	A plot of stress-strain characteristics for test bars using Instron testing machine . . . . .	94
5.8	Photo showing the experimental setup for testing meso-scale cellular contact-aided compliant mechanisms . . . . .	94
5.9	A typical characteristic of the fixture when connectors are coupled together by a rigid plate . . . . .	95
5.10	Force-displacement characteristics of a meso-scale 316L stainless steel non-contact cellular mechanism and comparison to FEA prediction . . . . .	98

5.11	Force displacement characteristics of a meso-scale 316L stainless steel contact-aided cellular mechanism and comparison to FEA prediction . . . . .	99
5.12	Force-displacement characteristics of a meso-scale 316L stainless steel contact-aided mechanism for both loading and unloading . . .	99
6.1	A flow chart showing the two-stage topology optimization methodology for designing cellular contact-aided compliant mechanisms . .	103
6.2	Finite element meshing for SIMP model . . . . .	105
6.3	Load cases required to determine the homogenized elastic coefficients	106
6.4	Boundary conditions and loads for local strain calculation . . . . .	110
6.5	Periodic perturbations for random initial guess . . . . .	112
6.6	Conversion of continuum model into a frame structure . . . . .	115
6.7	Schematic showing the effect of sensitivity of initial contact gap to the maximum stress in a contact-aided mechanism . . . . .	117
6.8	Unit cell topologies similar to honeycombs . . . . .	120
6.9	Cellular structure formed by different unit cells . . . . .	121
6.10	Honeycomb similar unit cell without the local strain constraint . . .	121
6.11	Frame structure for honeycomb similar cell . . . . .	122
6.12	Stress relieving contact mechanisms for honeycomb similar cell with arbitrary contact gaps . . . . .	122
6.13	Cellular structure formed using the contact-aided cellular mechanisms for honeycomb-similar unit cells . . . . .	123
6.14	Unit cell topologies for negative effective Poisson's ratio . . . . .	124
6.15	Cellular structure formed by auxetic unit cells . . . . .	124
6.16	Frame structure for an auxetic cell . . . . .	125
6.17	Stress relieving contact mechanisms for auxetic cell with arbitrary contact gaps . . . . .	125
6.18	Cellular structure formed using the contact-aided cellular mechanisms for auxetic unit cells . . . . .	126
6.19	Stress relieving contact mechanisms with five contact pairs for auxetic cell . . . . .	127
6.20	A diamond shaped unit cell along with the unit cell and the effective properties . . . . .	127
6.21	Frame structure, contact-aided unit cell, and contact-aided cellular configuration for the diamond-shaped unit cell . . . . .	128
6.22	Another cellular structure with negative Poisson's ratio . . . . .	129
6.23	Frame structure for another unit cell with negative Poisson's ratio .	130
6.24	Stress relieving contact-aided unit cells . . . . .	130
6.25	Stress relieving symmetric contact-aided unit cells . . . . .	131

7.1	A contact-aided unit cell (left) for thermal shock resistance and schematic representation of a nozzle using such unit cells . . . . .	138
-----	---	-----

# List of Tables

2.1	Effects of wing geometric parameters on aircraft performance [24]	14
3.1	Error in displacements predicted using two approximations	35
3.2	Validation of maximum strains for Delrin	46
3.3	Validation of maximum strains for Zirconia	47
3.4	Summary of results for various materials	47
3.5	Geometrical parameters for different experimental specimens	48
3.6	Geometry and different objective functions for the end points of each Pareto curve	59
4.1	Design of morphing skin for non-contact cellular structure using non-linear elastic material model	70
4.2	Design of morphing skin for contact-aided cellular structure based on nonlinear elastic material model	71
4.3	Design of morphing skin for non-contact cellular structure using linearly elastic material model. Shaded rows indicate infeasible designs	74
4.4	Design of morphing skin for contact-aided cellular structure using linearly elastic material model (NC - contact mechanism is present but not used, C - contact mechanism is used). Shaded rows indicate infeasible designs	76
4.5	Comparison of maximum global strain and initial contact gaps using analytical model and FEA	79
5.1	Final combined design constraints for the fabrication of cellular contact-aided compliant mechanisms using 316L stainless steel and 3YSZ	85
5.2	Two candidate geometries for meso-scale cellular contact-aided compliant mechanisms	90
6.1	Comparison of two stages used in the synthesis of contact-aided cellular mechanisms	102

# Acknowledgments

I would like to acknowledge Air Force Office of Scientific Research (Structural Mechanics Division), National Science Foundation, and Department of Mechanical and Nuclear Engineering for their monetary support. I would like to thank my both advisors Dr. Frecker and Dr. Lesieutre for guidance, support, generosity, and patience. I would also like to thank Dr. Adair, Dr. Rahn, and Dr. Simpson for serving on my committee.

There are many people who directly or indirectly helped me during this study. I would especially like to thank Greg Hayes for fabricating meso-scaled cellular structures, Samantha Cirone for making prototypes of new topologies, Pramod Vemulapalli for assisting to develop non-overlapping algorithm. Many thanks to High Performance Computing staff, Phil Irwin (Reber Machine Shop), Instrument Room staff, Amanda Baker (MRI Laser), David Shelleman (Instron Machine), and Learning Factory staff for helping me throughout the course of research.

I would also like to thank my fellow EDOG lab members, friends in the Vehicles group, and my tennis partners for their support and friendship during my time at Penn State. Lastly, many thanks to my parents for their moral support.

# Introduction

## 1.1 Background

Many engineering applications need materials having specific properties. Some of these applications demand conflicting properties such as high strain – high strength, high strength – low density, high thermal conductivity – high thermal diffusivity [1]. Nature, on the contrary, offers materials of only a limited range of properties. Such materials may not be the most suitable in many cases. Therefore, new materials such as alloys, composites, foams, and/or sandwich structures are tailored to meet specific needs.

High strength materials are often sought for structural and load carrying applications. The elastic modulus is generally a good representative for comparing the flexural strength of the material [1]. Structures made using alloys and ceramics have excellent flexural stiffness. On the other hand, many adaptive structures need materials with high recoverable elastic strain. The maximum overall strain that a material or structure can manage without permanent deformation is the elastically recoverable strain. Alloys and ceramics demonstrate a relatively small elastic strain, while elastomers and foams have relatively high elastic strain.

More recent adaptive structures are required to bear loads encountered due to the surrounding. They may also need to change their shape or size as a part of their tasks. The material for such structures must have high strength as well as high strain capability. A plot of elastic modulus and maximum elastic strain for

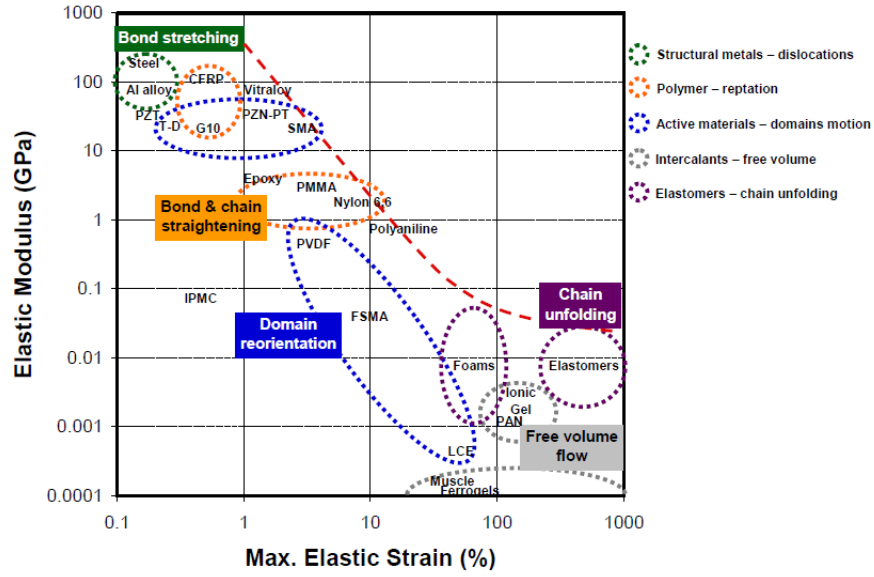


**Figure 1.1.** Plot of elastic modulus against the maximum elastic modulus for different materials. Materials are grouped together by their deformation mechanism [2]

different materials is shown in Figure 1.1. It demonstrates that existing materials can either have a high strength or a high maximum elastic strain but not both.

Notably, there are two principal types of materials potentially useful in such adaptive structures: active and passive. An active material needs external energy to effect a change in its mechanical properties. These changes in properties can be utilized to stiffen or to soften the material and effect a shape change as per the requirement, e.g., shape memory alloys and polymers. A comprehensive review of such active materials can be found in [3]. The energy source required for the active materials may not be readily available. Passive materials in the form of compliant mechanisms, however, provide an excellent alternative. The passive materials have material macrostructure or microstructure made of compliant links and joints, e.g., cellular materials and foams. During the deformation, the individual compliant members bend, which allows a higher effective maximum elastic strain than that of bulk material. Many such materials also possess a good strength-to-weight ratio [4].

Two type of passive compliant mechanisms, which have been implemented for high strength as well as for high strain applications, are cellular structures and



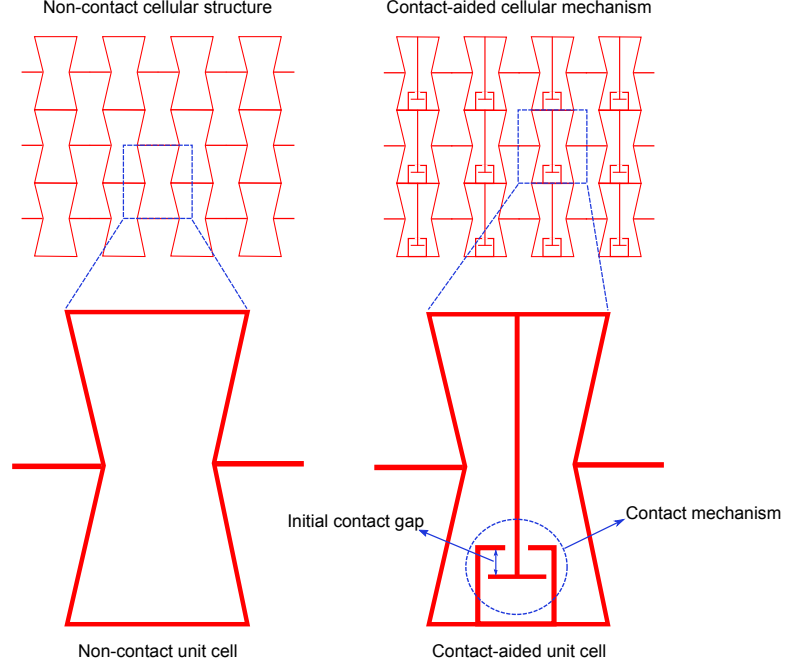


**Figure 1.2.** An example of contact-aided cellular mechanism showing a contact mechanism inside a cellular cell [5]. The cellular cell without the contact mechanism is non-contact cellular structure

contact-aided compliant mechanisms. A subset of cellular structures are compliant mechanisms, where a compliant mechanism is repeated in space in a patterned or random manner [4]. Cellular structures have been used in load carrying applications and they were recently employed for high elastic strain [6,7]. An example of a cellular structure is shown in Figure 1.2(left). Contact-aided compliant mechanisms are compliant mechanisms, which experience self contact under deformation. Since such contact decreases the stress concentration in a compliant mechanisms, it was used to improve the load bearing capacity of the compliant mechanisms [8]. A hybrid design comprising of both cellular design and contact-aided compliant mechanism is shown in Figure 1.2(right).

## 1.2 Motivation

There are other unexplored benefits of using contact in compliant structures. In this work, two benefits, specifically, stress relief and transverse stiffening, are investigated. Under deformation, a solid body experiences stress that can lead to

structural failure. If the structure contacts another object during this deformation, extra loads can arise. These loads can be used to counteract the failure-causing loads. This phenomena is called “stress relief”. In another case, such loads can be utilized for stiffening the structure in a direction perpendicular to the loads. This is termed “transverse stiffening”. These concepts are illustrated in the following example.

### 1.2.1 Stress Relief

For example, consider a beam as shown in Figure 1.3. The beam is clamped at one end. The other end of the beam is restrained to have no rotation. A design goal is to maximize the lateral deflection of the guided end ( $\Delta$ ). Without any aid from contact, this deflection is caused by the lateral loads ( $W$ ) and the maximum deflection and moment are given by [9]

$$\Delta = \frac{Wl^3}{12EI} \quad (1.1)$$

$$M_{\max} = Wl/2 \quad (1.2)$$

$$\Rightarrow M_{\max} = \frac{6EI\Delta}{l^2} \quad (1.3)$$

where  $E$ ,  $I$  are the Young’s modulus and area moment of inertia of the beam respectively. Assuming Euler-Bernoulli beam theory, the maximum tensile bending stress is given by

$$\sigma_{\max} = \frac{M_{\max}t/2}{I} = 3E\frac{\Delta}{l} \quad (1.4)$$

where  $t$  is the thickness of the beam. If a block, representing a contact surface, contacts the top of the beam before the deformation as shown in the figure, an axial load,  $P$ , is generated (e.g. a weight on the beam). The maximum deflection and moment caused by this combined loading is given by

$$\Delta = \frac{W}{kP} \left( 2 \tan \frac{kl}{2} - kl \right) \quad (1.5)$$

$$M_{\max} = \frac{W}{k} \tan \frac{kl}{2} \quad (1.6)$$

$$\Rightarrow M_{\max} = \frac{P\Delta}{2 \tan \frac{kl}{2} - kl} \tan \frac{kl}{2} \quad (1.7)$$

where  $k = \sqrt{P/EI}$ . The maximum tensile bending stress is then,

$$\sigma_{\max} = \frac{M_{\max}t/2}{I} = \left(\frac{kl}{2}\right)^2 \left[ \frac{\tan \frac{kl}{2}}{\tan \frac{kl}{2} - \frac{kl}{2}} \right] E \frac{\Delta}{l} \frac{t}{l} \quad (1.8)$$

A normalized variation of  $\frac{\sigma}{E \frac{\Delta}{l} \frac{t}{l}}$  against non-dimensional contact-axial load ( $kl$ ) is shown in Figure 1.4. Clearly, the bending stress for a particular value of  $\Delta$  significantly decreases as the contact load increases, demonstrating the stress relief. The axial load here effectively decreases the lateral stiffness.

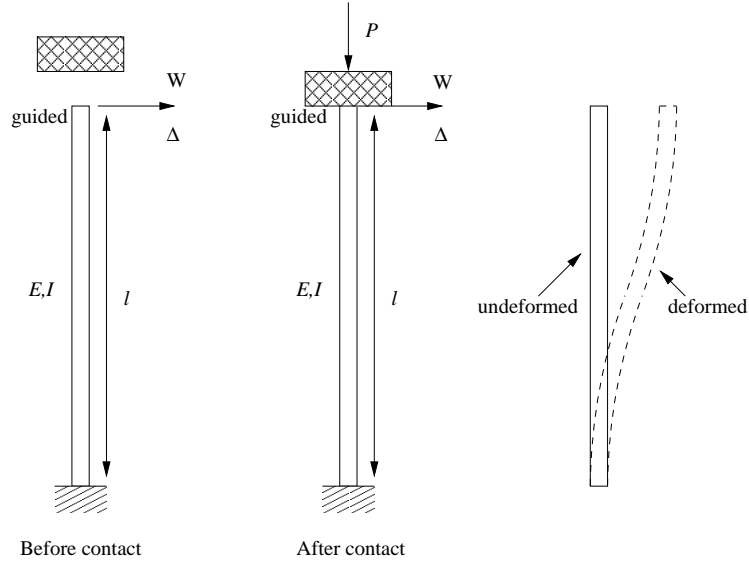


**Figure 1.3.** Illustration of stress-relief

### 1.2.2 Transverse Stiffening

Without the contact, the stiffness of the structure for lateral load can be given as

$$k_{stiff} = \frac{W}{\Delta} = 12 \frac{EI}{l^3} \quad (1.9)$$

The previous example has the compressive axial force induced due to contact. Now instead of compressive load, consider the case where a tensile load is generated as a result of contact. The maximum deflection produced, in this case, will be

$$\Delta = \frac{W}{kP} \frac{2 + kl + e^{kl}(kl - 2)}{1 + e^{kl}} \quad (1.10)$$

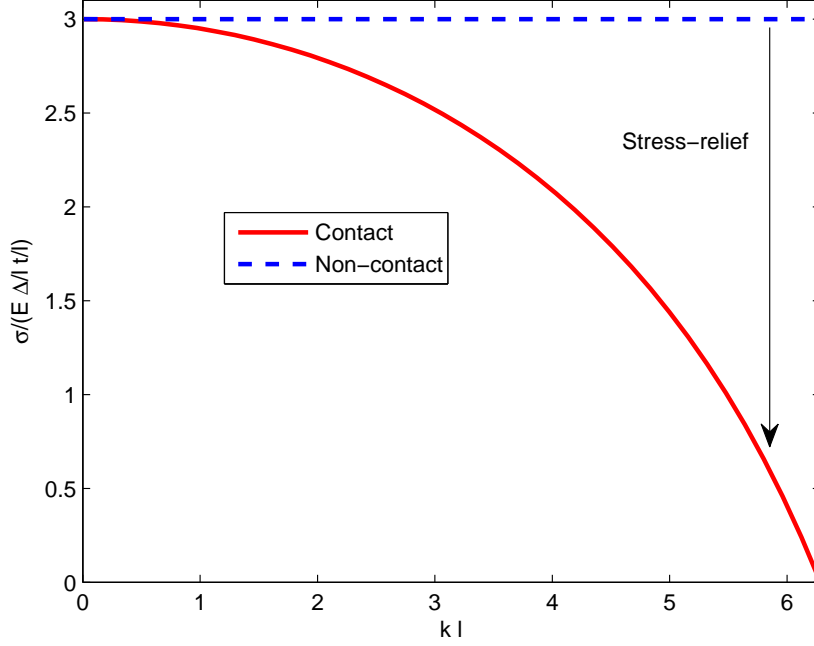


**Figure 1.4.** Variation of maximum bending stress against the contact load

where,  $k = \sqrt{-P/EI}$ . The stiffness of the structure is then,

$$k_{stiff} = \frac{(kl)^3 (1 + e^{kl})}{2 + kl + e^{kl}(kl - 2)} \frac{EI}{l^3} \quad (1.11)$$

The normalized variation of the stiffness ( $k_{stiff}/(EI/l^3)$ ) against non-dimensional contact-axial load ( $kl$ ) is shown in Figure 1.5. The transverse stiffness increases as the contact induced tensile axial load increases, showing the transverse stiffening.

### 1.3 Research Objectives

Although cellular structures are better in many aspects than solid metallic, polymer or composite structures, the question still remains as to whether one can improve the properties further. Additionally, if contact is used in these structures, can it be advantageous in adaptive structures such as morphing skin? This question has motivated the current work. The focus of this work is on design and

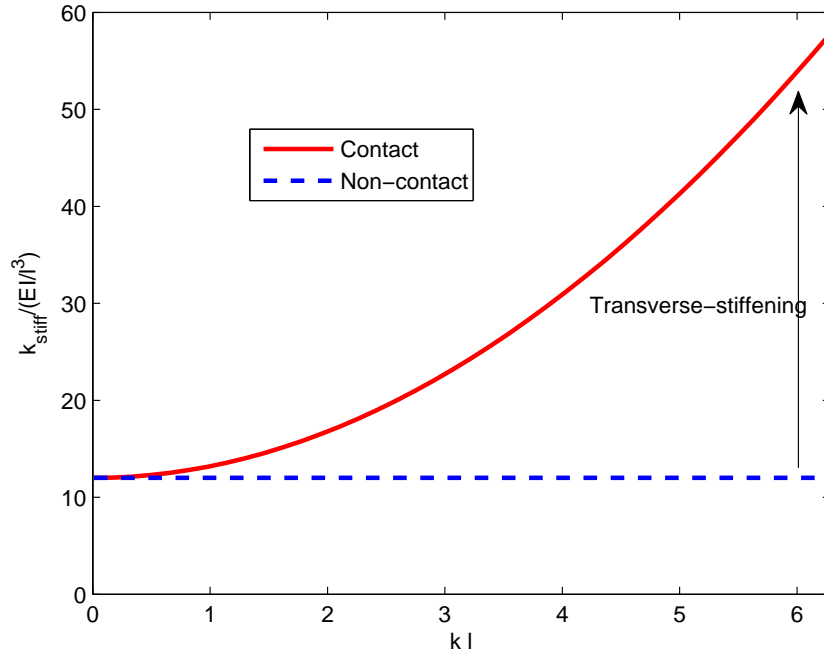


**Figure 1.5.** Variation of transverse stiffness against the tensile contact load

analysis of cellular contact-aided compliant mechanisms, which have not yet been considered in the literature.

This dissertation presents a new type of cellular structures, called “contact-aided compliant cellular” structures, which have improved properties compared to solid structures or cellular structures without contact. Specifically, the main objectives of this research are:

1. To develop techniques to design cellular contact-aided mechanisms with magnified the maximum allowable overall elastic strain.
2. To develop techniques to improve the transverse stiffness of cellular structures without penalizing structural mass.
3. To develop topology optimization methods to synthesize the contact-aided compliant mechanism for a given application.
4. To investigate the applications of the contact-aided cellular mechanisms in morphing aircraft skin and meso-scaled structures.

5. To fabricate and test these contact-aided cellular structures to validate their feasibility and to verify the numerical and analytical models.

## 1.4 Outline of Dissertation

The rest of the dissertation deals with how the research objectives are pursued. Chapter 2 presents related literature on cellular structures and contact mechanisms. It also discusses some applications of high-strength, high-strain materials in morphing aircraft skin and meso-scaled components. Some of the topology optimization procedures used for the synthesis of cellular structures and contact-mechanisms are described.

Chapter 3 addresses one specific cellular contact-aided compliant mechanism. The chapter develops an analytical formulation for the proposed structure. It presents results for various materials, and describes the experimental validation of stress relief.

Chapters 4 and 5 describes applications of the proposed mechanism to morphing skin and meso-scaled components. The proposed cellular concept is applied to a small UAV and results are compared to those for a cellular structure without contact. A cellular mechanism for meso-scaled manufacturing is designed and its testing is also discussed.

Chapter 6 outlines a design methodology for synthesizing the proposed mechanisms. It presents a two-step approach. Results obtained for both cellular structures without contact and for contact-aided mechanisms are given.

Chapter 7 summarizes the major results of the dissertation and discusses possible work for the future.

# Literature Review

## 2.1 Introduction

In this chapter, literature on various aspects of the research is presented. It includes literature on cellular structures, contact mechanisms, morphing skin, and meso-scaled cellular materials. The chapter also discusses some of the topology optimization tools, which can be used to synthesize cellular structures and contact mechanisms.

## 2.2 Cellular Structures

Cellular structures, by definition, are “*made up of an interconnected network of solid struts or plates which form the edges and faces of cells*” [4]. A subset of cellular structures are compliant mechanisms. Some naturally occurring examples of cellular structure are honeycomb, cork, animal skin, etc. There are two types of cellular structures. On one hand, there is a two dimensional unique cell, which is repeated periodically to fill up the space, e.g., honeycombs. On the other hand, there are randomly distributed compliant members in three dimensional space, which are commonly called foams, e.g., sponge.

There has been a lot of attention into man-made cellular structures because of their unique characteristics. The most popular cellular structure is regular honeycombs. Such honeycomb structures are extensively used in aerospace industries,

insulation, packaging, and other structural industries [4, 10, 11]. Cellular structures, especially honeycombs, have a high strength-to-weight ratio. This property is well exploited in the applications mentioned earlier. Honeycombs are made using different materials. Metallic and polymer (Kevlar or Nomex [12]) honeycombs are commercially available. Less common are cellular structures made of shape memory alloys [13] or shape memory polymers [2]. Examples of honeycombs fabricated with a variety of materials is shown in Figure 2.1.

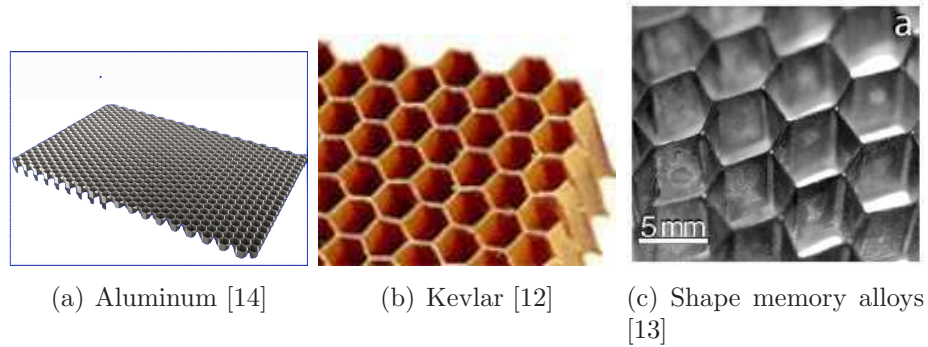


**Figure 2.1.** Honeycombs made of different materials

Cellular structures are often found with two relatively low strength face-sheets. This configuration is called a sandwich structure [15]. Cellular structures can be of different cell geometries. Although hexagonal shaped cells (honeycombs) are very common, rectangular, circular shaped cells can also be made [4]. Recently, researchers have discovered additional benefits of cellular structures that make them more attractive than solid structures such as Poisson's ratio [16], vibration absorbtion [17], high strain capability [2, 7, 18].

Cellular structures with a negative Poisson's ratio are called auxetic structures. R. Lakes first demonstrated negative Poisson's ratio materials using foams [19]. Another important cellular structure, which exhibits a negative Poisson's ratio, is shown in Figure 2.2. It is commonly called a re-entrant honeycomb. Scarpa et al. modeled such materials numerically and experimentally validated the model [18]. They found that these structures are highly sensitive to the geometric parameters.

Re-entrant structures are useful in a variety of applications. One such application include adaptive or deployable structures. Many researchers have used auxetic structures in high strain environments (e.g., [2, 7]). Henry and McKnight have used shape memory polymers for auxetic cellular structures to get about 70%



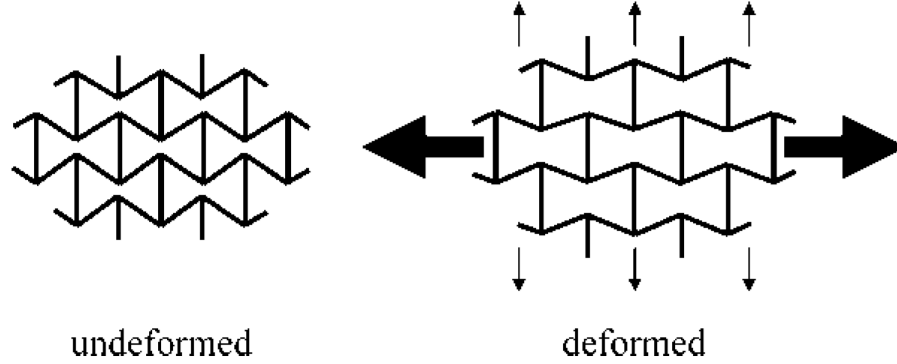


**Figure 2.2.** Undeformed and deformed shapes of a re-entrant honeycomb [16]

elastic strain [2]. They concluded that although very high elastic deformation can be achieved using such structures, the elastic properties tend to change with the deformation. Olympio and Gandhi investigated passive cellular structures made of aluminum and Delrin [7]. The maximum overall strain was found to be at least an order of magnitude greater than that of the core material. In another study, they examined a similar cellular composite with face sheets and infills for high strains as well as high strengths [20]. They observed that infill material increases the flexural strength of the cellular composite, but also increases the actuation requirements. Re-entrant materials can also be used as vibration absorbers for sandwich panels [17]. In one such study, the authors implemented a first-order sandwich plate theory to predict the out-of-plane properties of cellular structures. They concluded that bending stiffness for auxetic materials is better than the regular honeycomb materials.

There are many other cellular structures having a negative Poisson's ratio. A comprehensive review of auxetic materials can be found in [16]. Some examples of auxetic materials are shown in Figure 2.3. The strain relief and chiral cellular materials were used for high strain applications [2,6], while the double arrowhead cellular structure was used in MicroElectroMechanical Systems (MEMS) [21].

Notably, any cellular structure with a non-zero Poisson's ratio deforms in a direction that is perpendicular to the loading. Such deformations could be undesirable or they cannot be accommodated by the supporting structural members. To circumvent this problem, cellular structures with zero Poisson's ratio are de-

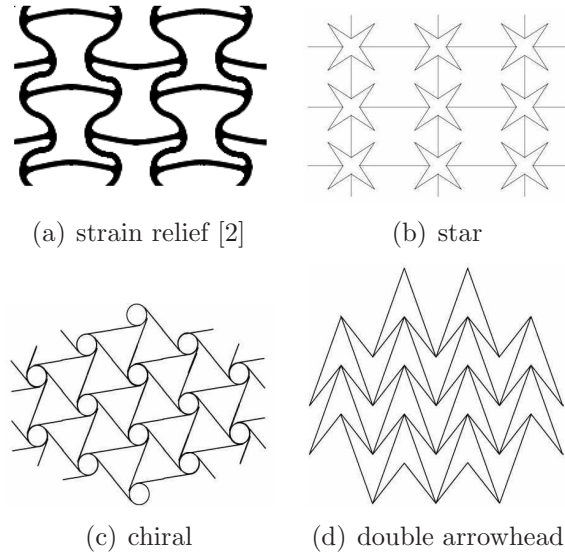


**Figure 2.3.** Examples of auxetic materials (adapted from [16])

veloped and shown in Figure 2.4 [22]. Although the effective strain capacity of these cellular structures is comparable to the traditional non-zero honeycombs, their flexural stiffness is poorer.

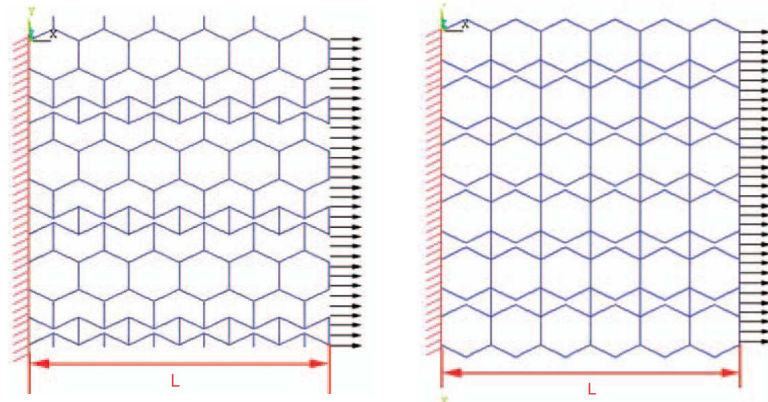


**Figure 2.4.** Zero Poisson's ratio cellular structures. The structure on left is called “hybrid”, while that on right side is called “accordion” [22]

The structural properties of cellular structures can be investigated by analyzing the smallest representative unit cell [4]. For example, the moduli of elasticity, Poisson's ratio, shear modulus have been derived for various cellular structures using a linear model [4, 7, 18, 23].

This review on cellular structures shows that such structures have high strength as well as capable of providing high elastic strains. The next two sections provide reviews on two potential applications for such structures. One application involves adaptive aircraft wings, while another focuses on the meso-scaled structures.

## 2.3 Morphing Aircraft Skin

The performance of an aircraft mainly depends on its engine and wing geometry. If all such parameters are fixed, the performance is optimal only for a particular flight maneuver. If the same aircraft is being used for different missions, its configuration are required to change. A morphing aircraft can change its configuration in-flight to achieve different types of mission tasks [24]. While lift and speed are important performance measures for aircraft flight, the others include drag, fuel efficient, and stability.

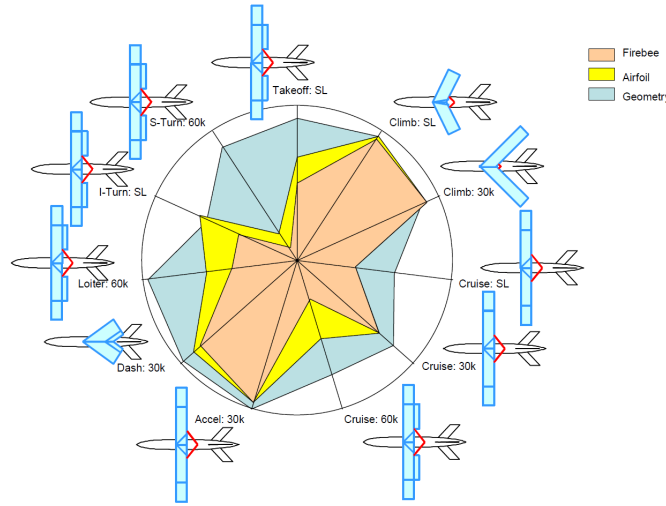


**Figure 2.5.** Spider-plot showing the performance of an aircraft (Firebee) for two types of wing morphing. The radial distance represents the flight efficiency for the type of mission considered [25]

A number of technologies are suggested for changing aircraft wing parameters. The effect of planform morphing and airfoil morphing on the flight performance was studied by Joshi et al. [25] and is shown in Figure 2.5. They compared a specific aircraft, Firebee, for different types of flight conditions. They considered two types of morphing: airfoil and planform. The radial distance represents the

flight efficiency. Planform morphing has been shown to improve the performance in most flight maneuvers. Jha and Kudva qualitatively studied the effect of different geometry parameters on the aircraft performance [24]. The results which are related to the planform geometry are summarized in Table 2.1. These studies indicate that planform morphing has the most significant impact on the aircraft performance.

**Table 2.1.** Effects of wing geometric parameters on aircraft performance [24]

Parameter		Effect of variability
Wing plan area	↑	Increases - lift, load factor capability
	↓	Decreases - parasitic drag
Wing aspect ratio	↑	Increases - L/D, loiter time, cruise distance turn rates
		Decreases - engine requirements
		Increases - maximum speed
	↓	Decreases - parasitic drag
Wing dihedral	↑	Increases - Rolling moment capability, lateral stability
	↓	Increases - maximum speed
Wing sweep	↑	Increases - critical Mach no., dihedral effect
		Decreases - high speed drag
	↓	Increases CLmax
Wing taper ratio	–	Wing efficiency (spanwise lift distribution); Induced drag
Wing Twist Distribution	–	Prevents tip stall behavior; Spanwise lift distribution

Since incorporating all types morphing in a single wing is a difficult problem, researchers have considered only a few variations. Morphing technologies available today are either one-dimensional, two-dimensional, or three-dimensional. One dimensional morphing generally includes changing the span of the wing. This can be achieved either by implementing a cellular structure [26], by using a flexible matrix composite [27], by incorporating a telescopic wing structure [28,29], or by utilizing compliant mechanisms [30]. One type of the two-dimensional morphing is to change the airfoil geometry. This can be done by using inflatable wings [31], by using chiral cellular structure [6], or by utilizing compliant mechanisms [32]. Nextgen Aeronautics has developed a 2-dimensional “bat-wing”, which is capable of changing the wing area by 70%, span by 40%, aspect ratio by 200%, and varying wing sweep between 30% to 75% [33]. There are relatively very few designs for three dimensional morphing. Ramrakhyani et al. have developed a morphing wing using rigid link mechanisms for variable airfoil camber and sweep [34]. Lockheed

Martin has developed a Z-shaped wing for out-of-plane morphing. Some of these concepts of morphing wings are illustrated in Figure 2.6.

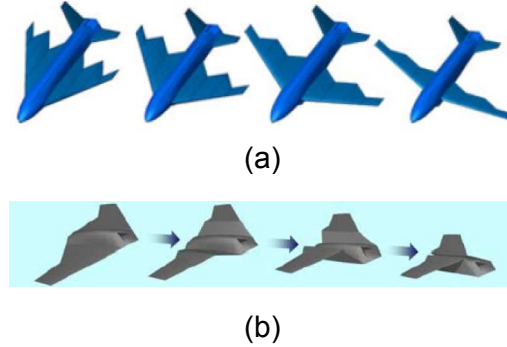


**Figure 2.6.** (a) Nextgen Aeronautics bat-wing [35] (b) Lockheed Martin folding Z-wing [36]

Relatively less attention has been given to morphing skin. The technologies described earlier can change the shape or size of the wing. However, they may not provide a desired and smooth aerodynamic shape. A smooth covering, called skin, is necessary to provide such a surface. Skin must be able to undergo a shape or a size change along with the attached morphing actuators without a local failure. Moreover, skin may be required to carry or transfer the aerodynamic loads to the underlying morphing mechanism or fuselage [24]. These conflicting requirements make the design of skin difficult and researchers are trying to implement innovative concepts to tackle the problem. An ideal morphing skin should be light weight, have high flexural stiffness, and have high strain capability.

A comprehensive review of morphing skin is given by Thill et al. [37]. Notably, some morphing wings are designed in such a way that skin is integrated with the morphing mechanism. Traditional skin made of aluminum alloys can be used for such designs. Telescopic mechanisms [28] (see Figure 2.7(a)) and compliant mechanisms [38] (see Figure 2.7(b)) are two examples of this concept. Although such skins have high flexural stiffness, their implementation is limited to only one type of morphing.

Morphing skins, which are required to envelope the underlying mechanisms, can be divided into two categories: active and passive. Shape memory alloys and shape memory polymers are extensively used for active skin materials. Shape

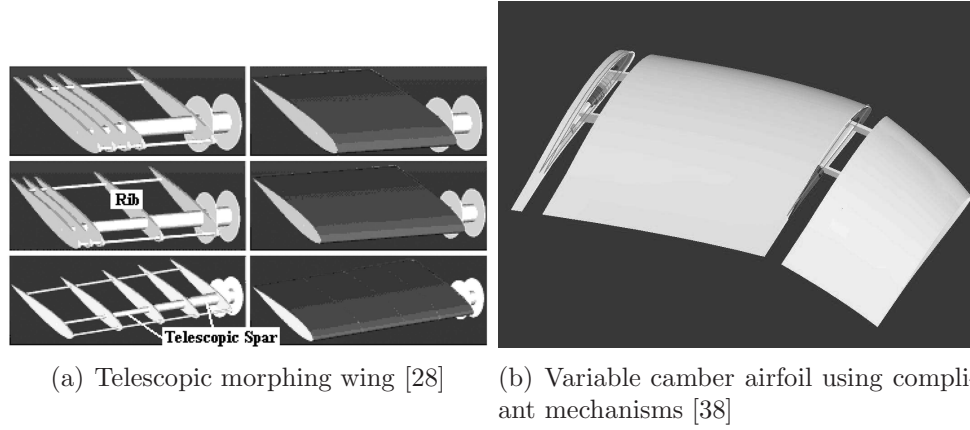


**Figure 2.7.** Morphing wings with integrated aluminum alloy skins

memory alloys and polymers have a high stiffness at low temperatures, but a low stiffness at higher temperatures. A structurally stiff skin at a low temperature can be used to carry or transfer the loads. The skin is then heated to change the shape or size of the wing. Reed et al. have suggested a solid or cellular sheet of shape memory polymer [39]. Another concept is based on variable stiffness materials using shape memory polymers [40]. Advantages of cellular structures are combined with shape memory materials to obtain new skin materials. Honeycomb [2, 39], auxetic [2], or newer shapes [41–43] have been suggested. Active skins, however, require additional energy for actuation, which can increase the structural mass as well as engine requirements.

Another concept that is investigated is the use of a passive skin which can deform with the underlying morphing mechanism. To obtain the necessary high out-of-plane stiffness while providing high overall strain for morphing, composites and cellular structures have been suggested [6, 7, 22, 27, 44]. Yokozeki et al. have designed composite skin using corrugated materials for span morphing [44], since corrugated materials can sustain high strain in corrugated direction and stiff in the transverse direction (see Figure 2.8(a)). Another design for composite skin using directional flexible matrix for span morphing is suggested by Murray et al. (see Figure 2.8(b)) [27]. The matrix dominated direction is aligned with the morphing direction, while the fiber direction have higher stiffness to withstand aerodynamic loads.

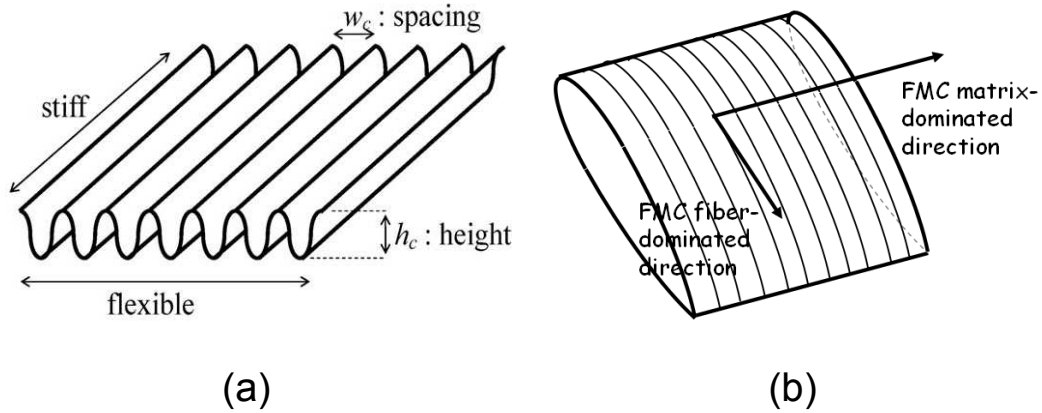


**Figure 2.8.** Composite passive morphing skins: (a) Corrugated [44] and (b) Flexible matrix [27]

Since cellular structures exhibit high strain and high strength, various cellular materials are also explored for morphing skin application. In one such concept, honeycombs-similar and zero Poisson's ratio cellular structures (see Figure 2.4) are proposed for one-dimensional morphing [7, 22]. The authors have studied the geometry of the cellular structure to maximize the overall strain capacity. However, they have not considered the effect of aerodynamic loads when the skin is attached to the morphing mechanism.

## 2.4 Meso-Scaled Structures

Another important application of high strength and high strain materials is in the meso-scaled structures. Meso-scale structures are about millimeters scale with micron scale features. This section reviews some such structures and their fabrication methodologies.

Micro-fabrication techniques have been successfully used in the silicon chip industry for a number of years. Mechanical micro-sized components are now also manufactured for use in applications such as micro-chemical reactors [45], micro-turbines [46], gas sensors [47], micro-actuators [48], and surgical instruments [49, 50]. Ceramics are particularly appealing in these applications because of their high-temperature capability, chemical stability, and relatively high mechanical strength. Such micro-ceramic devices are fabricated using various meth-

ods [51–54], including prototype forming directly from designs, self-assembly techniques using micro-contact printing [55] and micro-transfer molding [56]. Another method for manufacturing thick parts is the Lost-Mold Rapid Infiltration Forming (LMRIF) technique. In this method, photo-lithography is used to create molds from refractory materials such as  $\alpha$ -alumina [57]. SU8 is typically used as the photo resist. A colloidal solution of ceramic powder is then gel-cast into the molds, and subjected to high-temperature sintering. The micro-parts are separated from the substrate either by dissolving the substrate in a chemical solution [58] or by thermal decomposition of the substrate [59].

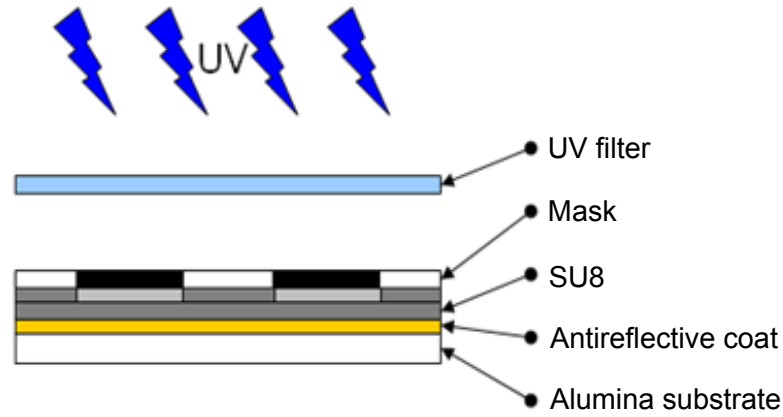


**Figure 2.9.** Lithography layer sequence used to make the molds [60]

Our collaborators in Penn State have improved LMRIF process to increase the process yield and to obtain parts with higher aspect ratios. The process developed includes mold fabrication, nanoparticulate suspension preparation, casting, and sintering. Mold fabrication research includes the development of a modified lithography process capable of thicknesses ranging from 10 to over 500 microns. Polished polycrystalline alumina substrates are used as substrates and SU8 photo-resist molds are fabricated on top of the substrate using a modified UV lithography process as shown in Figure 2.9. An antireflective coating is spin coated on to the substrate to eliminate mold defects caused by light scattering caused by the substrate. A calculated amount of pre- and post-baking is carried out for proper bonding between various layers. UV light exposure is employed to ensure vertical side walls in the final parts. Either 3% mol fraction yttria partially stabilized zirconia or particulate stainless steel 316L is dispersed and concentrated. For nanopar-



ticulate zirconia, chemically-aided attrition milling is used to reduce the particle sizes. Various chemicals added during the dispersion and concentrations create a colloidal suspension of the particles. Such suspension along with gel-casting monomers, cross-linkers, binders, and plasticizers are utilized to prepare the final colloidal solution. The gelation reaction converts the solution into a nanoparticulate zirconia or particulate stainless steel slurry. The slurry is infiltrated into the molds using screen printing squeegee technique. The slurry is allowed to dry in ambient atmosphere. The excess slurry is removed via planarization. The molds are removed using pyrolysis, which is followed by sintering. Detailed information about this process can be found in [49, 50, 60–62]. Through the process development, the ability to produce parts ranging in thickness from 10 to 400 microns has been demonstrated [60].

Not much attention has been given on fabricating cellular structures at small scales. Hawkins et al. explored the possibility of augmenting micron sized mechanisms in a composite structure [63]. A cross-sectional view of one such machine-augmented composite is shown in Figure 2.10. Each mechanism is about 1 mm in size, extends through the thickness, and separated a layer of fibers. Evidently, such composites can exhibit properties that are difficult to obtain otherwise. These composites are proposed to be used in fasteners, gaskets, or seals.

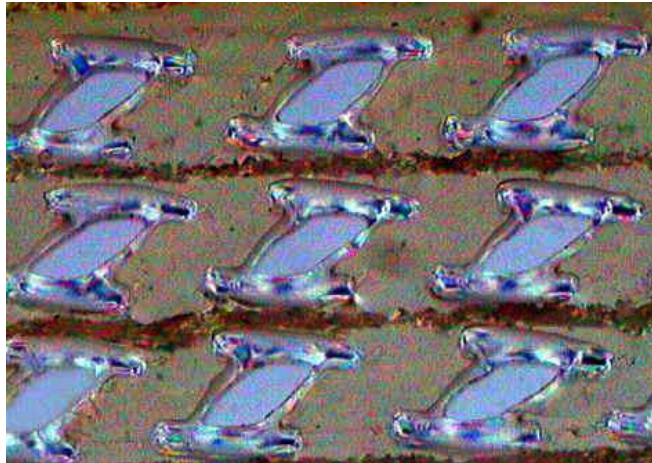


**Figure 2.10.** A cross-sectional view of machine augmented composite [63]

Evans studied microporous polymeric materials exhibiting negative Poisson's ratio [64]. Two such materials, polytetrafluoroethylene and ultra-high molecular

weight polyethylene, were analyzed for their mechanical properties [65]. Schematically the microstructures of these materials is shown in Figure 2.11.

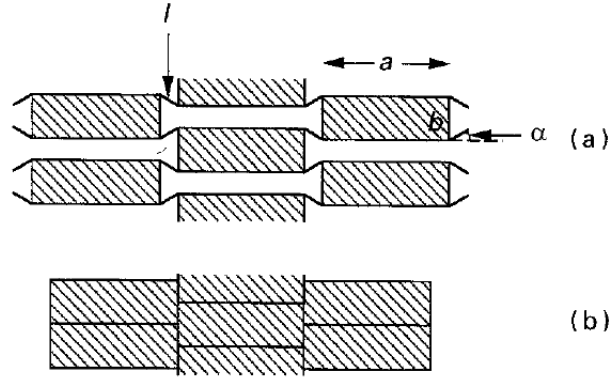


**Figure 2.11.** Schematic representation microstructure of microporous polymeric materials: (a) undeformed and (b) deformed [65]

Meso-scaled cellular structures with a negative Poisson's ratio are useful in micro-devices, motion transformers, and micro-capsules [21, 66]. Larsen et al. fabricated double arrowhead cellular structures using MEMS procedures [21]. A cantilever beam using such a structure is shown in Figure 2.12. Although their methodology is promising, the final structure was attached to the substrate, and a free-standing part was not obtained.

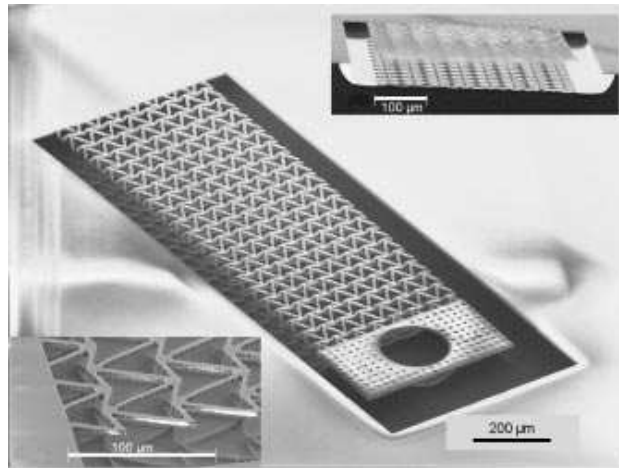


**Figure 2.12.** MEMS cantilever beam composed of cellular structures [21]

The sections so far focused on the cellular structures and their applications. There is another subset of compliant mechanisms that utilizes contact between two compliant members. Such mechanisms can also be used to redistribute the loads in the mechanism. A review of contact mechanisms and their applications are summarized in the next section.

## 2.5 Contact Mechanisms

When the distance between two or more surfaces vanishes, contact is said to have taken place. Contact-aided compliant mechanisms are defined as flexible structures that experience internal contact as the structure deforms. Because of contact, additional loads and/or constraints are introduced in the system. Despite the difficulty of the problem arising with the nonlinearity of contact, the added loads/constraints, can perhaps be used for different purposes. In one such scheme, contact interactions with different compliant members have been used to enhance the performance of the system by reducing the stress concentrations [67,68]. Cannon and Howell have used this concept to design a contact-aided revolute joint (see Figure 2.13), which has better performance than the comparable traditional joint.

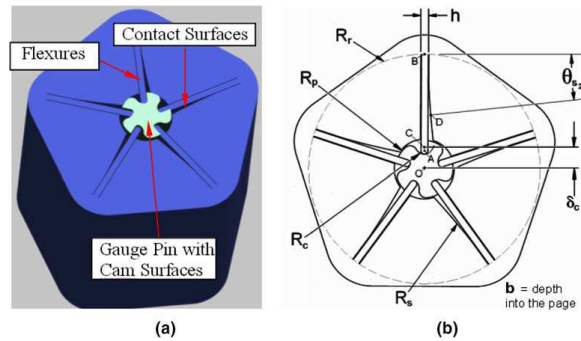


**Figure 2.13.** A contact-aided revolute joint. The flexures rotate with the cam surfaces and contacts the desired surface reducing the stress concentration in the flexures [68]

Contact can also be used to increase the load bearing capacity of the compliant mechanisms. Guerinot et al. designed a number of compliant joints to be used in high compressive load situations [8]. Contact provides additional load carrying members. Two examples of such joints are shown in Figure 2.14. In each case,

contact takes place after a certain deformation allowing even more load to be carried.

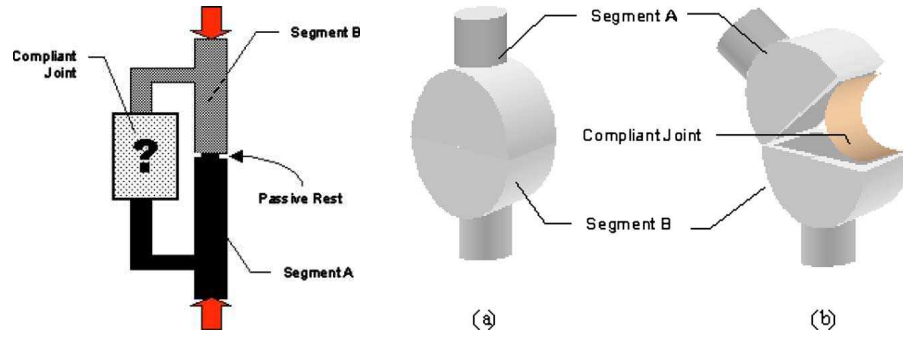


**Figure 2.14.** Examples of compliant joint enhanced by contact formation [8]

For a given output path, contact-aided compliant mechanisms can be designed [67,69]. The contact helps in generating a nonlinear, non-smooth shapes which might not be possible using traditional compliant mechanisms. One of the application of such mechanisms is in the processing biological cells. Since maneuvering biological cells need complex motion, it may not be obtained through a compliant mechanism with contact. Contact-aided compliant mechanisms, however, provide nonlinear and non-smooth path suitable for the cell-maneuvers. They have modeled the system and experimentally validated it. They have also described a methodology to synthesize such mechanisms. A few of these contact-aided compliant mechanisms are shown in Figure 2.15

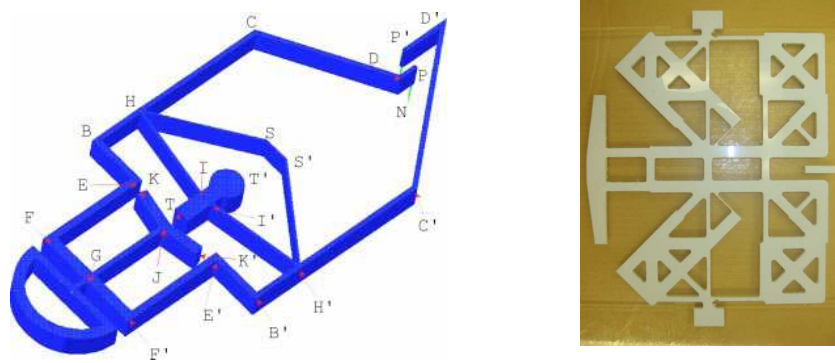


**Figure 2.15.** Contact-aided compliant mechanism to generate nonlinear, non-smooth path [67,69]

The studies on cellular structures, contact-aided compliant mechanisms, and their applications were based on a pre-determined topology. To design more of

such compliant mechanisms, one needs a systematic procedure. The following section reviews some schemes from topology optimization that can be employed to synthesize cellular structures as well as contact mechanisms.

## 2.6 Topology Optimization

Topology optimization is a tool that may be used to find the features such as the number, location and shape of holes in a solid structure and the distribution of material over a domain [70]. The optimal material distribution depends on specific objectives such as the compliance or strain energy of a structure for a given volume fraction. Finite element analysis is generally required in the evaluation of the objective function in topology optimization. Either frame elements or continuum (planar) elements are usually used as the finite elements. Both of these elements have been used in the literature.

An objective function based on minimizing compliance or strain energy makes the resulting mechanism stiff for the given loading and boundary conditions. Another objective function is to obtain a specific deflection at an output point for a given set of loading conditions. These objective functions have been extensively used for topology optimization to design compliant mechanisms (e.g., [70–73]).

Another objective function in topology optimization might involve finding an optimal material microstructure, a process known as inverse homogenization. Homogenization involves estimating effective elastic properties for a given material microstructure. A numerical implementation of homogenization theory is given in [74]. Estimation of homogenized coefficients using finite element methods was first presented in [75]. Such homogenization theory has been successfully used to design material micro-structures either for a prescribed elasticity matrix [76, 77] and to obtain a composite structure with extremal properties [78]. A cellular configuration can be obtained through the material microstructure.

Sigmund employed both frame elements and continuum elements to design periodic materials using inverse homogenization [76, 78]. Some of these designs are shown in Figure 2.16. Sigmund deduced that although the implementation using the continuum elements is more complex than the frame elements, the former allows

much more passive arrangement of the resulting topology. He has also extended the inverse homogenization approach for three-dimensional structures.

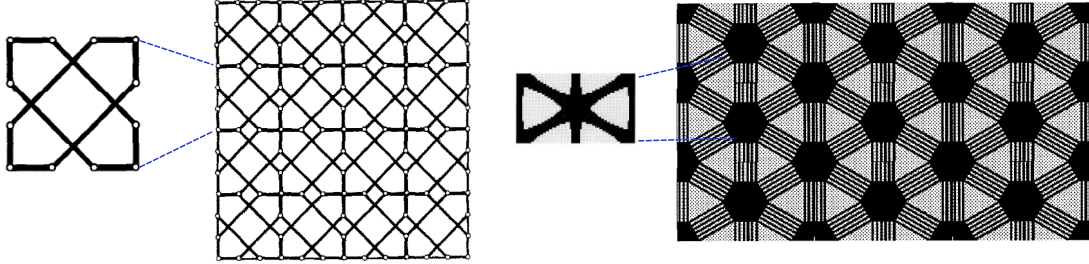


**Figure 2.16.** Cellular topologies obtained using inverse homogenization approach and frame elements (left) [76] and planar elements (right) [78]

Zhang and Sun [79] studied the effects of scale on the topology optimization of cellular structures. In their study, they changed the scale and aspect ratio of the desired unit cell and small variations were observed in the final topologies. A similar study was carried out by Qiu et al. [80] utilizing superelements.

The preceding schemes were targeted at stiffening the structure. Cellular structures that are useful for high strain applications were investigated by Olympio and Gandhi [81]. Instead of inverse homogenization, they employed multiple objective functions such as overall strain, volume, strain energy, and transverse displacements. A genetic algorithm based optimizer was used to solve the topology optimization problem. A number of possible solutions are obtained along the Pareto curve. However, only a few designs can result into a structurally stable cellular configuration.

Contact-aided compliant mechanisms, which experience contact during deformation, have also been synthesized using topology optimization [67, 69, 82]. In one such study, unilateral contact is considered for the compliance minimization of structures [82]. They have presented a mathematical formulation for the contact problem using frame elements. Contact nodes were predefined and contact was assumed to induce a constant pressure load. Such a condition is modeled using a nonlinear constraint, along with a linear finite element analysis. Linear programming tools are used to solve the problem. This study does not address any specific benefits that can be obtained through contact.



Contact-aided compliant mechanisms have an effective stiffness before contact occurs. Contact usually stiffens the mechanisms and increases their effective stiffness. Contact was therefore modeled as a nonlinear spring [67, 69]. The contact location was known a priori and the spring stiffness is a function of nodal displacement of these contact nodes. The contact stiffness increases inverse exponentially as the distance between the contact nodes is reduced. Although contact is a discontinuous phenomenon, a nonlinear spring model provides a continuous and regularized function to be used in analysis and synthesis. Geometrically nonlinear finite element analysis using frame elements is implemented for the topology optimization of compliant mechanisms. These mechanisms are designed to generate nonlinear, non-smooth output paths. Although this study presents a novel methodology to generate paths which might not have possible to obtain through traditional compliant mechanisms, contact location and the initial separation between the contact surfaces are predetermined.

## 2.7 Summary

A review of related literature on different aspects of the research is described. Cellular structures and contact mechanisms have a great potential to be used in the high-strain and high-strength applications such as morphing aircraft skin and meso-scaled structures. Furthermore, there are analytical tools available to synthesize these compliant mechanisms.

The review on cellular structures shows that they can be designed in various shapes, sizes, and materials to get specific effective properties. Two properties that are investigated here are the flexural stiffness and the overall strain. Contact-aided compliant mechanisms were utilized to increase the load carrying capacity. However, the literature does not reveal any studies which involve contact-aided compliant mechanisms implemented in the cellular structures. A direct application of cellular structures can be seen in morphing aircraft skin. Although some cellular structures are very good for this application, improving the properties further while minimizing the mass is still a concern. A methodology to implement a cellular skin for a morphing wing is missing as well. The concept of meso-scaled mechanisms provides new material macro structures. However, fabrication of com-

plex meso-scaled mechanisms and their testing for high strength and high strain is needed. Topology optimization schemes from the literature provide tools to synthesize cellular structures as well as contact-aided compliant mechanisms. A synthesis methodology for cellular contact-aided compliant mechanisms has not yet been considered. The rest of the dissertation focuses on the design, analysis and applications of the proposed cellular contact-aided compliant mechanism.



# Analysis of Cellular Contact-Aided Compliant Mechanisms

## 3.1 Introduction

This chapter addresses a candidate contact-aided cellular structure. It develops an analytical formulation for this proposed structure. It also presents a set of results for various materials and describes the experimental validation of the stress relief.

## 3.2 Proposed Structure

This section describes the geometry and concept of the contact-aided compliant mechanisms by presenting one representative structure.

### 3.2.1 Geometry

Cellular structures consist of an array of unit cells. The unit cell, the smallest representative structure [4] for the contact-aided compliant cellular structure, is presented in Figure 3.1. The geometry is similar to that of a honeycomb unit cell, with an additional contact mechanism inside the cell. As described earlier, such a cellular topology (without contact) has been shown to provide high strain and high bending stiffness [4, 7]. The geometric parameters and the nomenclature are as shown in the figure. The length of the horizontal members is  $h$  and that of the

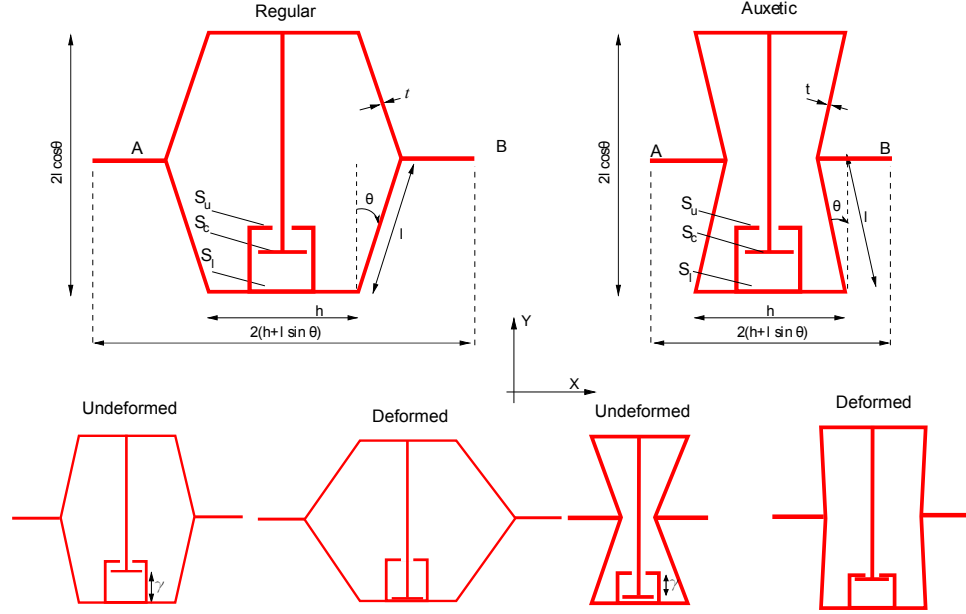


**Figure 3.1.** Geometry and nomenclature of a contact-aided compliant unit cell

oblique members is  $l$ . The in-plane thickness of the structural members is  $t$ . The out-of-plane thickness of the structure is  $w$ . The angle that an oblique wall makes with a vertical line is denoted by  $\theta$ . There are two possible variations of the cell: regular (Figure 3.1, left - having a positive value of  $\theta$ ) and auxetic (Figure 3.1, right - having a negative value of  $\theta$ ). The regular cell exhibits positive Poisson's ratio, and therefore if points A and B are moved away from each other in the X-direction, then the surface  $S_c$  will contact  $S_l$ . The auxetic cell exhibits negative Poisson's ratio, and therefore if points A and B are moved away from each other in the X-direction, surface  $S_c$  will contact  $S_u$ . The initial distance (before deformation) between  $S_c$  and the surface where it makes contact after the deformation is called the 'initial contact gap' and is denoted by  $\gamma$ .

### 3.2.2 Finite Element Analysis

To find the maximum stresses for a prescribed global deformation of a contact-aided compliant structure, finite element procedures can be used. To emulate the cellular nature of the structure, the unit cells were arranged in an array as shown in Figure 3.2 and analyzed using ANSYS as a finite element solver. Each cell wall

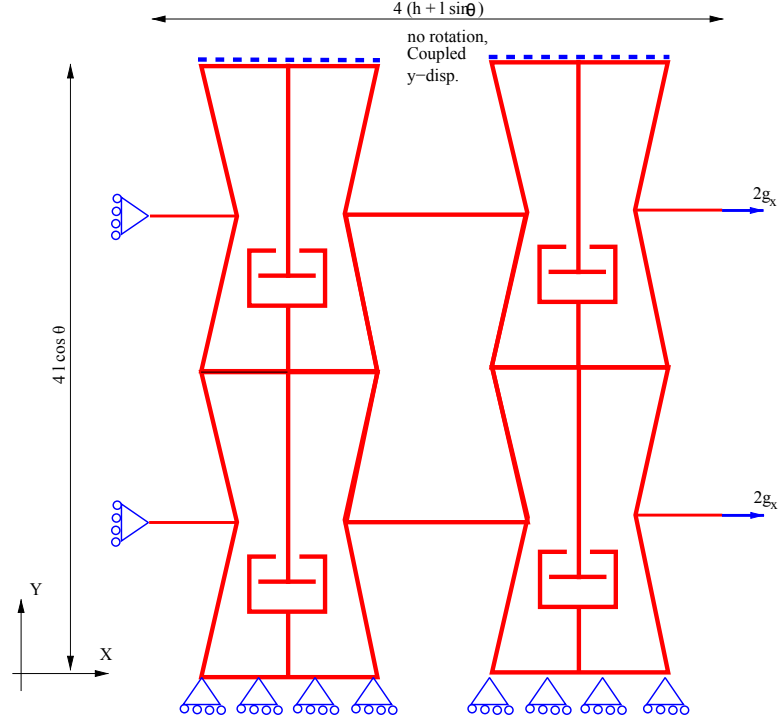
is modeled using beam elements (BEAM23). This element is a 2-D Timoshenko beam element that allows analysis with large deflection, shear effect, and contact elements. Contact is modeled using CONTA172 (for  $S_c$ ) along with TARGE169 as target elements (for  $S_u$  and  $S_l$ ).

Figure 3.2 shows the boundary conditions imposed on the structure to represent an infinite sheet in 2-D. The bottom-most cell walls are constrained to move only in the X-direction, and the top-most cell walls are constrained to move together in the Y-direction. The left-most nodes are fixed in the X-direction and a displacement constraint is applied at the right-most nodes (denoted by  $2g_x$ , where  $g_x$  is the tensile deformation per unit cell). This displacement is incremented until the maximum local tensile stress has reached or is near the allowable value. For the contact-aided compliant cells, the initial contact gap is set so that contact occurs and provides stress relief. Because of stress relief the structure can withstand more deformation than it could without contact. The deformation is further increased until the maximum axial stress in the oblique wall reaches the buckling stress. In this portion of the work only linearly elastic materials are considered.

Consistent with the literature [4, 7, 18], the global strain of non-contact cellular structures in the X-direction is related to  $g_x$  as the following.

$$\epsilon_x^{global} = \frac{2g_x}{4(h + l \sin \theta)} = \frac{g_x}{2(h + l \sin \theta)} \quad (3.1)$$

To demonstrate the concept of stress relief, a contact-aided structure similar to that shown in Figure 3.2 is considered. The unit cell has a cell angle ( $\theta$ ) of -27 deg. and lengths  $l$ ,  $h$  are 10 mm each. Thicknesses  $w$  and  $t$  are 10 mm and 1 mm, respectively. For a material having an elastic modulus of 1.4 GPa and a yield stress of 43 MPa, the normalized maximum tensile bending stress and the maximum axial stress in the oblique wall as a function of global strain is shown in Figure 3.3. If a contact mechanism is not present in a cellular structure, the cellular structure is termed a ‘non-contact’ structure. Prior to contact (i.e.,  $< 13\%$  global strain), the bending and axial stresses in the contact-aided structure and the non-contact structure are exactly the same. Once contact takes place (here  $\gamma = 0.62$  mm and  $S_c$  contacts  $S_u$  because  $\theta < 0$ ), the axial stress increases substantially in the structure. The axial stress reduces the tensile bending stresses that can cause



**Figure 3.2.** Cellular structure and boundary conditions applied for FE simulation

structural failure either by yielding or by fracture. This enables the contact-aided structure to sustain a larger global strain than a non-contact structure with the same dimensions. In this particular case, the non-contact structure has a maximum global strain of 18 % and the contact-aided structure has a maximum global strain of 27 %, as shown when  $\sigma/\sigma_{all} = 1$  in Figure 3.3.

Evidently, for regularly shaped cells the contact mechanism experiences compression and the oblique walls experience tensile axial stress, while for auxetic cells the contact-mechanism undergoes tension and the oblique walls experience compressive axial stress. To reduce the tensile bending stress, compressive axial loads are required. Therefore auxetic cells provide a unique opportunity for stress relief. Moreover, as per the literature [7, 18], the maximum allowable global strains for regular cells are lower than those of auxetic cells even for non-contact structures.

The dotted lines in Figure 3.3 show the maximum von Mises stress in the structures. Many engineering materials including alloys, ceramics, and some polymers fail at a critical tensile stress. For other materials such as ductile polymers, von

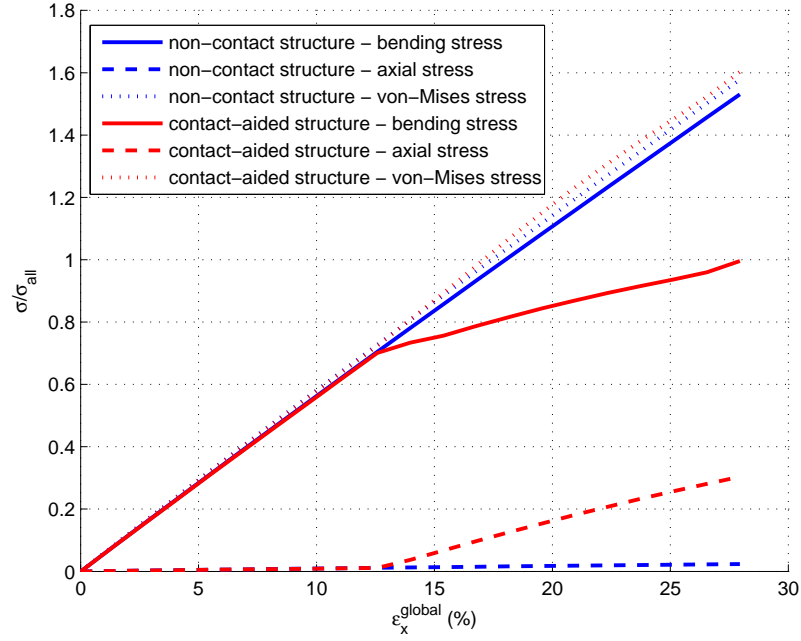


**Figure 3.3.** Stress history for non-contact and contact-aided cellular structure

Mises stress governs the material failure. In the present analysis, it is assumed that the material failure is due to a normal stress.

### 3.2.3 Prototype

To demonstrate the concept of a contact-aided mechanism, a prototype was made. Commercially available plastic, Delrin 100st, was used for the fabrication. The prototype was manufactured using a laser cutting machine. Two photos of this prototype are shown in Figure 3.4. The global strain observed with this prototype was approximately 45%. The figure also demonstrates how different cell walls deform as well as the working of the contact mechanism. The left-most points as well as the right-most points of this prototype are constrained together. These points, therefore, cannot move freely in the lateral direction as opposed to the model used for analysis (see Figure 3.2). The horizontal walls corresponding to these points bend while stretched. Moreover, due to manufacturing imperfections, the oblique walls on left side are thicker than those on right side. The oblique



**Figure 3.4.** Delrin prototype of the contact-aided compliant structure: Left photo shows initial configuration and right photo shows deformed configuration and contact

walls on right side are more compliant, and, therefore, bend more than those on left side. Experimental evaluation of cellular contact-aided mechanisms is discussed in Section 3.5.

### 3.3 Analytical Model

An analytical model was developed to predict the maximum elastic global strain based on the deformation and stress in cell walls. The analytical model includes contact. As it is shown later, this model has good accuracy and can effectively replace the computationally expensive finite element (FE) analysis.

#### 3.3.1 Large Deflection Approximation

A deformation model for non-contact structures based on linear, small deflection theory has been reported in the literature (e.g., [4], [65], [7], [18]). An exhaustive deformation model for non-contact structures based on an elliptic integral formulation for large deflections is also available [83]. For high-strain structures, a linear

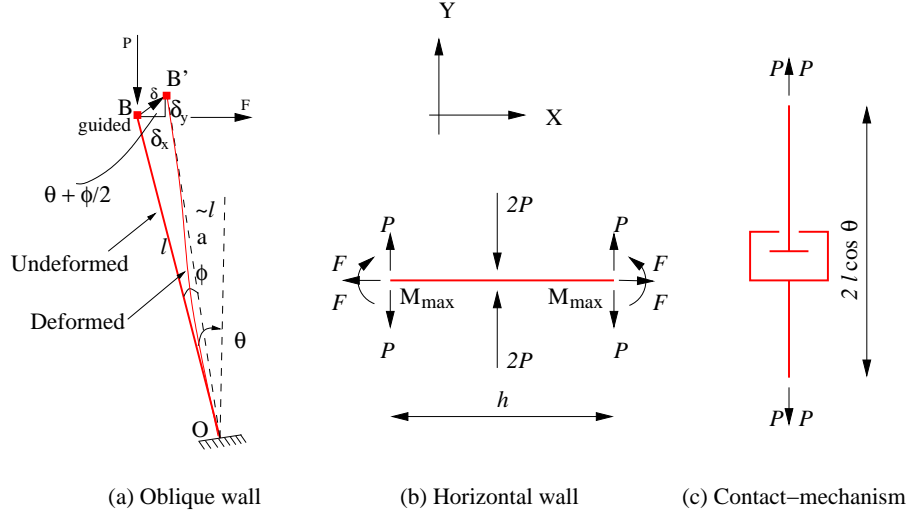


**Figure 3.5.** Free body diagrams of the cell walls

theory may not be accurate enough. On the other hand, when designing such structures, the elliptic integral formulation may not be computationally efficient. A new model is developed here that accounts for both large deflections and contact, which have not been considered together in the literature. Two independent approaches are used to model large deflection.

When displacements are applied in the X-direction, the oblique walls – those having length  $l$  – bend; and the horizontal walls – those having length  $h$  – stretch. The free body diagram of an oblique (lower) wall undergoing bending is shown in Figure 3.5(a). Note that for auxetic cells,  $\theta$  shown here has a negative value.  $F$  represents the load applied to bend this member and  $P$  represents the additional load due to the contact mechanism after contact has taken place. After deformation, point B moves to B' making the total deflection  $\delta$ . The components of  $\delta$  in the X-direction and the Y-direction are denoted by  $\delta_x$  and  $\delta_y$  respectively. The angle change subtended by points B to B' with respect to the root of the wall, O, is given by  $\phi$ . If one assumes that the length of segment OB' remains approximately the same as OB (i.e.  $\sim l$ ), the angle between  $\delta$  and  $\delta_x$  is  $\theta + \phi/2$ . Therefore,

$$\phi \approx \delta/l \quad (3.2)$$

and

$$\delta_x \approx \delta \cos(\theta + \phi/2) = \delta \cos(\theta + \delta/2l) \quad (3.3)$$

$$\delta_y \approx \delta \sin(\theta + \phi/2) = \delta \sin(\theta + \delta/2l) \quad (3.4)$$

In other words, an average angle is used to find the components of the displacement. The Y-displacement found using this approach is less accurate than the X-displacement as shown in Table 3.1. In an alternative approach, the length of segment OB' is  $a$ , and the perpendicular distance from B' to OB is  $b$  such that  $\phi = \arctan(b/a)$ . It implies

$$\delta_x = \sqrt{a^2 + b^2} \sin(\theta + \phi) - l \sin \theta \quad (3.5)$$

$$\delta_y = \sqrt{a^2 + b^2} \cos(\theta + \phi) - l \cos \theta \quad (3.6)$$

The pseudo-rigid-body model [84] is used to approximate the behavior of a continuum beam undergoing large deflections. If  $\Theta$  is the rigid-body angle and  $\Gamma l$  is the length of an equivalent rigid-body link, the following expressions are found as the following.

$$a = l [1 - \Gamma (1 - \cos \Theta)] \quad (3.7)$$

$$b = l \Gamma \sin \Theta \quad (3.8)$$

Substituting these equations into Eqns. 3.5 and 3.6,

$$\delta_x = l \sqrt{1 - 2\Gamma + 2\Gamma^2 - 2(\Gamma - 1)\Gamma \cos \Theta} \cdot \sin \left[ \theta + \arctan \left( \frac{\Gamma \sin \Theta}{1 - \Gamma + \Gamma \cos \Theta} \right) \right] - l \sin \Theta \quad (3.9)$$

$$\delta_y = l \sqrt{1 - 2\Gamma + 2\Gamma^2 - 2(\Gamma - 1)\Gamma \cos \Theta} \cdot \cos \left[ \theta + \arctan \left( \frac{\Gamma \sin \Theta}{1 - \Gamma + \Gamma \cos \Theta} \right) \right] - l \cos \Theta \quad (3.10)$$

$\Gamma$  is given as a function of the ratio of lateral and axial load on the beam. However, for simplicity, it is assumed to be constant at 0.8517 [84].



**Table 3.1.** Error in displacements predicted using two approximations

$k$	$\theta$ (deg.)	$\delta/l$	error in x (%)	error in y (%) (using $\phi$ )	error in y (%) (using PRBM)
0	-30	0.22	1.07	6.10	0.91
		0.42	1.36	16.3	2.33
	0	0.20	0.20	15.1	0.21
		0.41	0.87	15.2	2.13
3	-30	0.21	0.58	17.3	11.3
		0.41	2.00	27.2	12.1
	0	0.30	1.09	27.4	13.6
		0.41	1.61	23.5	7.80

Eqn. 3.3 is used to determine the deflection in the X-direction given the total deflection of point B. Eqn. 3.9 can then be solved to find the rigid-body angle  $\Theta$  for this particular deformation. Finally Eqn. 3.10 is used to estimate the deflection in the Y-direction. To check the accuracy of the preceding approximations, the inclined cell wall is individually analyzed. One end of the wall is fixed while the other is constrained in rotations (guided) as shown in Figure 3.5(a). The guided end is subjected to a lateral and an axial load. The total displacement of the guided end ( $\delta$ ), X-displacement ( $\delta_x$ ) and Y-displacement ( $\delta_y$ ) are monitored. The beam is modeled in ANSYS using BEAM23 elements and solved assuming large deflections. Only  $\delta$  from this simulation is used in the preceding approximations to get an estimate of  $\delta_x$  and  $\delta_y$ . These estimates are compared with FEA results and presented in Table 3.1, where  $k^2 = Pl^2/EI$ . The results indicate that the estimated X-displacement is very accurate, while the Y-displacement estimated using pseudo-rigid-body model (PRBM) has an error  $< 15\%$ .

### 3.3.2 Global Strain

As the deformation increases, the stresses in the structure tend to increase as well. So it is initially assumed that the maximum stress is experienced when the deformation is also the largest. The angle made by  $F$  with the deformed oblique wall is then  $\pi/2 - \theta + \phi$ . The effective lateral ( $F_n$ ) and axial load ( $F_a$ ) on an oblique wall are

$$F_a = -F \sin(\theta + \phi) + P \cos(\theta + \phi) \quad (3.11)$$

$$F_n = F \cos(\theta + \phi) + P \sin(\theta + \phi) \quad (3.12)$$

For the beam under consideration, the total deflection of point B is given by [9] as the following.

$$\delta = \frac{F_n}{-kF_a} \left( 2 \tan \frac{kl}{2} - kl \right) \quad (3.13)$$

where  $k = \sqrt{\frac{F_a}{EI}}$  and  $E$ ,  $I = bt^3/12$  are the modulus of elasticity and the area of moment of inertia for the beam, respectively. The external loads generate a bending moment in the beam. Its maximum value is given by the following expression.

$$M_{max} = \frac{F_n}{k} \tan \frac{kl}{2} \quad (3.14)$$

This bending moment causes bending stress in the wall. Using the flexure formula for the combined loading of bending and axial stress [85],

$$\sigma_{max} + \sigma_{ax} = \frac{M_{max}t/2}{I} \quad (3.15)$$

where  $\sigma_{max}$  and  $\sigma_{ax}$  are the maximum bending tensile stress and axial direct stress in the beam. From Eqns. 3.14 and 3.15, solving for  $F_n$ ,

$$F_n = \frac{bt^2}{6} \frac{k(\sigma_{max} + \sigma_{ax})}{\tan \frac{kl}{2}} \quad (3.16)$$

The axial stress is related to the axial load as

$$F_a = \sigma_{ax}bt \quad (3.17)$$

Substituting the preceding equations into Eqn. 3.13 and simplifying,

$$\delta = \frac{t}{3} \left( 1 + \frac{\sigma_{max}}{\sigma_{ax}} \right) \left( 1 - \frac{\frac{1}{t/l} \sqrt{\frac{3\sigma_{ax}}{E}}}{\tan \left( \frac{1}{t/l} \sqrt{\frac{3\sigma_{ax}}{E}} \right)} \right) \quad (3.18)$$

This equation provides a relationship between the total bending deflection and the stress state in the beam. The deformation in the X-direction, therefore, can be found using Eqn. 3.3. In addition to bending, the horizontal walls (having length  $h$ ) can stretch. Solving Eqns. 3.11 and 3.12 simultaneously for  $F$ ,

$$F = -F_a \sin(\theta + \phi) + F_n \cos(\theta + \phi) \quad (3.19)$$

$F_n$  and  $F_a$  can be substituted as a function of the stress state using Eqns. 3.16 and 3.17, respectively. The free body diagram of a horizontal wall is shown in Figure 3.5(b). The stretching of the horizontal wall is given by

$$\begin{aligned} \delta_x^s = & 2h \left[ -\frac{\sigma_{ax}}{E} \sin(\theta + \phi) \right] + \\ & 2h \left[ \frac{1}{3} \frac{\sigma_{max} + \sigma_{ax}}{E} \frac{\sqrt{\frac{3\sigma_{ax}}{E}} \cos(\theta + \phi)}{\tan \left( \frac{1}{t/l} \sqrt{\frac{3\sigma_{ax}}{E}} \right)} \right] \end{aligned} \quad (3.20)$$

The combined bending and stretching of cell walls results in the half-cell deformation,

$$g_x/2 = \delta_x + \delta_x^s \quad (3.21)$$

Using Eqn. 3.1, an expression for the global strain may be written as in Eqn. 3.22.

$$\epsilon_x^{global} = \Pi_1 \{ \Pi_2 \sin(\theta + \Pi_2/2) + \Pi_4 \} \quad (3.22)$$

where

$$\begin{aligned} \Pi_1 &= \frac{1}{h/l + \sin \theta} \\ \Pi_2 &= \frac{1}{3} \frac{t}{l} \left( 1 + \frac{\sigma_{max}/E}{\sigma_{ax}/E} \right) \left( 1 - \frac{\frac{1}{t/l} \sqrt{\frac{3\sigma_{ax}}{E}}}{\tan \left( \frac{1}{t/l} \sqrt{\frac{3\sigma_{ax}}{E}} \right)} \right) \end{aligned}$$

$$\begin{aligned}\Pi_3 &= \frac{1}{3} \left( \frac{\sigma_{max}}{E} + \frac{\sigma_{ax}}{E} \right) \frac{\sqrt{\frac{3\sigma_{ax}}{E}}}{\tan \left( \frac{1}{t/l} \sqrt{\frac{3\sigma_{ax}}{E}} \right)} \\ \Pi_4 &= 2 \frac{h}{l} \left[ -\frac{\sigma_{ax}}{E} \sin(\theta + \Pi_2) + \Pi_3 \cos(\theta + \Pi_2) \right]\end{aligned}$$

### 3.3.3 Contact Gap

The initial contact gap can be determined using the deformation of the cell in the Y-direction. The X-displacement due to bending ( $\delta_x$ ) is substituted in Eqn. 3.9, which is solved numerically for  $\Theta$ . In the present work MATLAB's root finding tool, `fsolve`, is used for the numerical solution. The result is then used in Eqn. 3.10 to obtain the Y-displacement due to bending. The cell wall is also under compressive load causing a contraction  $= l\sigma_{ax}/E$  in the direction of the beam. The net displacement of point B in the Y-direction is the sum of a bending displacement and a contraction.

$$\delta_y^B = \delta_y - l \frac{\sigma_{ax}}{E} \cos(\theta + \phi) \quad (3.23)$$

The total separation between two horizontal walls will then be twice this value. Once contact has taken place, the two horizontal members can still move in the Y-direction because of the stretching of the contact mechanism. The free body diagram of the contact mechanism under load is shown in Figure 3.5(c). The axial force acting on the mechanism ( $P$ ) is obtained by solving Eqns. 3.11 and 3.12, and is given by

$$P = F_a \cos(\theta + \phi) + F_n \sin(\theta + \phi) \quad (3.24)$$

The stretching of the contact mechanism can now be expressed as a function of the stress-state as

$$\begin{aligned}\delta_y^s &= 2l \cos(\theta + \phi) \frac{2P}{Ebt} \\ &= 4l \cos(\theta + \phi) \times \\ &\quad \left[ \frac{\sigma_{ax}}{E} \cos(\theta + \phi) + \frac{1}{3} \frac{\sigma_{max} + \sigma_{ax}}{E} \frac{\sqrt{\frac{3\sigma_{ax}}{E}} \sin(\theta + \phi)}{\tan \left( \frac{1}{t/l} \sqrt{\frac{3\sigma_{ax}}{E}} \right)} \right]\end{aligned} \quad (3.25)$$

Finally, the contact gap is found by subtracting this stretching of the contact mechanism from the total separation ( $2\delta_s^B$ ). The non-dimensional initial contact gap is then given in Eqn. 3.26.

$$\frac{\gamma}{l} = \Pi_6 - \Pi_7 - 4\Pi_8 \cos(\theta + \Pi_2) \quad (3.26)$$

where

$$\begin{aligned} \Pi_5 &= \sqrt{1 - 2\Gamma + 2\Gamma^2 - 2(\Gamma - 1)\Gamma \cos \Theta} \\ \Pi_6 &= 2\Pi_5 \cos \left[ \theta + \arctan \left( \frac{\Gamma \sin \Theta}{1 - \Gamma + \Gamma \cos \Theta} \right) \right] - 2 \cos \Theta \\ \Pi_7 &= 2 \frac{\sigma_{ax}}{E} \cos(\theta + \phi) \\ \Pi_8 &= \frac{\sigma_{ax}}{E} \cos(\theta + \Pi_2) + \Pi_3 \sin(\theta + \Pi_2) \end{aligned}$$

Evidently, Eqns. 3.22 and 3.26 depend only on non-dimensional quantities such as  $h/l$ ,  $t/l$ ,  $\sigma_{max}/E$ ,  $\sigma_{ax}/E$  and  $\theta$ .

### 3.3.4 Maximum Global Strain

The analytical model developed thus far assumes that the stress state in the structure is known. To design a contact-aided compliant mechanism one can dictate the maximum tensile stress ( $\sigma_{max}$ ) be the material allowable value (i.e., yield or ultimate stress,  $\sigma_{all}$ ). However, various geometric and material constraints are used to find the maximum value for the axial stress.

For non-contact structures, the only external force acting on the structure is  $F$ . Equating moments from Eqns. 3.14 and 3.15 and letting  $P = 0$  for non-contact structures, one obtains

$$\left( \frac{\sigma_{max}}{E} + \frac{\sigma_{ax}}{E} \right) \tan \theta + \sqrt{3 \frac{\sigma_{ax}}{E}} \tan \left( \frac{1}{t/l} \sqrt{3 \frac{\sigma_{ax}}{E}} \right) = 0 \quad (3.27)$$

Here  $\phi$  is neglected for simplicity. This equation can be numerically solved for  $\sigma_{ax}$ , which is substituted in Eqn. 3.22 to calculate the maximum allowable global strain ( $\epsilon_{x,max}^{global}$ ) for non-contact structures.

For contact-aided structures, the contact-induced axial stress in the oblique wall is positive only when  $\theta < 0$ , assuming that the overall deformation includes only stretching in the X-direction. To utilize stress relief, the maximum possible angle change is therefore  $\theta$ . In such a case, the total possible deformation in the X-direction will be  $g_x/2 = -l \sin \theta$ . The geometrically allowed maximum global strain is then

$$\epsilon_{x,\max}^{global} = -\frac{\sin \theta}{h/l + \sin \theta} \quad (3.28)$$

This strain is substituted in Eqn. 3.22, which is solved for  $\sigma_{ax}$  numerically. Eqn. 3.26 can further be used to find the required contact gap. In some cases, though, the axial stress required for such a deformation may be greater than that which the structure can handle without buckling. The buckling load for a fixed-guided beam, as shown in Figure 3.5(a), is given by [85]

$$F_a^{buck} = \pi^2 \frac{EI}{l^2} = \frac{\pi^2}{12} \left(\frac{t}{l}\right)^2 Ebt \quad (3.29)$$

The axial stress at the buckling load is

$$\sigma_{ax}^{buck} = \frac{\pi^2}{12} \left(\frac{t}{l}\right)^2 E \quad (3.30)$$

This value is used in Eqns. 3.22 and 3.26 to find the maximum allowable global strain and the corresponding initial contact gap.

The contact gap found using this method may not be practically possible (either too small to manufacture or negative). Therefore a lower limit on the initial contact gap ( $\gamma_{\min}$ ) is imposed. If  $\gamma$  is calculated to be smaller than  $\gamma_{\min}$ , the latter value is substituted in Eqn. 3.26 and the equation is solved numerically for  $\sigma_{ax}$ , which can be used to find the corresponding  $\epsilon_x^{global}$  using Eqn. 3.22.

### 3.4 Results for Maximum Global Strain

The proposed cellular structure and the developed model can be used for any linearly elastic material. For comparison, two materials are considered here. One material has a relatively high elastic strain capability (polymer) and the other

material has a low elastic strain (ceramic). The results for various non-dimensional parameters are presented.

### 3.4.1 Delrin

Delrin is a commercially available engineering thermoplastic from Dupont, Inc. Delrin as a plastic material exhibits a nonlinear stress-strain relation. The nonlinear elastic strain at yield is 30%, corresponding to the yield stress of 43 MPa [12]. To linearize, the initial slope of the stress-strain curve is assumed to be the modulus of elasticity, while the yield stress is assumed to be the same. Thus the linearized properties of Delrin 100st are assumed to be  $E = 1.4$  GPa and  $\sigma_{all} = 43$  MPa, so  $\sigma_{all}/E = 0.0307$ .  $\gamma_{min}/l$  is taken to be  $\sim 0.025$ . For different values of ratio  $h/l$  (0.5, 1.0 and 2.0) and  $t/l$  (0.05, 0.07 and 0.10) a variation of  $\epsilon_{x,max}^{global}$  per unit material allowable strain ( $\sigma_{all}/E$ ) with the cell angle is shown in Figure 3.6.  $\sigma_{all}/E$  is the allowable strain of the material, which is usually small. The  $\epsilon_{x,max}^{global}/(\sigma_{all}/E)$  ratio shown in the plot can be thought of as an “amplification factor” – a higher ratio implies more amplification of the material allowable strain in the effective global strain. At an angle  $\theta_{min} = -\arcsin(h/2l)$ , two oblique walls of a unit cell will be nearly touching each other [18]. This angle is used as the minimum cell angle in all subsequent plots.

Figure 3.6 indicates that the cellular structure provides greater global strain for smaller cell angle, thinner cell walls and narrower cell sizes ( $h/l$ ), which is true for structures with or without a contact mechanism. The contact-aided cellular structure exhibits more global strain than the corresponding non-contact structure in this region. For the given range of non-dimensional parameters, the non-contact structures provide a maximum of 74% global strain (when  $h/l = 0.5$ ,  $t/l = 0.05$ , and  $\theta = -13\text{deg.}$ ) and the contact-aided structures provide a maximum of 83% (when  $h/l = 0.5$ ,  $t/l = 0.05$ , and  $\theta = -13\text{deg.}$ ) global strain. Since contact-aided structures apparently sustain more global strain than a corresponding cellular structure without contact, one can find maximum improvement in the global strain with respect to the non-contact structures. When  $h/l = 2.0$ ,  $t/l = 0.10$ , and  $\theta = -30\text{deg.}$ , as high as 67% improvement in global strain is possible using a contact mechanism due to the induced stress relief.

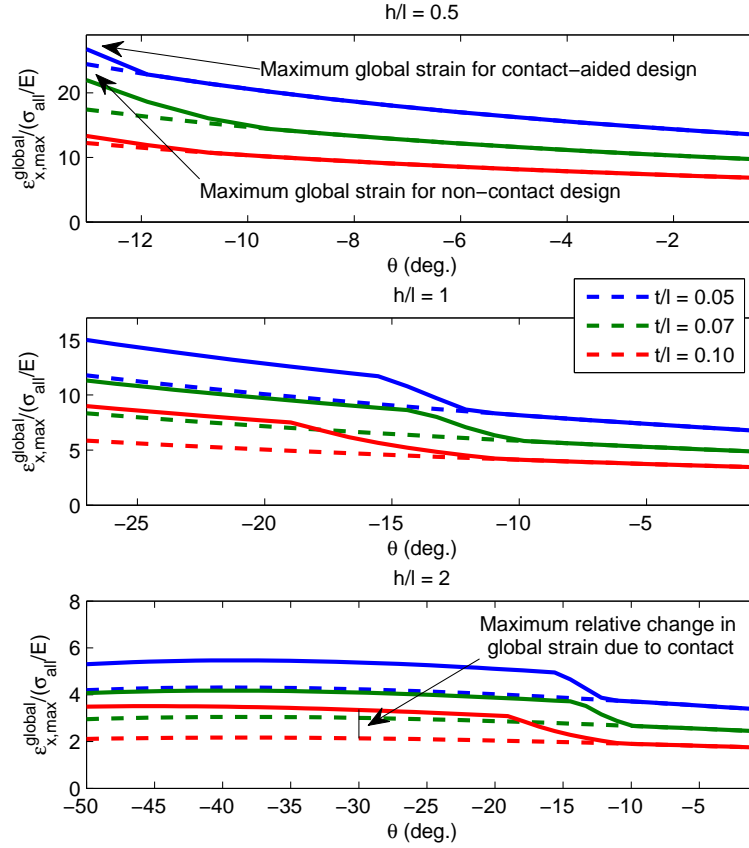


**Figure 3.6.** Variation of global strain per unit material strain with cell angle for Delrin (solid line - contact-aided structure, dashed like - non-contact structure)

### 3.4.2 Zirconia

A ceramic material, 3YSZ (3% mol fraction yttria stabilized zirconia), is also considered. The ceramic itself can sustain a very small elastic tensile strain before fracture. However, meso-scaled ceramic components are being developed that exhibit high strength [49, 50, 60]. Assuming properties reported for nano-particulate Zirconia [49, 50]:  $E = 200$  GPa and  $\sigma_{all} = 670$  MPa, so  $\sigma_{all}/E = 0.00335$ .  $\gamma_{min}/l$  is taken be  $\sim 0.025$ . For different values of  $h/l$  (0.8, 1.0 and 1.2) and  $t/l$  (0.04, 0.05 and 0.06) the variation of  $\epsilon_{x,max}^{global}$  per  $\sigma_{all}/E$  with the cell angle is shown in Figure 3.7.



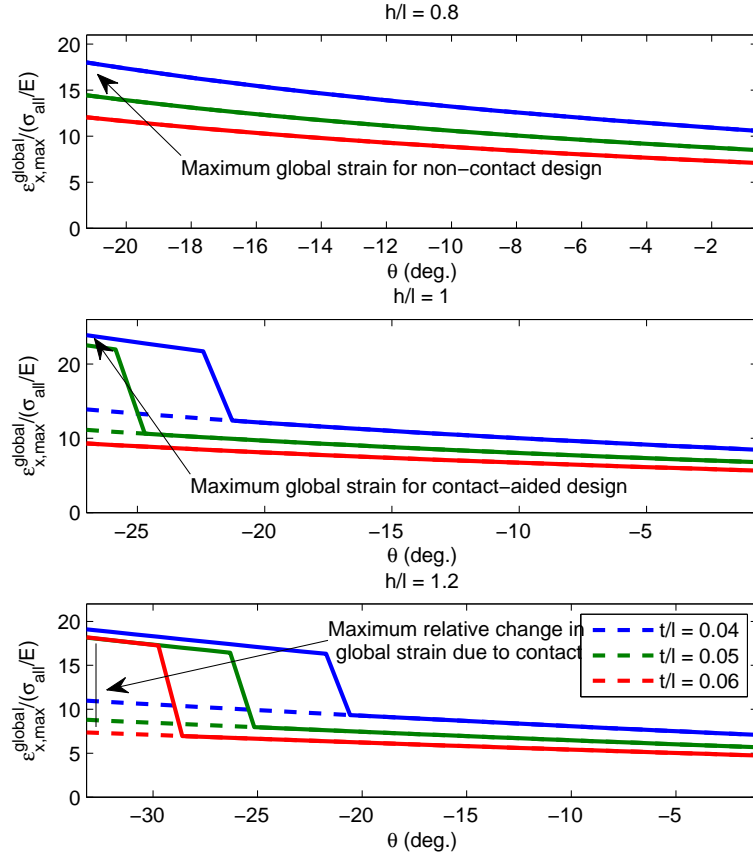


**Figure 3.7.** Variation of global strain per unit material strain with cell angle for Zirconia (solid line - contact-aided structure, dashed line - non-contact structure)

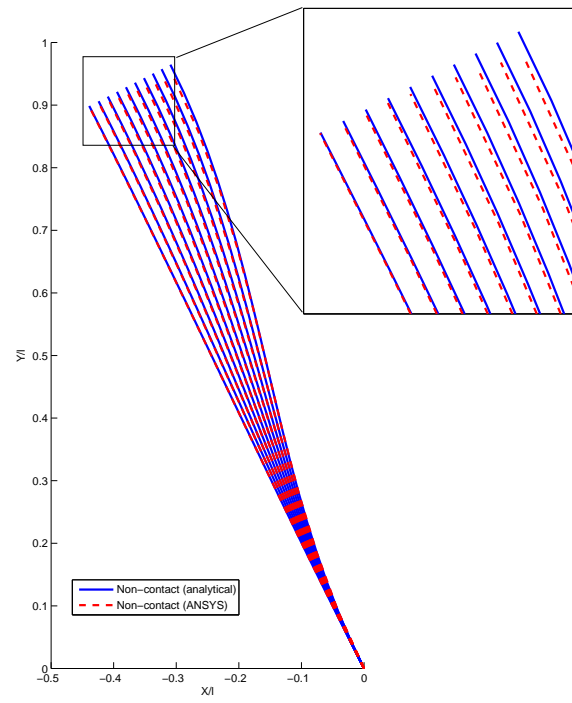
The variations in the global strain for Zirconia are similar to those for Delrin. In the considered range of non-dimensional parameters, non-contact structures provide a maximum of 5.4% global strain (when  $h/l = 0.8$ ,  $t/l = 0.04$ , and  $\theta = -21$ deg.), while contact-aided structures provide a maximum of 7.2% global strain (when  $h/l = 1.0$ ,  $t/l = 0.04$ , and  $\theta = -27$ deg.). When  $h/l = 1.2$ ,  $t/l = 0.06$ , and  $\theta = -32$ deg., as high as 143% improvement in global strain is possible using a contact mechanism and the induced stress relief.

### 3.4.3 Validation

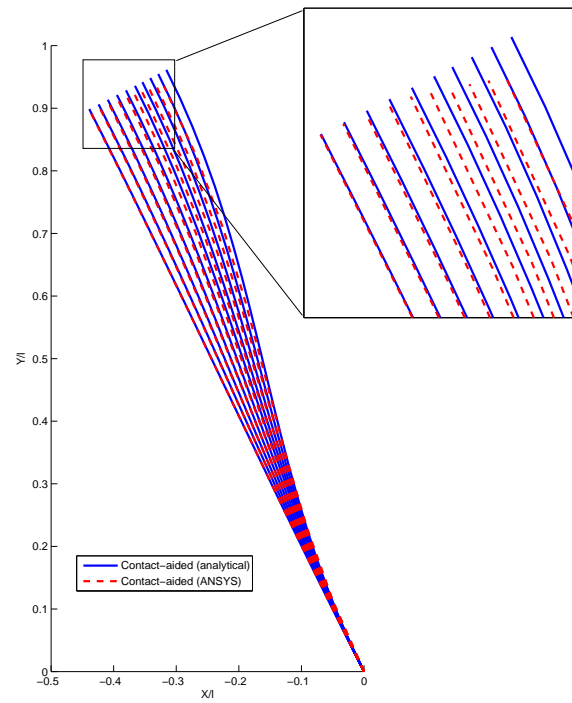
The predicted maximum global strain for various non-dimensional parameters was validated using finite element (FE) simulation. In the FE simulation, the external displacement ( $g_x$ ) was incremented until the tensile stresses were at or near the allowable value. For non-contact structures this value of  $g_x$  is used to calculate the maximum allowable global strain. For contact-aided structures  $g_x$  is still increased and  $\gamma$  is decreased until contact occurs. This process is continued until either: the overall strain of the structure reaches its geometrical maximum value (Eqn. 3.28); the axial stress reaches a value needed to induce buckling (Eqn. 3.30); or  $\gamma$  is near or equal to  $\gamma_{\min}$ . In each case the required initial contact gap is also recorded.

Figs. 3.6 and 3.7 are used to find the value of  $\theta$  at which global strains are maximum for given  $h/l$  and  $t/l$ , respectively. The global strains for such cases are given in Table 3.2 and 3.3 respectively. Different results such as the maximum amplification in the overall elastic strain and the advantage of contact-aided structures over non-contact structures are also summarized in Table 3.4. The table presents the maximum percentage error in predicting the global strain and the contact gap using the analytical model as compared to the FE results. To calculate the maximum global strain for a set of non-dimensional parameters, FE analysis requires about 2-3 hours. The analytical model takes approximately 4-5 seconds to generate similar results with acceptable accuracy. Such model can now be used as a substitution for FE simulation to reduce the computational cost. The analytical model also provides physical insight into the mechanics of the contact-aided structures and the stress relief.

The deformed shapes of an oblique member throughout the loading using both the analytical model and ANSYS are shown in Figure 3.8. The material was assumed to be Delrin and  $h/l = 1.0$ ,  $t/l = 0.10$ , and  $\theta = -27\text{deg}$ . The non-contact as well as contact-aided shapes are compared and both models, evidently, match very closely.



(a) Non-contact oblique wall



(b) Contact-aided oblique wall

**Figure 3.8.** Comparison of deformed shapes from analytical model with finite element analysis

**Table 3.2.** Validation of maximum strains for Delrin

$h/l$	$t/l$	$\theta$ (deg.)	$\epsilon_{x,\max}^{global}/(\sigma_{max}/E)$		$\gamma/l$
			Non-contact	Contact-aided	
			Theory	Theory	Theory
			FEA	FEA	FEA
0.5	0.05	-13	24.4	26.7	0.035
			24.2	26.6	0.037
0.5	0.07	-13	17.4	21.9	0.026
			17.3	21.1	0.025
0.5	0.10	-13	12.2	13.3	0.025
			12.1	13.2	0.026
1.0	0.05	-27	11.8	15.0	0.152
			11.7	15.8	0.148
1.0	0.07	-27	8.34	11.3	0.116
			8.35	12.2	0.112
1.0	0.10	-27	5.9	9.0	0.071
			5.8	10.1	0.065
2.0	0.05	-30	4.2	5.4	0.178
			4.2	5.7	0.179
2.0	0.07	-30	3.0	4.1	0.136
			3.0	4.4	0.141
2.0	0.10	-30	2.1	3.3	0.087
			2.1	3.5	0.092

### 3.5 Experiments

To observe the stress relief and to validate the simulation, experiments were conducted. This section describes the experimental setup and salient results.

**Table 3.3.** Validation of maximum strains for Zirconia

$h/l$	$t/l$	$\theta$ (deg.)	$\epsilon_{x,\max}^{global}/(\sigma_{max}/E)$		$\gamma/l$
			Non-contact	Contact-aided	
			Theory FEA	Theory FEA	Theory FEA
0.8	0.04	-20	17.4	17.4	-
			17.4	17.4	-
0.8	0.05	-20	13.9	13.9	-
			13.9	13.9	-
0.8	0.06	-20	11.6	11.6	-
			11.6	11.6	-
1.0	0.04	-27	13.9	23.9	0.034
			13.9	24.8	0.032
1.0	0.05	-27	11.1	22.5	0.027
			11.1	24.2	0.026
1.0	0.06	-27	9.3	9.3	-
			9.3	9.3	-
1.2	0.04	-30	10.6	18.3	0.038
			10.6	20.1	0.038
1.2	0.05	-30	8.5	17.3	0.032
			8.5	18.1	0.030
1.2	0.06	-30	7.1	17.3	0.026
			7.1	19.0	0.026

**Table 3.4.** Summary of results for various materials

Material	$\sigma_{all}/E$	$\frac{\epsilon_x^{global}}{\sigma_{all}/E}$	Benefit of contact	% prediction error	
	%		Max. %	in $\epsilon_x^{global}$	in $\gamma/l$
Delrin	3.1	27	67	10	9
Zirconia	0.3	24	143	11	7

**Table 3.5.** Geometrical parameters for different experimental specimens

	Sample A		Sample B	
	non-contact	contact-aided	non-contact	contact-aided
$\theta$	$-30^\circ$	$-30^\circ$	$-30^\circ$	$-30^\circ$
$l$	40 mm	40 mm	40 mm	40 mm
$h$	50 mm	50 mm	50 mm	50 mm
$t$	1.55 mm	1.55 mm	1.50 mm	1.50 mm
$w$	1.05 mm	1.05 mm	1.70 mm	1.70 mm
$\gamma$	-	2.9 mm	-	2.8 mm

### 3.5.1 Experimental Setup

Commercially available 7075-T6 aluminum was used to fabricate a five-cell model as represented in Figure 3.2. The modulus of elasticity and the yield stress were assumed to be 68 GPa and 550 MPa, respectively. Two sets of such samples were made using the water-jet machining process. Note that, similar to delrin prototypes, the left-most and the right-most horizontal points are constrained together. This allows using the clamps readily available for the tensile testing machine. Their geometrical parameters are summarized in Table 3.5.

The experimental setup is shown in Figure 3.9. A screw-driven Instron 5866 material testing machine was used for the experiments. A 1 kN load cell was used. The loading speed used was 2 mm/min. The extension of the structure is measured using the built-in sensor of the testing system.

### 3.5.2 Results

The first set of experiments, involving samples A, were tested to observe the stress relief. The cellular structures, both non-contact and contact-aided, were stretched to a specified deformation. This loaded deformation divided by the original length of the overall structure gives the global strain. The load was removed, and the unloaded length was measured. The difference between the unloaded length and the initial length is a measure of yielding. This difference is normalized by the initial length and called ‘residual strain.’ The process is repeated for increasing

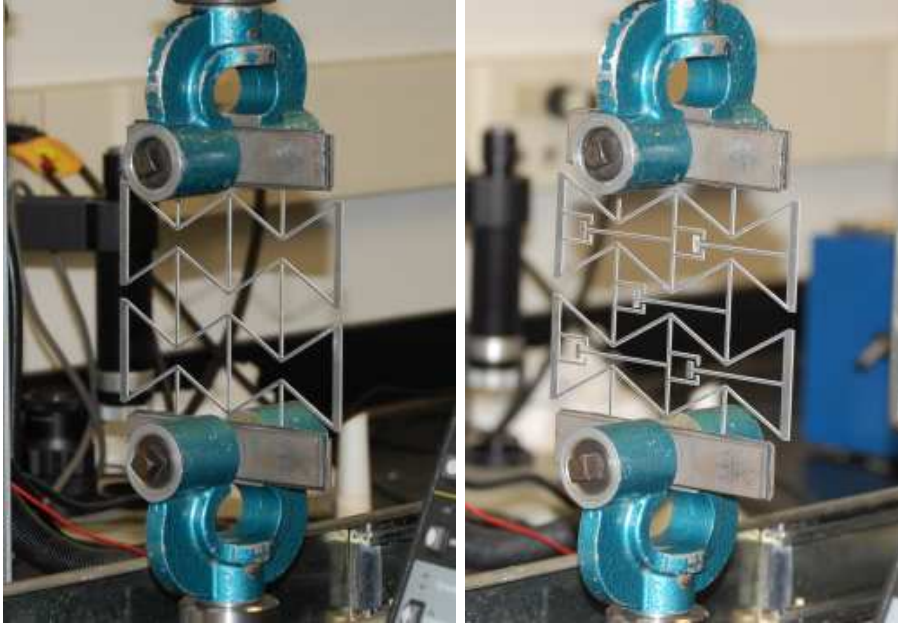


**Figure 3.9.** Experimental setup and the aluminum models, without (left) and with (right) the contact mechanism

levels of stretching. The variation of residual strain with global strain is plotted in Figure 3.10.

It is customary to measure yield stress at 0.2% offset in a stress-strain plot [86]. In a cellular structure, the local yielding at 0.2% strain is also magnified in a global sense. If one assumes a magnification factor of about 12, the corresponding global residual strain becomes 2.4%. Thus from Figure 3.10, the non-contact structures can be stretched up to about 9.1%, while the contact-aided structures can be stretched up to about 9.7%. The analytical model predicts a global strain of 8.4% for non-contact structures and 11.7% for contact-aided structures. The stress relief observed in the experiments is about 6.6%, while that predicted by the model is about 39.3%. The error between the experimentally observed strain and the predicted strain can be attributed to the fact that the analytical model assumes a structure with an infinite number of cells (so that the boundary effects are negligible), but the experimental model has only a few cells (and boundary effects are not negligible). Errors in the measurement of geometrical parameters and the material properties may also contribute.

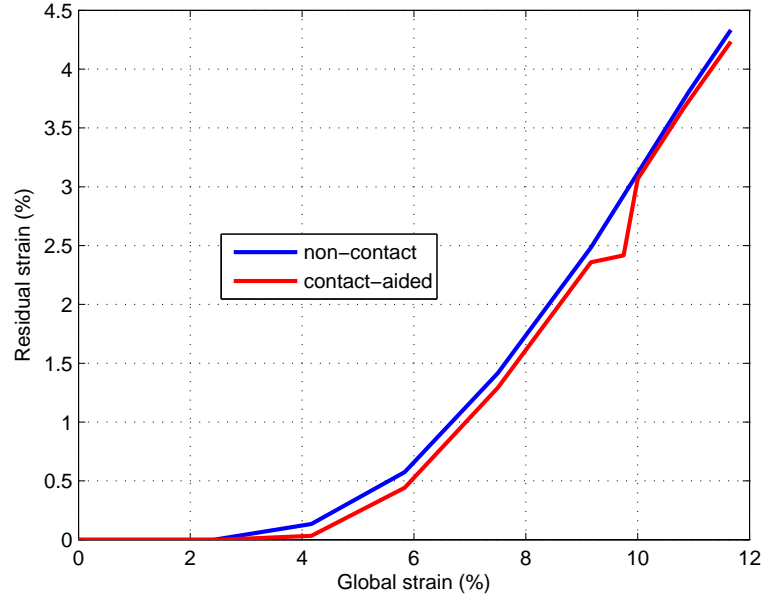


**Figure 3.10.** Variation of residual strain with global strain. The kink in the contact-aided plot occurs when contact takes place

The second set of experiments, involving samples B, were carried out to validate the simulation. In this set, both structures were stretched sufficiently and their load-displacement data was recorded. A variation of non-dimensional load (required to stretch the structure) against a non-dimensional extension (global strain per unit material strain) is shown in Figure 3.11. For this plot, the structure was modeled as a finite sheet in FE simulation to emulate the boundary effects and the experimental setup. Five cells were modeled and no boundary condition is applied to top-most and bottom-most cell walls. Instead, these walls were modeled twice as thick as manufactured in the experimental models. Rest of the boundary conditions and loading are same as described in the earlier section. Therefore, the experimental and FE load-displacement characteristics match very closely. The current analytical model does not address the boundary effects, and thus a significant difference is observed.



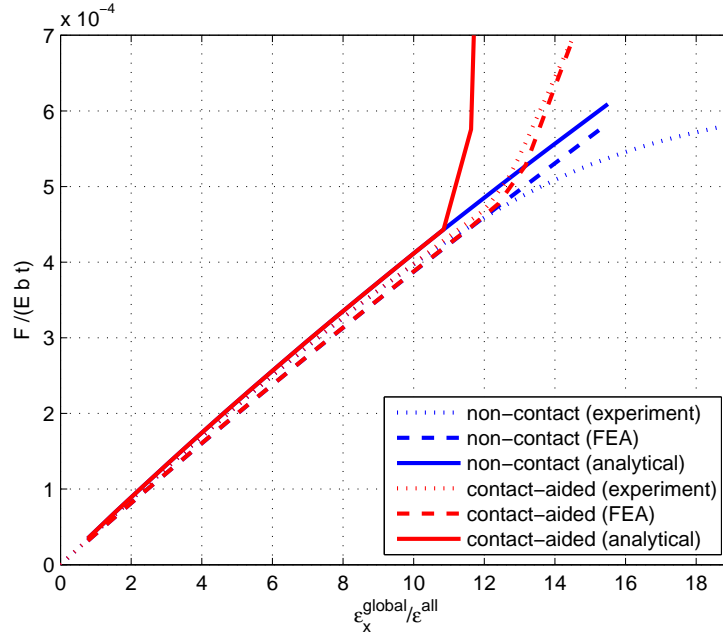


**Figure 3.11.** Variation of non-dimensional reaction load vs. non-dimensional extension

### 3.6 Extension of the Analytical Model

The analytical model developed in the preceding section assumes a stress state in only the oblique wall and at the end of deformation process. Some observations are as follows:

1. The underlying assumption for the model is that the maximum stress occurs when the deformation is also the maximum. This assumption might not be accurate in every case. For example, the stress history is plotted for  $h/l=2.0$ ,  $t/l=0.05$ , and  $\theta=-30$  deg. with Delrin as a material using the analytical model and FEA and is shown in Figure 3.12(a). The analytical model predicts the maximum global strain to be about 16.5%. The plot indicates that the maximum stress reaches the allowable limit at about 13% and peaks at about 15%. Evidently, a modification is necessary to address this issue to ensure that the tensile stress is always less than the allowable value along the entire deformation process.

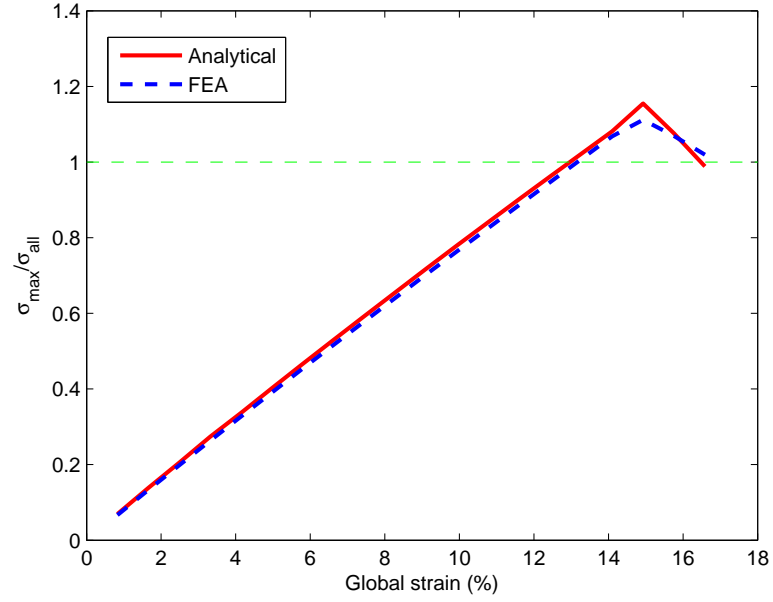
2. The present model ignores the stresses in the other walls of the cellular structure such as the contact mechanism and the horizontal wall. A modification is needed to accommodate the maximum stresses in these walls.
3. Figure 3.12(b) shows stress history plots for two geometries using Delrin as a material. For case I, the contact takes place well before the allowable stress. This effectively decreases the the rate of change of maximum stress with deformation. For case II, the contact occurs when the stress is near to the allowable value. The slope of stress-displacement curve changes its sign and the maximum stress initially decreases with the deformation before increasing again. Although both these cases lead to stress relief and a reduction in the maximum stress, the model cannot predict if a cell geometry leads to a particular case.

Notably, Eqns. 3.22 and 3.26 are valid irrespective of these limitations. Newer constraints are formulated corresponding to these observations. Evidently from Figure 3.12(a), the maximum stress crosses the allowable stress before contact (about 13% global strain) implying that the initial contact gap was significantly higher. If contact is forced to take place when the maximum stress is near the allowable value, it results in stress relief and higher deformations are possible without a local failure. Moreover, in such a case, the slope of stress strain curve must change its sign to accomplish stress relief. All such cases, therefore, yield the stress history plot represented by case II in Figure 3.12(b).

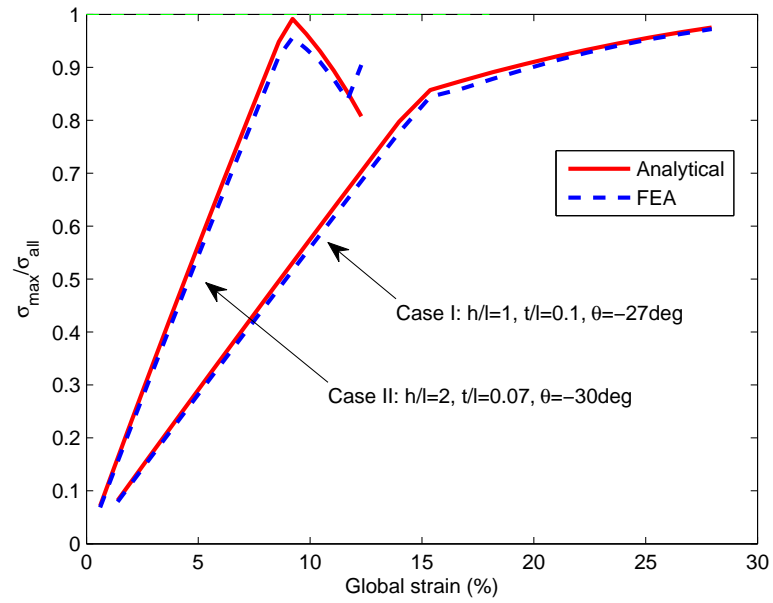
To implement such a scheme, the initial contact gap must be such that contact occurs when the maximum stress is near the allowable value. The initial contact gap is therefore limited to the total y-displacement for the non-contact structures. The total y-displacement for the non-contact structures ( $\gamma_{NC}$ ) can be calculated by using the axial stress for non-contact structures (using Eqn. 3.27) in the equation for contact gap (Eqn. 3.26). Mathematically,

$$\gamma_{\max} = \gamma_{NC} \quad (3.31)$$

Although such a contact gap keeps the maximum tensile stress below the allowable value, the axial stress increases with increasing stretching. Since the maximum axial stress can only be as high as the buckling stress, Eqn. 3.26 is used again



(a) Example of maximum stress not occurring at the end of deformation process



(b) Various stress-displacement relations for stress relief

**Figure 3.12.** Stress history plots for various test cases using both analytical model and FEA

with  $\sigma_{ax} = \sigma_{ax}^{buck}$  and  $\gamma = \gamma_{\max}$  to solve for  $\sigma_{\max}$ . This maximum stress along with buckling stress is used in Eqn. 3.22 to estimate the maximum global strain.

Eqs. 3.20 and 3.25 provide the total axial stretching in the horizontal walls ( $\delta_x^s$ ) and the contact mechanism ( $\delta_y^s$ ), respectively. The lengths of these members are  $h$  and  $2l \cos(\theta + \phi)$ , respectively. The stretching displacement divided by the length gives the axial strain. The axial strain must be less than the material allowable strain to prevent local failure. If  $\epsilon_h$  and  $\epsilon_{CM}$  are the stretching strain in the horizontal wall and that in the contact mechanism, respectively,

$$\begin{aligned} \epsilon_h &= \frac{\delta_x^s}{h} \leq \frac{\sigma_{all}}{E} \\ \epsilon_{CM} &= \frac{\delta_y^s}{2l \cos(\theta + \phi)} \leq \frac{\sigma_{all}}{E} \end{aligned} \quad (3.32)$$

If the preceding constraints are violated, then the axial stress ( $\sigma_{ax}$ ) is adjusted to lower the strains and maximum global strain is recalculated.

## 3.7 Size Optimization

The modified analytical model developed in the preceding section is employed in a formal optimization scheme to determine the optimum (non-dimensional) cell size.

### 3.7.1 Problem Formulation

Two independent optimization problems are considered. In one optimization problem, maximization of the amplification factor ( $\epsilon_{x,\max}^{\text{global}}/(\sigma_{all}/E)$ ) is sought. In another optimization problem, a measure of stress relief is maximized. Tables 3.2 and 3.3 indicate that the cellular geometries for higher global strains require smaller initial contact gaps. However, very small contact gaps are difficult to manufacture. Therefore, another objective function in the form of the initial contact gap is added in each of the preceding problems. Mathematically,

$$\begin{aligned} &\max \quad \left\{ \begin{array}{c} M^{CA} \\ \gamma/l \end{array} \right\} \\ &\text{Subject to} \\ &0.5 \leq \quad h/l \quad \leq 2.0 \end{aligned} \quad (3.33)$$

$$\begin{array}{rcl} 0.05 \leq & t/l & \leq 0.10 \\ \max \left( \frac{\pi}{6}, \arcsin \frac{h}{2l} \right) \leq & \theta & \leq 0 \end{array}$$

and

$$\begin{array}{rcl} \max & \left\{ \begin{array}{l} m' = \frac{M^{CA} - M^{NC}}{M^{NC}} \\ \gamma/l \end{array} \right\} & \\ \text{Subject to} & & \\ 0.5 \leq & h/l & \leq 2.0 \\ 0.05 \leq & t/l & \leq 0.10 \\ \max \left( \frac{\pi}{6}, \arcsin \frac{h}{2l} \right) \leq & \theta & \leq 0 \end{array} \quad (3.34)$$

where  $M^{CA}$  and  $M^{NC}$  are the amplification or magnification factors for the contact-aided cellular mechanism and the non-contact cellular structure for the same geometrical parameters, respectively.  $m'$  is a measure of stress relief and given by the normalized increase in the amplification factor. The design variables are non-dimensional geometric parameters  $h/l$ ,  $t/l$ , and  $\theta$ . Eqns. 3.33 and 3.34 form multi-objective optimization problems. To tackle these optimization problems, an evolutionary algorithm based optimizer is implemented.

The Non-dominated Sorting Genetic Algorithm (NSGA-II) is one of the computationally fast evolutionary algorithms that is used for multi-objective optimization [87]. In addition to reducing the computational complexity, the algorithm also uses non-dominated sorting approach for finding the Pareto front. A population member is said to be dominated by another if all the latter is better in all the objective functions. The non-dominated sorting approach involves sorting the population members according to the non-domination. Moreover, both the parent and offspring population are combined to obtain the best members.

### 3.7.2 Results

The optimization parameters for crossover probability (0.5), mutation probability (0.5), crossover distribution index (20), and mutation distribution index (20) were set at the default values recommended by the developers of NSGA-II. The pop-

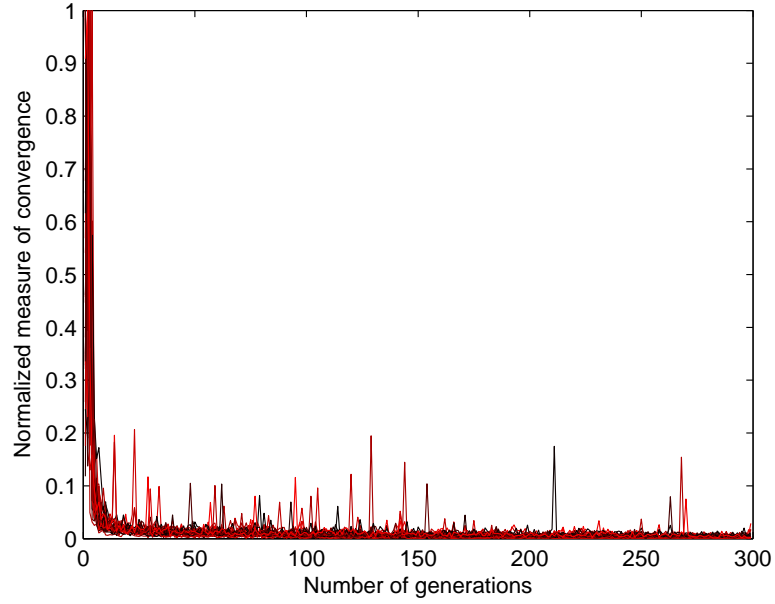


**Figure 3.13.** Normalized measure of convergence as a function of the number of generations

ulation size was 40, and the number of generations was set to 200. These values were determined empirically such that the resulting Pareto curve is smooth, and no more improvement is observed in the front. A normalized measure of the convergence is plotted against the number of generations in Figure 3.13. The convergence measure was adapted from [88], and it is plotted for 25 different random initial seeds and a population of 40. The figure shows that after about 200 generations, the measure is less than 0.01 for all random seeds. The figure also demonstrates that the effect of the initial guess on convergence is minimal. The Pareto curves were found for various values of  $\sigma_{\text{all}}/E$  for both the optimization problems and are shown in Figures 3.14 and 3.15.

The non-dimensional geometric parameters, the amplification ratios, and the stress relief for the end points of each Pareto curve (shown as square boxes in Figures 3.14 and 3.15) are calculated and summarized in Table 3.6.

The following observations can be made from this optimization study:

1. Both the magnification factor and the normalized stress relief increase with decreasing values of initial contact gap. This clearly demonstrates the trade-

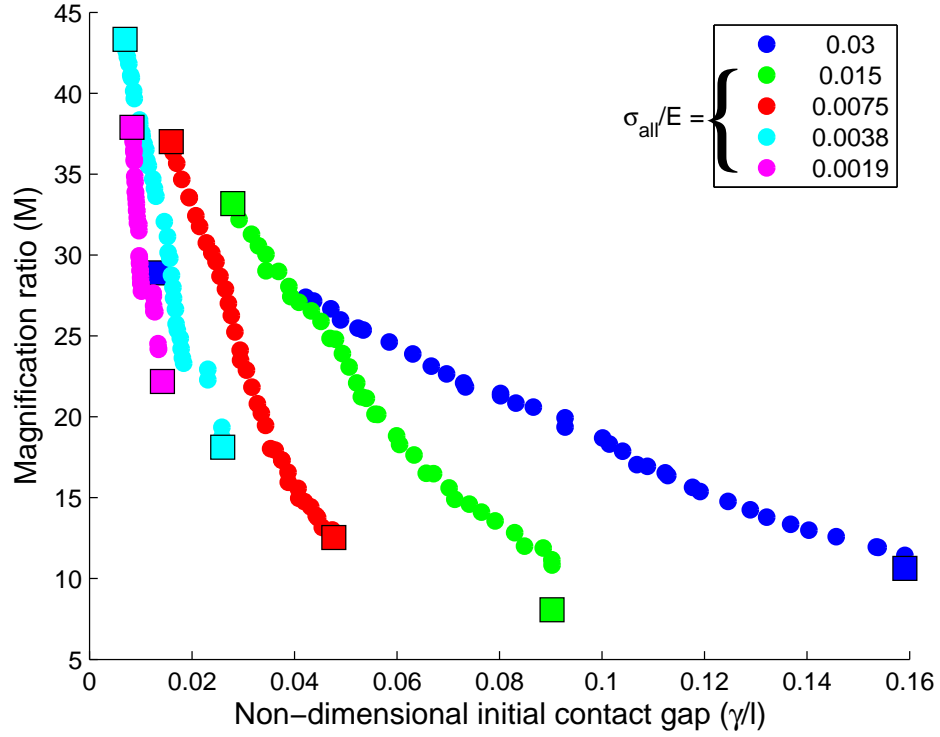


**Figure 3.14.** Pareto curves for various values of  $\sigma_{\text{all}}/E$  for optimization problem given in Eqn. 3.33. The square boxes indicates the end points for each Pareto curve

off between the output performance and the manufacturing capabilities. A manufacturing process that can make smaller contact gaps is very useful at obtaining a higher strain contact-aided cellular mechanism.

2. The benefits of cellular configuration and contact mechanisms increase with decreasing core allowable strain. Materials such as ceramics and alloys exhibit a low allowable strain. Contact-aided cellular mechanisms can help to increase their overall strain.
3. The maximum performance was found when cell angle is at its lowest possible value in all cases. This is consistent with that of non-contact cellular structures [7].
4. The designs from the greyed rows in Table 3.6 correspond to the stress relief indicated by case I in Figure 3.12(b). All other designs correspond to case

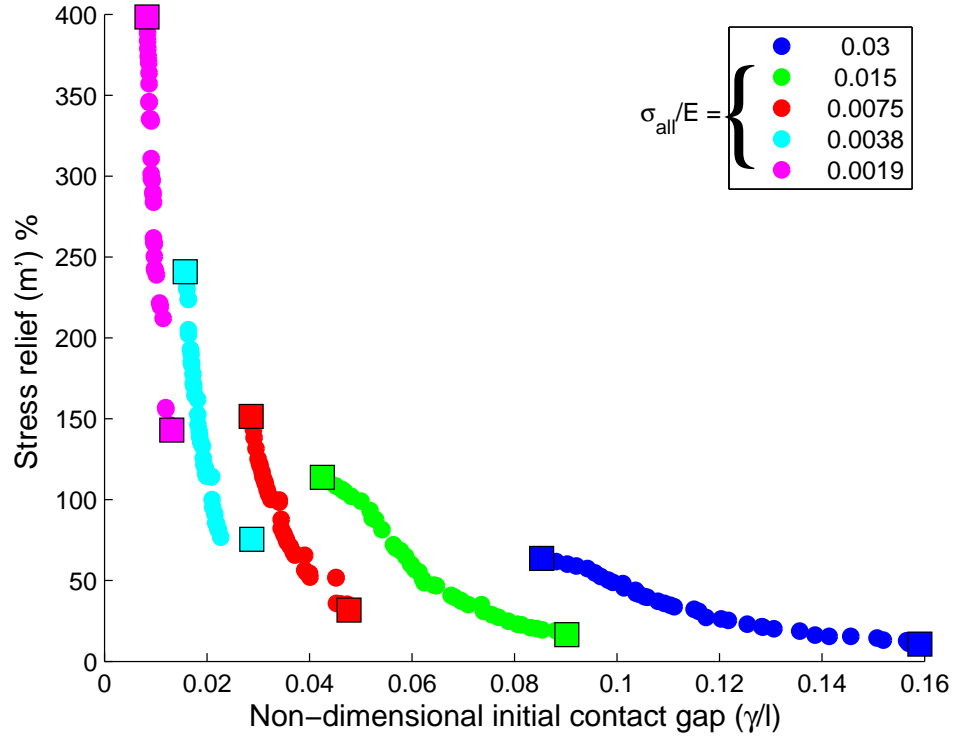


**Figure 3.15.** Pareto curves for various values of  $\sigma_{\text{all}}/E$  for optimization problem given in Eqn. 3.34. The square boxes indicates the end points for each Pareto curve

II. Apparently, the designs corresponding to case I have larger contact gaps, while those corresponding to case II have larger magnification ratios and stress reliefs. This is expected since contact gaps for the designs from case I are not constrained by the non-contact Y-deformations. In case II, the slope of effective stress-strain curve changes its sign, which makes the designs from case II have larger magnification ratios and stress reliefs.

5. Maximum amplification is obtained for slender cells with thin walls, since slender walls make the cellular mechanism very compliant. However, the initial contact gaps need to be very small for such cells.
6. The stress relief is maximum for stout cells having higher  $h/l$  ratios. For such cells, since the magnification ratio for non-contact cells is small, the benefit obtained using contact is also higher. For larger contact gaps, though, the



**Table 3.6.** Geometry and different objective functions for the end points of each Pareto curve

$\sigma_{\text{all}}/E$	$h/l$	$t/l$	$\theta(\text{deg.})$	$\gamma/l$	$m'$	$M^{CA}$	$M^{NC}$
For optimization problem given by Eqn. 3.33							
0.0300	1.15	0.05	-30	0.16	10.3	10.6	9.6
	0.50	0.05	-12	0.01	28.7	28.9	22.4
0.0150	1.37	0.05	-30	0.09	15.5	8.1	7.0
	0.50	0.05	-13	0.03	37.7	33.2	24.1
0.0075	1.10	0.05	-30	0.05	27.1	12.5	9.9
	0.50	0.05	-13	0.02	55.0	37.1	23.9
0.0038	1.03	0.05	-27	0.03	74.1	18.1	10.4
	0.50	0.05	-13	0.007	88.3	43.3	23.8
0.0019	1.07	0.05	-27	0.026	74.1	18.1	10.4
	0.77	0.05	-21	0.014	120.3	22.2	10.1
For optimization problem given by Eqn. 3.34							
0.0300	2.00	0.05	-30	0.16	10.7	4.6	4.2
	2.00	0.10	-30	0.09	63.7	3.4	2.1
0.0150	2.00	0.05	-30	0.09	16.5	4.7	4.0
	2.00	0.10	-30	0.04	113.7	4.3	2.0
0.0075	1.90	0.05	-30	0.05	31.7	5.5	4.2
	2.00	0.08	-30	0.03	151.3	5.9	2.3
0.0038	1.90	0.05	-30	0.03	75.5	7.5	4.3
	2.00	0.08	-30	0.02	240.9	8.6	2.5
0.0019	2.00	0.05	-27	0.01	143.0	9.5	3.9
	2.00	0.08	-30	0.008	398.4	13.0	2.6

wall thickness needs to be smaller – increasing the aspect ratio. Thinner walls make the cellular structure more compliant allowing more overall strain and marginally larger contact gaps.

### 3.8 Summary

Contact in cellular structures reduces the maximum tensile stress. This reduction in stress is utilized to increase the overall stretching capacity of the cellular structures. Analytical, numerical, and experimental work verifies this concept. Size optimization provides insights about these structure for implementing them for

applications such as morphing skin and meso-scaled components, as described in the next two chapters.

# Morphing Aircraft Skin

## 4.1 Introduction

One important potential application of high-strain materials is in morphing aircraft wings with large planform area changes. In this chapter, the proposed cellular structure is designed for use in a contemplated morphing aircraft skin, and its performance in terms of structural mass is compared with that of a non-contact cellular skin. Both the in-plane and out-of-plane stiffnesses are investigated for actuation and load-bearing capacity.

## 4.2 Description

Consider a variable span morphing wing with rectangular profile as shown in Figure 4.1. The initial half-span of the wing is  $b$  and the root chord is  $c$ . During morphing, the wing expands span-wise as shown in dashed lines. The difference between the final span and initial span divided by the initial span gives the morphing or global strain ( $\epsilon_x^{global}$ ). The underlying mechanism that drives the shape change is shown as a diamond cell-type [26, 30, 89], but it could be any general topology. The underlying morphing mechanism provides an input displacement constraint to the cellular skin. The points at which the underlying mechanism is connected to the skin are distributed uniformly over the wing. The number of such connections in the span direction is denoted by  $(n + 1)$ , and in the chord direction, by  $(m +$

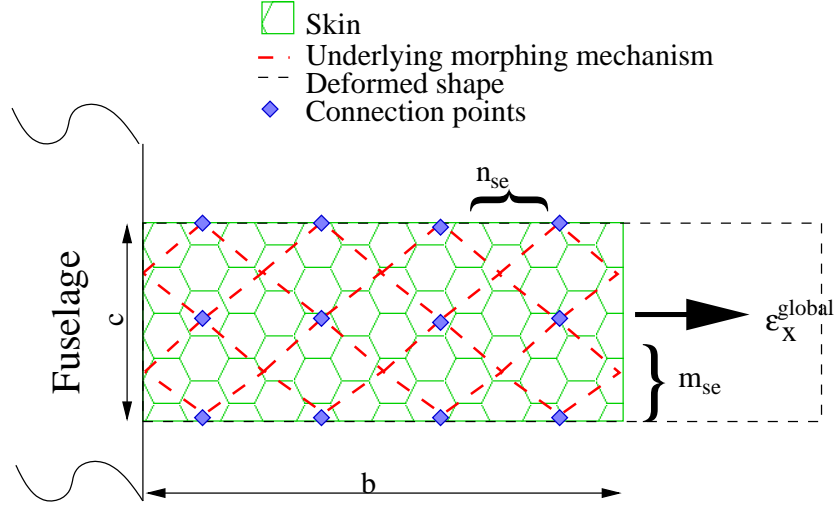


**Figure 4.1.** A variable span morphing wing with notation

1). A skin element is defined as the portion of the skin between two consecutive attachment points in each direction. Therefore, there are  $(n \times m)$  skin elements. If the number of cells per unit skin element in the span direction is  $n_{se}$  and in the chord direction is  $m_{se}$ , the the total number of unit cells comprising the half-span is as the following.

$$nn_{se}m_{se}(m+1) + (nn_{se}-1)[m_{se}(m+1)-1] \quad (4.1)$$

The ‘cell density’ is defined as the number of cell per unit area of the skin. Therefore, the cell density ( $\rho_{cell}$ ) is given by

$$\rho_{cell} = \frac{nn_{se}m_{se}(m+1) + (nn_{se}-1)[m_{se}(m+1)-1]}{bc} \quad (4.2)$$

Figure 4.2 illustrates some aspects of this morphing skin problem and the corresponding nomenclature. Both out-of-plane and in-plane aerodynamic loads are applied to the wing (not shown in the figure). The distribution of these loads is assumed to be uniform over the planform of the wing. Using this notation, the average half-length ( $b'$ ) and average half-width ( $c'$ ) of a cell are defined as:

$$b' = \frac{b}{2nn_{se}} \quad (4.3)$$

$$c' = \frac{c}{2mm_{se}} \quad (4.4)$$

The length and width of a unit cell are  $2(h + l \cdot \sin \theta)$  and  $2l \cdot \cos \theta$ , respectively. Using the nomenclature for number of connectors and number of cells per unit skin-element, the total length and total width covered by all skin cells is equal to  $2nn_{se} \cdot (h + l \cdot \sin \theta)$  and  $2mm_{se}l \cdot \cos \theta$  respectively. These values must be equal to the span and chord of the wing. Simplifying using Eqs. 4.3 and 4.4, the geometric parameters of a cell can be expressed as a function of cell angle as,

$$h = b' - c' \tan(\theta) \quad (4.5)$$

$$l = c' \sec(\theta) \quad (4.6)$$

Eqs. 4.5 and 4.6 show that, given  $n, m, n_{se}$  and  $m_{se}$ , the angle ( $\theta$ ) is the only independent cell parameter. To determine the limiting values of the angle, two extreme cases are considered. In the first case, the length  $h$  approaches zero and in the other cases, all the cell walls of length  $l$  will touch each other internally [18]. The corresponding limiting values of angle are

$$\theta_{\min} = \arctan(-b'/c') = \arctan(-r) \quad (4.7)$$

$$\theta_{\max} = \arctan(b'/c') = \arctan(r) \quad (4.8)$$

where

$$r = b'/c' \quad (4.9)$$

$r$  can be viewed as the aspect ratio of a cell.

### 4.2.1 Development of Constraints

The effective moduli of elasticity of a cellular structure in the span-wise direction ( $E_{span}$ ) and in the chord-wise direction ( $E_{chord}$ ) are adapted from Gibson and Ashby [4]

$$E_{chord} = \frac{E_s (t/l)^3 \cos \theta}{(h/l + \sin \theta) \sin^2 \theta} \quad (4.10)$$

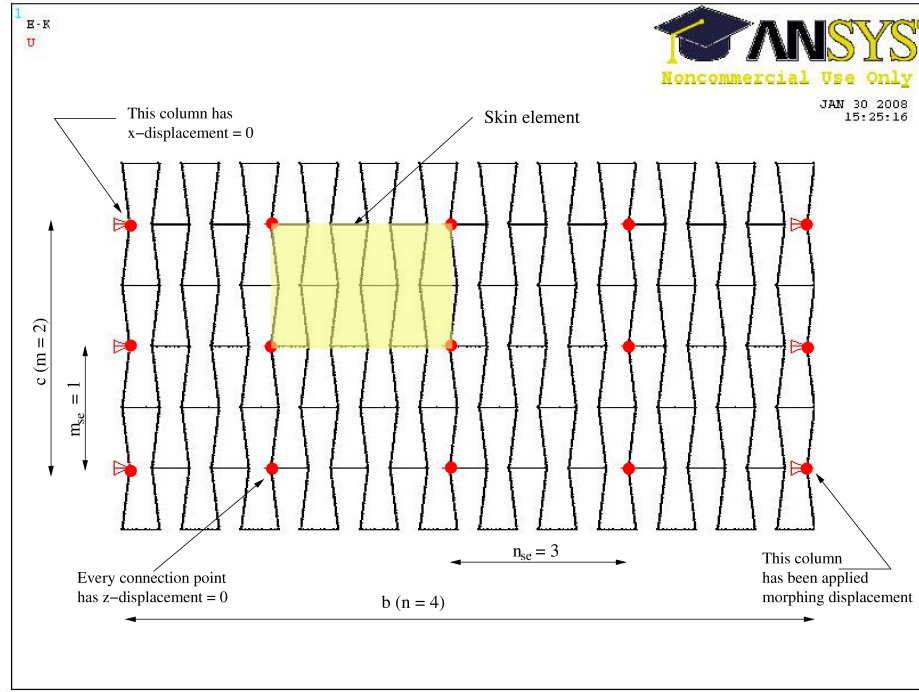


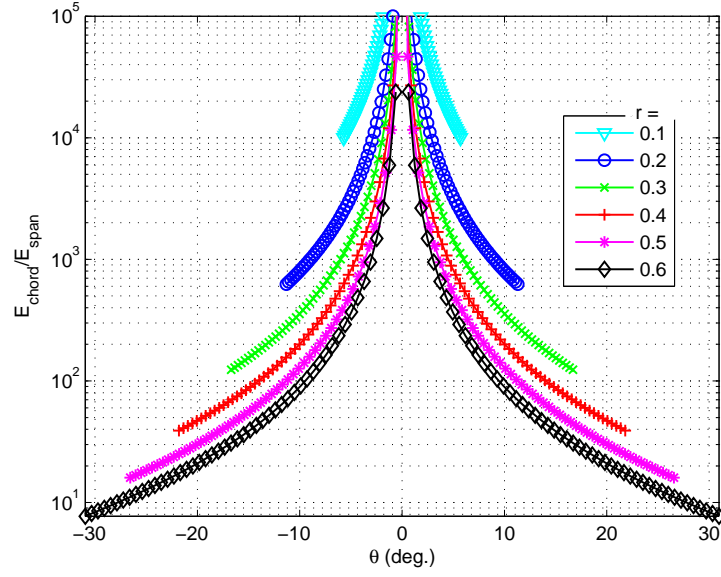
**Figure 4.2.** Example of nomenclature used for skin element and other integer variables

$$E_{span} = \frac{E_s (t/l)^3 (h/l + \sin \theta)}{\cos^3 \theta} \quad (4.11)$$

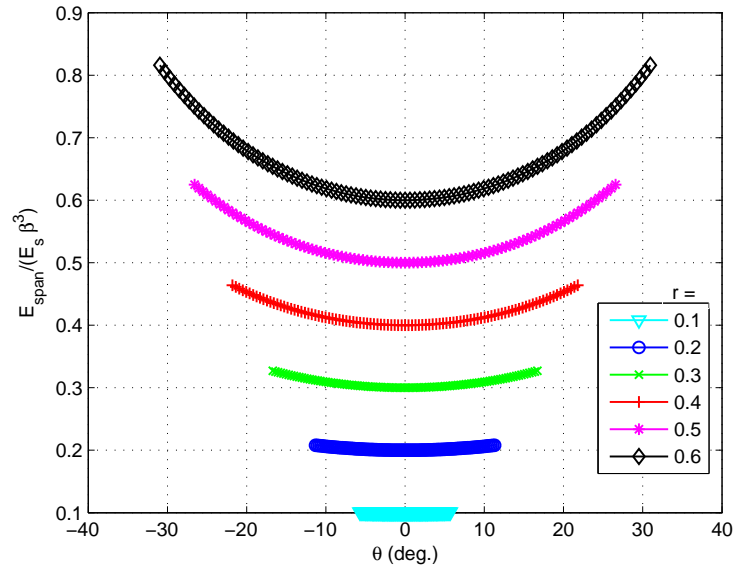
where  $E_s$  is the modulus of elasticity of the base material. The ratio ( $E_{chord}/E_{span}$ ) is simplified as,

$$\frac{E_{chord}}{E_{span}} = \frac{1}{(r \tan \theta)^2} \quad (4.12)$$

where  $r$  is given by Eq. 4.9. This ratio is plotted for various values of  $r$  and the corresponding feasible range of  $\theta$  and is shown in Figure 4.3a. The figure indicates that for values of  $r < 0.3$ , the ratio of the moduli is greater than approximately 150. This means that for  $r < 0.3$ , the structure is much stiffer in a direction perpendicular to the morphing strain, which is a requirement for the morphing skin. On the other hand, the variation of a normalized measure of  $E_{span}$  is shown in Figure 4.3b. The structure becomes significantly stiffer in both directions for higher values of  $r$ . To resolve conflicts on  $r$ , the design value of  $r$  is taken as approximately 0.3.



(a) Variation of  $E_{chord}/E_{span}$  with  $r$  and  $\theta$



(b) Variation of dimensionless  $E_{span}$  with  $r$  and  $\theta$

**Figure 4.3.** Demonstration of constraint  $r \sim 0.3$

According to a 1934 NACA report [90], to avoid any unnecessary aerodynamic drag, the maximum out-of-plane perturbation ( $\delta$ ) should be less than about 0.001 of the root chord. This is also referred to as the pillowing [43] or bubbling constraint [91].

If the number of cells per unit skin-element ( $m_{se}$ ) is increased, then the structural mass increases but the maximum stress and the out-of-plane deformation do not vary much. Therefore, its value is kept at its lower bound (i.e.,  $m_{se} = 1$ ). As  $r \sim 0.3$ , substituting  $m_{se} = 1$  in Eqn. 4.9 and simplifying,

$$m = 0.3 \cdot \frac{nn_{se}}{(b/c)} \quad (4.13)$$

Constraints developed here are for honeycomb-like structures and assume a linearly elastic material. The contact-aided cellular structures behave exactly the same way until contact takes place.

### 4.2.2 Optimization Problem

As in many other aerospace structural problems, the total mass of the morphing skin is a concern. Therefore one objective is to minimize the mass of the system,  $m_t$ . The constraints developed in this section are used to formulate the following optimization problem

$$\begin{aligned} & \min \quad m_t \\ & \text{subject to,} \\ & \epsilon_x^{global} - \epsilon_{x, d} = 0 \\ & \sigma_{\max} - \sigma_{all} < 0 \\ & \delta/c - 0.001 < 0 \\ & r - 0.3 \sim 0 \\ & m_{se} - 1 = 0 \\ & \theta_{\min} \leq \theta \leq \theta_{\max} \end{aligned} \quad (4.14)$$



where  $\sigma_{\max}$  is the maximum stress in the structure,  $\sigma_{all}$  is the allowable stress for the material being used, and  $\epsilon_{x,d}$  is the desired morphing strain.  $\theta_{\min}$  and  $\theta_{\max}$  are given using Eqs. 4.7 and 4.8, respectively. The design variables are  $n$ ,  $n_{se}$ ,  $w$ ,  $\theta$ ,  $\gamma$ .

### 4.2.3 Solution Algorithm

The entire half-span of the skin is modeled in ANSYS with BEAM188 elements for FEA analysis. This 3-D element is based on nonlinear Timoshenko beam theory that allows large deflection, shear effects, slender to thick cross-sections, plasticity and contact elements [92]. CONTA172 along with TARGE169 are used to model the contact. For a nonlinear elastic material such as Delrin, the Multi-linear ISotropic hardening (MISO) model is used. The aerodynamic loads are uniformly applied. The lift loads (= weight of the aircraft  $\times$  the load factor) are applied in the out-of-plane direction. The drag loads ( $\sim 1/10$  of lift loads) are applied parallel to the chord. At all the connection points, the out-of-plane displacement is zero. For the left-most connection points, the span-wise displacement; and for the bottom-most points, the chord-wise displacement is zero. The morphing displacement is applied at the right-most connection points (see Figure 4.2). Full transient analysis with large deflections is implemented to solve the problem.

Except for  $\theta$  and  $\gamma$ , no other design variables have explicit bounds. Two design variables, namely  $n$  and  $n_{se}$ , are integers. The problem is difficult to solve using classical optimization methods and, because of the high computational cost associated with these approaches, an ad-hoc method is applied to tackle it. The basic steps in this algorithm are outlined in the following.

1. For a given value of  $\epsilon_{x,d}$ , a pair  $(n, n_{se})$  is considered. Initially  $\theta$  is taken to be 0 ( $= (\theta_{\max} + \theta_{\min})/2$ ) and aerodynamic loads are applied. Eq. 4.13 is used to calculate  $m$ . The FEA simulation for the entire morphing operation is performed. Two distinct values of out-of-plane thickness ( $w$ ) are found such that the lower value violates the pillowing constraint and the higher value satisfies the constraint. Keeping all other variables fixed, the bisection method is applied to find the value of  $w$  at which  $\delta/c$  is very close to 0.001. This is the minimum thickness of the structure required for the given loading,

and it is held constant for the rest of the process. The maximum stress constraint is not considered in this step.

2. Now  $\theta$  is optimized such that the maximum stress in the structure is a minimum. MATLAB's nonlinear optimizer **fminbnd** is used for this purpose. The optimized cell angle can be different than zero. Evidently, from Figure 4.3(b), the effective modulus in span-wise direction ( $E_{span}$ ) higher for all cell angles  $\theta \neq 0$  than that for  $\theta = 0$ . The calculation of thickness is not needed again, since the thickness was estimated based on zero cell angle or the minimum effective modulus.
3. For a non-contact cellular structure, if  $\sigma_{\max} > \sigma_{all}$  even after the optimization on  $\theta$ , then the design is infeasible. For a contact-aided cellular structure, though, there are two possibilities:
  - (a)  $\sigma_{\max} > \sigma_{all}$ : The contact opening ( $\gamma$ ) is then reduced such that contact takes place during the morphing deformation. As described in Chapter 3, this leads to stress relief. In some cases it can make the design feasible. Using Eqn. 3.28, the geometrically maximum global strain for auxetic configuration is  $-\frac{\sin \theta}{h/l + \sin \theta}$ . Substituting  $h$  and  $l$  from Eqns. 4.5 and 4.6, respectively, and simplifying,  $\theta_{\max}$  becomes  $\arctan(-\epsilon_x^{global} \cdot b'/c')$ . This maximum cell angle is used in Step 2.
  - (b)  $\sigma_{\max} < \sigma_{all}$ : In this case, contact is not needed for stress relief due to the morphing displacement, but one can still use the contact mechanism to decrease the out-of-plane deformation. The thickness ( $w$ ) is recalculated for a particular value of  $\gamma$  using Step 1. This process is repeated until compressive stresses in the contact mechanism are below the buckling limit. This results in a lower total mass of the structure. Here the cells must have a regular configuration anytime during the morphing. For Step 2,  $\theta_{\min}$  becomes 0.
4. All the preceding steps are repeated for a number of combinations of  $(n, n_{se})$ , and the resultant mass for each feasible solution is recorded. The best design is the one with the lowest mass.

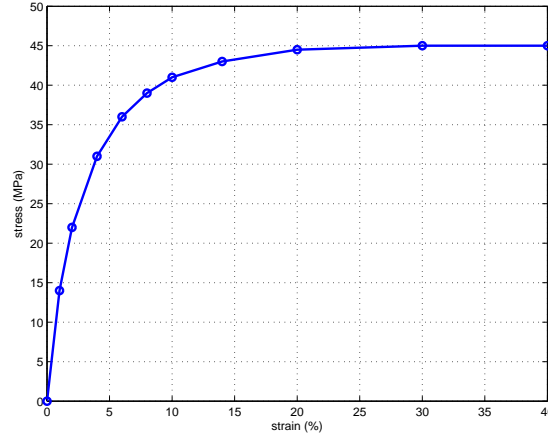


**Figure 4.4.** Stress-strain characteristics for Delrin 100st

### 4.3 Results

The described algorithm is applied to non-contact cellular structures as well as the contact-aided cellular structures for an RC-scale aircraft. Two material models are considered, and the results for the contact-aided skin structure are found to be advantageous.

To validate the feasibility of the algorithm and the proposed cellular structure, a 1 lb. RC aircraft is considered. The unmorphed half-span and chord of the wing for the aircraft are approximately 44 cm and 25 cm, respectively. The load factor ( $LF$ ) is considered to be  $\pm 3$  and the factor of safety (FOS) is taken to be 1.2. The results for a target of 75% global strain are presented. Commercially available engineering thermoplastic Delrin 100st is considered as a candidate skin material because of its high toughness and high value of yield strain. The stress-strain relationship for Delrin is found in the literature [7, 93] and is shown in Figure 4.4. According to the same references, the yield strain of Delrin has been reported as 30 %, which corresponds to yield stress of 43 MPa; with FOS,  $\sigma_{all} = 35.8$  MPa. The density of the material is  $1340 \text{ kg/m}^3$ .

Results based on nonlinear material characteristics and for various pairs of  $(n, n_{se})$  for non-contact cellular structure are found. The results are listed in Table 4.1. Clearly each design is feasible in this case. The total mass, though, decreases as

the cell density increases. Evidently the best design corresponds to  $(n, n_{se})=(9,5)$  having a total mass of 185 g.

**Table 4.1.** Design of morphing skin for non-contact cellular structure using non-linear elastic material model

$(n, n_{se})$	$\rho_{cell}$	$w$	$\theta$	$\sigma_{\max}$	$m_t$
		mm	deg	MPa	g
(7,3)	1682	23.9	0	18.0	497
(7,4)	2755	19.1	0	19.5	503
(7,5)	4082	16.4	0	21.3	520
(8,3)	1927	18.8	0	15.9	439
(8,4)	3155	13.3	0	17.7	397
(8,5)	5391	8.2	0	23.3	290
(9,3)	2655	8.5	0	20.1	217
(9,4)	4200	6.8	0	20.9	220
(9,5)	6882	4.7	0	24.9	185

Results for contact-aided cellular structures are presented in Table 4.2. Since the maximum stress does not exceed the allowable value, stress relief is not needed here. The contact mechanism itself, provides additional load bearing members for the aerodynamic loads. Moreover, in the case of regular cells (see Figure 3.1) the net axial stress in the contact mechanism is compressive and the net axial stress in the oblique cell walls is tensile. This stiffens the structure in the transverse direction, and therefore, the corresponding deformation decreases. The best design corresponds to (9,5) in the regular configuration ( $\theta > 0$ ) with a minimum mass of 142 g. While utilizing contact and the transverse stiffening, a smaller thickness suffices, resulting in a reduction of structural mass. As shown in the table, there is a significant reduction in the total mass, which is lower than that of the corresponding non-contact cellular structure. A chart comparing the total mass of the system for different combinations of connection points is given in Figure 4.5. For lower cell density, using contact is not efficient, but at higher cell density, it becomes very advantageous. Figure 4.6 shows the reduction in the required out-

**Table 4.2.** Design of morphing skin for contact-aided cellular structure based on non-linear elastic material model

$(n, n_{se})$	$\rho_{cell}$	$w$	$\theta$	$\sigma_{\max}$	$m_t$	$\gamma$
		mm	deg	MPa	g	mm
(7,3)	1682	13.5	0	21.0	549	1.03
(7,4)	2755	7.6	0	22.8	397	0.99
(7,5)	4082	5.0	0	24.5	319	0.95
(8,3)	1927	10.7	0	18.7	492	1.00
(8,4)	3155	5.7	0	20.5	334	0.99
(8,5)	5391	2.8	0	26.0	201	0.95
(9,3)	2655	4.5	0	23.4	228	1.00
(9,4)	4200	2.9	0	23.4	190	1.00
(9,5)	6882	1.8	0	29.9	142	0.99

of-plane thickness with cell density. Even though the thickness required for the contact-aided structure is less than that of corresponding non-contact structure, the contact mechanism adds to the structural mass. The required thickness decreases by more than 40% in each case but the maximum decrease in the total mass is about 39%. Further, the mass of the structure decreases as the cell density increases.

To investigate the effects of a linearly elastic material model, the properties of Delrin are linearized. The initial slope of the stress-strain relationship (see Figure 4.4) is assumed to be the Young's modulus of the linear material ( $= 1.4$  GPa). The yield stress is kept the same ( $\sigma_y = 43$  MPa). The strain at yield then becomes about 3%.

For this material model, results for non-contact cellular structures are given in Table 4.3. Only five design data points are now feasible with the best design corresponding to  $(n, n_{se}) = (9, 3)$  and a total mass of 245 g. The results for the contact-aided cellular skin are given in Table 4.4. To make more design points feasible, stress relief is necessary. Therefore, only an auxetic configuration (see Figure 3.1) is used. Seven design data points are feasible using stress relief. The

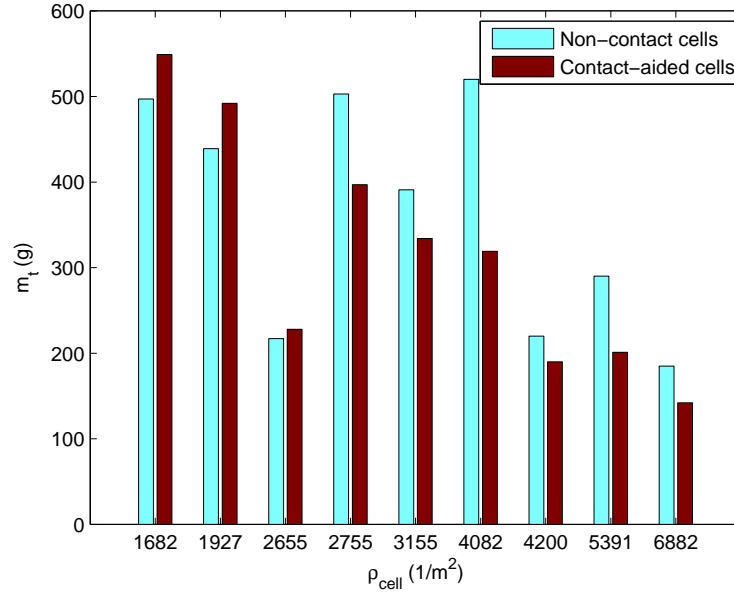
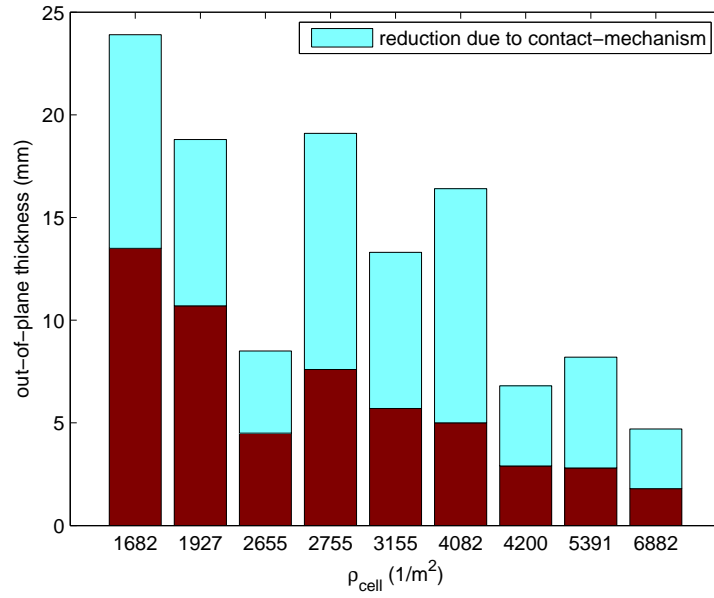


**Figure 4.5.** Bar chart showing the total mass for non-contact cells as well as for contact-aided cells

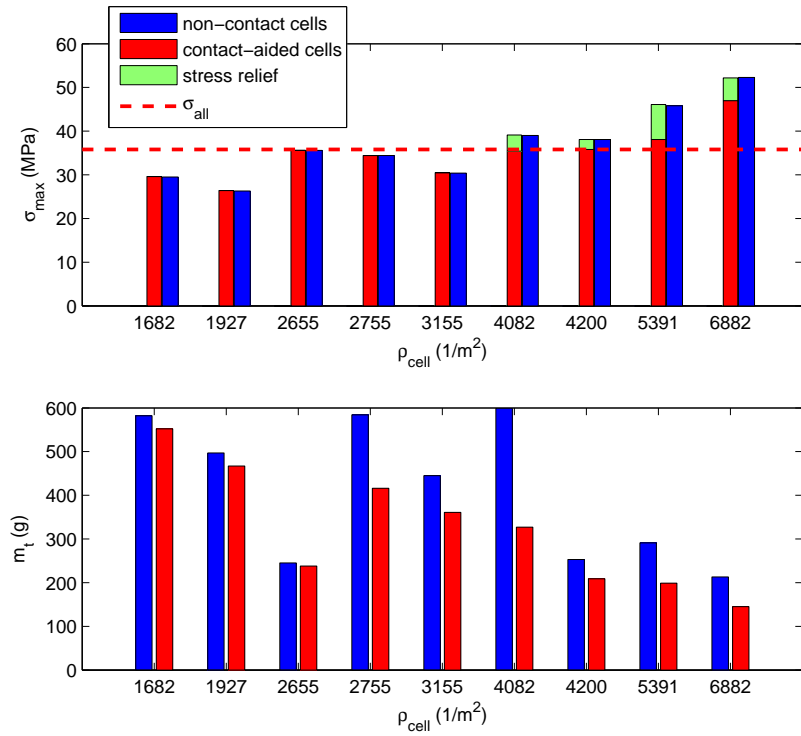
best design with  $(n, n_{se}) = (9, 4)$  has total mass of 209 g, which is 15% less than that of the best design for the non-contact case.

Figure 4.7 shows the variation of maximum stress and total structural mass for both the non-contact and contact-aided designs. The maximum stress increases and the structural mass decreases with cell density for both designs. The structural mass for any design is always lower for the contact-aided designs than that the corresponding non-contact design. For contact-aided structures, stress relief is utilized for some cases having higher cell density and the design is made feasible, without penalizing the mass. Also if stress relief is not used, the maximum stress in the two structures is approximately the same.

Two different material models, linear and nonlinear elastic, are considered for the design of a morphing skin. The unit cell geometry for both the non-contact and contact-aided cellular structure is found for each material model. The schematic representations of the final designs for all these cases are shown in Figure 4.8.



**Figure 4.6.** Reduction of required out-of-plane thickness while using contact



**Figure 4.7.** Maximum stress and structural mass with cell density

**Table 4.3.** Design of morphing skin for non-contact cellular structure using linearly elastic material model. Shaded rows indicate infeasible designs

$(n, n_{se})$	$\rho_{cell}$	$w$	$\theta$	$\sigma_{\max}$	$m_t$
		mm	deg	MPa	g
(7,3)	1682	23.9	-17	29.5	582
(7,4)	2755	19.1	-15	34.2	584
(7,5)	4082	16.4	-15	39.0	599
(8,3)	1927	18.5	-15	26.3	497
(8,4)	3155	13.2	-14	30.4	445
(8,5)	5391	8.2	-15	45.8	291
(9,3)	2655	8.2	-16	35.6	245
(9,4)	4200	6.8	-15	38.1	253
(9,5)	6882	4.7	-16	52.3	213

## 4.4 Stiffness Comparison

### 4.4.1 In-plane Stiffness

The results presented in the previous section indicate that the out-of-plane thickness for contact-aided structures is smaller than that of corresponding non-contact structures. This implies that the actuation forces required should also be lower. To verify this, a non-contact skin with  $(n, n_{se}) = (9, 3)$  (the best design for linearized model of Delrin in terms of total mass) and a contact-aided skin with  $(n, n_{se}) = (9, 4)$  (the best design for linearized model of Delrin in terms of total mass) are considered. Both the structures are analyzed in ANSYS using procedures described earlier. The in-plane stiffness is the sum of all reaction forces experienced by the skin where it is connected to the fuselage divided by the total morphing displacement (left-most nodes as shown in Figure 4.2). The stiffness of such in-plane structures is shown in Figure 4.9. The plot indicates that the stiffness of the contact-aided skin is 15% less than that of non-contact structure for the same morphing displacement. Therefore the stress relief not only helps



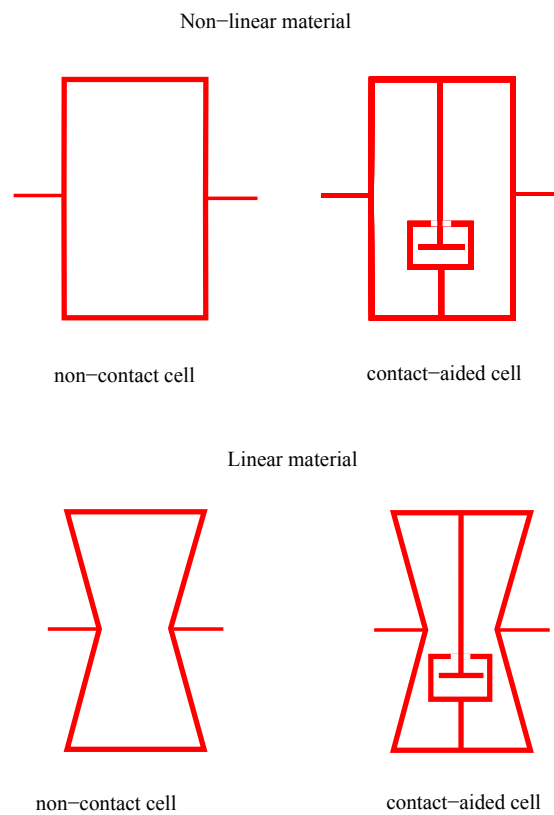


**Figure 4.8.** Schematic representation of the optimized cell shapes for morphing skin

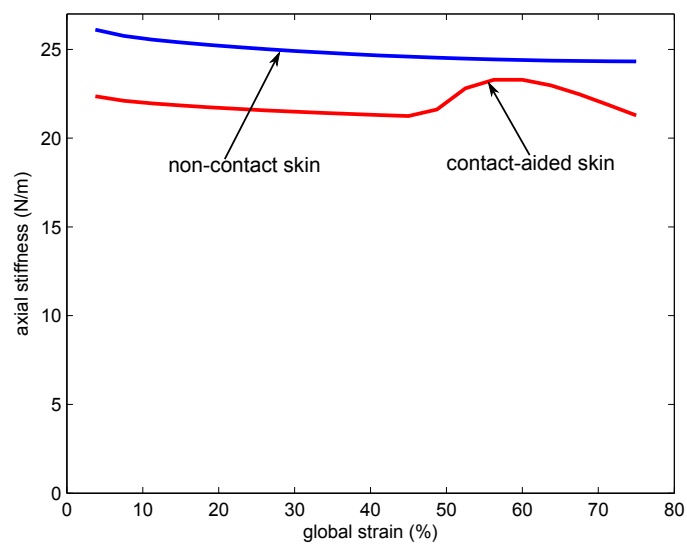


**Figure 4.9.** Equivalent in-plane stiffness of skin

**Table 4.4.** Design of morphing skin for contact-aided cellular structure using linearly elastic material model (NC - contact mechanism is present but not used, C - contact mechanism is used). Shaded rows indicate infeasible designs

$(n, n_{se})$	$\rho_{cell}$	$w$	$\theta$	$\sigma_{\max}$	$\sigma_{\max}$	$m_t$	$\gamma$
		mm	deg	MPa (NC)	MPa(C)	g	mm
(7,3)	1682	15.2	-16	29.6	NA	552	NA
(7,4)	2755	9.1	-15	34.3	NA	416	NA
(7,5)	4082	6.0	-14	39.1	35.4	327	1.07
(8,3)	1927	11.6	-14	23.3	NA	467	NA
(8,4)	3155	7.1	-14	30.5	NA	361	NA
(8,5)	5391	3.3	-15	46.1	38.1	199	0.86
(9,3)	2655	5.4	-16	35.6	NA	238	NA
(9,4)	4200	3.8	-14	38.1	35.8	209	1.06
(9,5)	6882	2.1	-15	52.2	47.0	145	0.78

in reducing the structural mass but in lowering the actuator requirements due to lower stiffness.

#### 4.4.2 Transverse Stiffness

Figure 4.10 shows a normalized variation of the maximum out-of-plane deformation ( $\delta/c$ ) with global strain. Here the best designs for non-contact and contact-aided skin using a nonlinear material model is used. Because of the pillowing constraint, the maximum value in each case is 0.001. If the transverse stiffness is defined as the total out-of-plane load divided by the maximum out-of-plane deflection, the transverse stiffness of every feasible design is same ( $= 53400 \text{ N/m}$ ), but the stiffness per unit mass for the contact-aided structure is  $376 \text{ N/kg-m}$ , while that for the non-contact structure is  $288 \text{ N/kg-m}$ . Therefore, the contact improves the stiffness-to-weight ratio of the cellular structures.

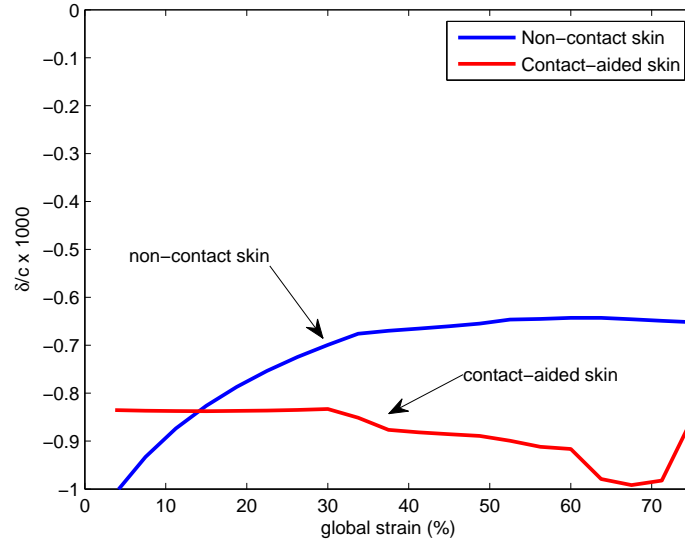


**Figure 4.10.** Variation of the maximum perturbation against the morphing strain

### 4.4.3 Silicone Sheet

As indicated in Figure 4.1, the cellular skin can be covered by a highly flexible membrane such as a silicone sheet to provide a smooth surface to resist airloads. Under the aerodynamic loads, this membrane may also be deformed transversely. Assuming a cell shape is rectangular with edges  $h$  and  $2l$ , the maximum deflection in the Z-direction ( $z_{\max}^{\text{silicone}}$ ) can be adopted from [94] as,

$$z_{\max}^{\text{silicone}} = \frac{16p_0}{\pi^6 D} \sum_{i=1,3,\dots}^{\infty} \sum_{j=1,3,\dots}^{\infty} \frac{-1^{\frac{i+j}{2}-1}}{ij [(i/h)^2 + (j/(2l))^2]^2} \quad (4.15)$$

where  $D = \frac{E_s w_s^3}{12(1-\nu^2)}$ . The modulus of elasticity,  $E_s$ , and Poisson's ratio,  $\nu$ , of silicone are assumed to be 3.6 MPa and 0.5, respectively [95]. The out-of-plane thickness of a silicone sheet  $w_s$  is estimated such that the out-of-plane deflection of the sheet is less than 0.001 times the root chord. For initial estimation,  $h$  and  $l$  are assumed to be 10 mm and 20 mm, respectively. For non-contact design, the required thickness for silicone sheet is about 3.5 mm. Since the contact mechanism provides additional support in the transverse direction to the silicone sheet, the required thickness for the contact-aided design is about 1.8 mm – about 50% less.

The axial stiffness of the silicone sheet is given as  $E_s w_s c / b$ , which corresponds to about 3.7 kN/m for contact-aided skin – substantially higher than the bare cellular mechanism. This is due to the thick solid sheet. However,  $h$  and  $l$  decrease with higher cell density, which reduces both the silicone sheet thickness and its axial stiffness.

## 4.5 Prediction of Morphing Strain using Analytical Model

The analytical model developed in Chapter 3 can be used to estimate the maximum global strains in the case of the linear material model. The lengths for the unit cell are calculated using Eqns. 4.5 and 4.6. The cell angle is taken from Tables 4.3 and 4.4. The variation of maximum global strain with cell density is shown in Figure 4.11. As the cell density increases, the capability of providing maximum global strain decreases. However, the morphing strain capability of a contact-aided skin is more than that of a non-contact skin. Apparently, the rate of decreasing the global strain capability is also smaller for contact-aided skin than that for non-contact skin.

The maximum global strain can also be estimated using FEA. The entire half span of the wing is modeled in ANSYS as described in Section 4.2.3. The applied global strain is incremented gradually. Keeping the global strain fixed, the initial contact gap is then reduced to decrease the maximum stress. The process is continued until the maximum stress cannot be reduced below the allowable stress for any lower value of contact gap. A comparison of maximum global strains and the corresponding initial contact gaps using the analytical model and FEA is given in Table 4.5.

The analytical model does not account for any aerodynamic loads, but it gives a very good estimate of designs that can provide the required morphing capability. From Table 4.5, the maximum error in the prediction of maximum global strain using the analytical model is less than 8%, while that in the prediction of contact gap is less than 18%. The model also demonstrates that, as the cell density increases, the maximum global strain decreases. According to Tables 4.3 and 4.4, the struc-

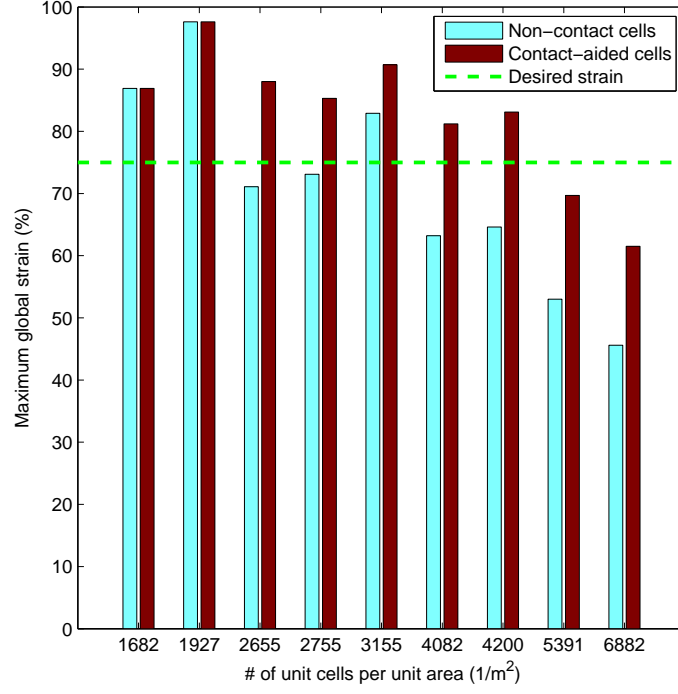


**Figure 4.11.** Comparison of maximum global strain for non-contact and contact-aided cellular skin for various data points

**Table 4.5.** Comparison of maximum global strain and initial contact gaps using analytical model and FEA

$\rho_{cell}$	Maximum global strain (%)			Contact gaps (mm)	
	Theory	FEA	error	Theory	FEA
1682	90	89	1.1	2.2	2.7
2655	87	85	2.4	1.5	1.4
2755	90	87	3.4	1.4	1.4
3155	89	89	0.0	1.2	1.2
4082	81	77	5.2	1.0	1.0
4200	83	79	5.1	1.0	1.0
5391	70	65	7.7	0.9	0.9
6882	61	57	7.0	0.3	0.4

tural mass decreases with the cell density. Therefore, there exists a ‘sweet-spot’ at which the skin consisting of linear material has minimum mass while providing the required morphing strain.

#### 4.5.1 Optimization

The preceding analysis shows that a multi-objective optimizer along with the analytical model can be employed to investigate the trade-off between the maximum global strain ( $\epsilon_{\max}^{global}$ ) and the structural mass ( $m_t$ ) for a morphing skin. The optimization problem is formulated as the following.

$$\begin{aligned}
 & \min \quad m_t \\
 & \max \quad \epsilon_{\max}^{global} \\
 & \text{subject to,} \\
 & \sigma_{\max} - \sigma_{all} < 0 \\
 & \delta/c - 0.001 < 0 \\
 & \theta_{\min} \leq \theta \leq \theta_{\max}
 \end{aligned} \tag{4.16}$$

The design variables are  $n$ ,  $n_{se}$ ,  $m$ ,  $m_{se}$ ,  $\theta$ , and  $t$ . The maximum global strain and the required contact gap are obtained from the analytical model for given values of  $n$ ,  $n_{se}$ ,  $m$ ,  $m_{se}$ , and  $\theta$ . Such a structure is then analyzed in ANSYS to determine the out-of-plane thickness ( $w$ ) so that the pillowing constraint is satisfied. The cellular geometry along with the out-of-plane thickness determines the structural mass. The variables such as  $n$ ,  $n_{se}$ ,  $m$ , and  $m_{se}$  are integer variables, while  $\theta$  and  $t$  are continuous variables. This makes the optimization problem in Eqn. 4.16 to be a mixed-integer, nonlinear, and non-differentiable. An evolutionary algorithm based optimizer is thus implemented. The Non-dominated Sorting Genetic Algorithm (NSGA-II) [87] has shown a great promise in tackling such multi-objective problems in the past and is therefore implemented here.

A FE simulation is required to estimate the out-of-plane thickness. Since one such estimation takes about 10-15 minutes of computational time, only a limited range of variables are considered. In-plane thickness ( $t$ ) is assumed to be constant

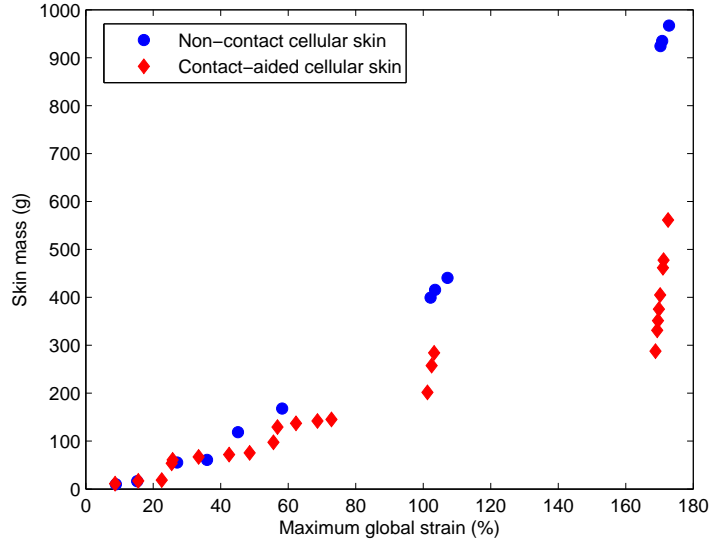


**Figure 4.12.** Plot showing the trade-off between the structural mass and the maximum global strain

at 1mm. The other bounds are given as the following.

$$\begin{aligned}
 n &\in [7, 9] \\
 n_{se} &\in [3, 5] \\
 m &\in [4, 7] \\
 m_{se} &\in [1, 2]
 \end{aligned} \tag{4.17}$$

The results using the preceding bounds are shown in Figure 4.12. These results clearly show the tradeoff between structural mass and morphing capacity for both non-contact and contact-aided cellular skins. The designs for contact-aided skin, however, are lighter than the non-contact structures while providing the same morphing or overall strain capability. Moreover, skin mass increases with the capacity of providing the maximum global strain for both non-contact and contact-aided cellular skin. The lighter designs have higher cell density than those having more morphing strain capabilities. Designs with very high cell density resemble to traditional solid skins having the least mass. Skins with big compliant cellular walls have lower cell density but higher morphing strain capability. The structural mass, therefore, needs to be higher to obtain higher morphing strains.

## 4.6 Summary

This chapter describes a morphing aircraft skin problem and provides a solution algorithm and sample results. All the designs based on nonlinear material are feasible, but contact-aided designs are superior in terms of total mass because of the transverse stiffening induced due to contact. Some of the designs based on a linear material model are not feasible, and some are made feasible using stress relief provided by the contact. Thus contact-aided compliant mechanisms can be promising candidates for morphing skin designs. Notably, skin for RC aircraft is considerably heavy with or without contact. The number of connection points and the number of cells considered were, however, very small due to high computation cost. With higher cell density, lighter designs could be possible. Moreover, the results correspond to the concept, where skin is connected to the underlying morphing actuators only at a discrete number of points. If skin is also connected to the morphing actuators along the edges, then the structural mass can be reduced.



# Meso-Scaled Cellular Structures

## 5.1 Introduction

Another application of the proposed cellular structure is to meso-scaled components. Cellular contact-aided compliant mechanisms in conjunction with meso-scale fabrication could result in potentially high-strain and high-strength lightweight materials. Design, fabrication, and testing of such meso-scaled cellular mechanisms are discussed in this chapter.

## 5.2 Design for Meso-Scale Manufacturing

Although Equations 3.22 (for global strain) and 3.26 (for initial contact gap) depend only on non-dimensional parameters, fabrication of compliant mechanisms at a meso-scale imposes many dimensional constraints. Two candidate materials are considered for the meso-fabrication of the proposed cellular structures – nanoparticulate 3 mol% yttria partially stabilized zirconia (3YSZ) and particulate stainless steel 316L. These materials are chosen due to their high strength, availability in particulate form, and ease of incorporation into the LMRIF process [49]. There are, however, manufacturing constraints that need to be applied to the overall design that stem from the mold fabrication, the particle size of the suspension that will be cast into the mold, and the aspect ratio of the final fabricated part.

The particle size of the suspensions that are cast into the mold, dictate the in-plane thickness of the final parts. In cross section, the final parts should have greater than 5 grains of material across any dimension (width and thickness) in order to ensure complete densification during sintering and structural integrity. The average particle size of the stainless steel is 10 microns, while that of the 3YSZ is 65 nm; dictating that the minimum in-plane thickness ( $t_{\min}$ ), as constrained by particle size, of the stainless steel should be greater than that of the 3YSZ. However, there is also a manufacturing constraint on the final aspect ratio of the fabricated part as well as the minimum feature size for a given mold thickness which will further constrain the final in-plane thickness.

In the fabrication process, a UV lithography process has been developed to create molds with out-of-plane thicknesses greater than 400 micron [96]. In this lithography step, there is a tradeoff between the mold thickness and the minimum resolvable in-plane feature size. Therefore, the out-of-plane thickness dictates the minimum manufacturable initial contact gap ( $\gamma_{\min}$ ). Secondly, similar to the in-plane thickness of the parts, the minimum out-of-plane thickness ( $w_{\min}$ ) is dependent on the particulate material system chosen. Therefore, the manufacturable contact gap also depends on the material used.

The final fabrication process yield has been shown to decrease with increasing aspect ratio of the parts [61]. In this study, Yuangyai et al. [61] determined the maximum aspect ratio to maximize the process yield. For cellular structures, the aspect ratio ( $AR$ ) is defined as the ratio of in-plane thickness to the maximum of length of the oblique wall or that of the horizontal wall. Mathematically,

$$AR = \frac{\max\{h, l\}}{t} \quad (5.1)$$

Such an aspect ratio should be less than 50 for stainless steel components and less than 20 for 3YSZ components [61,62]. The low allowable aspect ratio for the 3YSZ parts, dictates that the in-plane thickness should be greater than that required by the particle size constraint.

Given all the constraints, the minimum feature size, out-of-plane mold thickness, in-plane part thickness, and aspect ratio for both the stainless steel and 3YSZ material systems are listed in Table 5.1. .

**Table 5.1.** Final combined design constraints for the fabrication of cellular contact-aided compliant mechanisms using 316L stainless steel and 3YSZ

Material system	$t_{\min}$	$w_{\min}$	$\gamma_{\min}$	max $AR$
3YSZ	150 $\mu\text{m}$	50 $\mu\text{m}$	50 $\mu\text{m}$	50
316L	50 $\mu\text{m}$	100 $\mu\text{m}$	100 $\mu\text{m}$	20

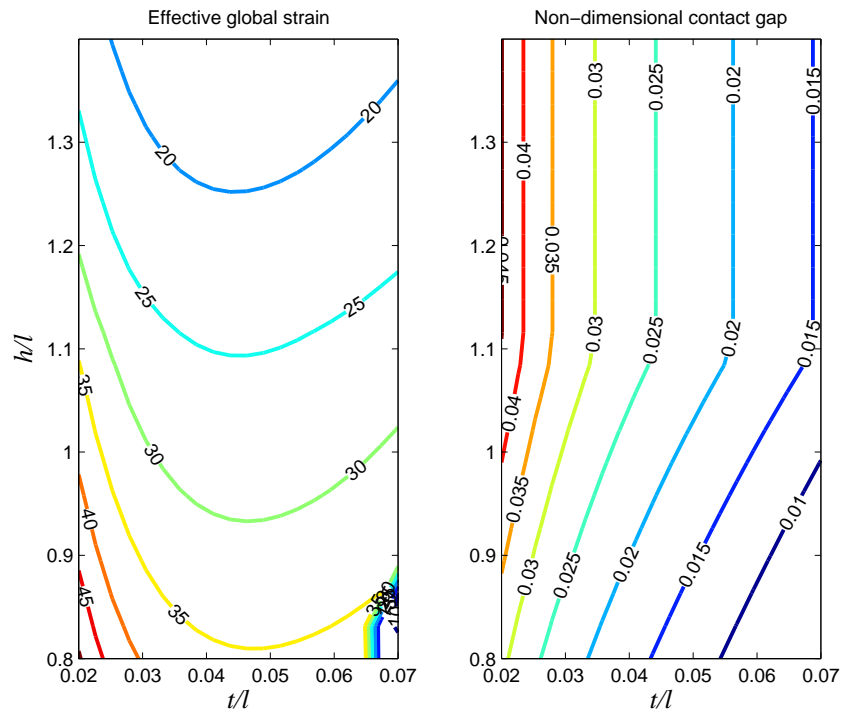


**Figure 5.1.** Contour plot of the effective strain and the non-dimensional initial contact gap for different unit cell geometries

The preceding manufacturing constraints are accommodated to design the contact-aided cellular mechanisms. Previous research suggests that the elastic modulus for 3YSZ is 200 GPa, while the ultimate strength is 590 MPa [50]. For an initial parametric study, the elastic modulus and yield stress for 316L stainless steel components is assumed to be the same at 200 GPa and 590 MPa, respectively. The size optimization study from Chapter 3 is utilized. Moreover, contour plots showing the variations of the effective strain and the initial contact gap for

different values of  $h/l$  and  $t/l$  are shown in Figure 5.1. FOS is assumed to be 1.4 in all geometries. Since smaller cell angles provide more effective strain [5, 7], the cell angle for Figure 5.1 is  $\min \left\{ \sin^{-1} \frac{h}{2l}, -\pi/6 \right\}$ . The ratio  $h/l$  is varied from 0.8 to 1.4 in steps of 0.1, while the ratio  $t/l$  is varied from 0.02 to 0.07 in steps of 0.01. These different values of  $h/l$ ,  $t/l$ ,  $\theta$ , and FOS are used in Equations. 3.22 and 3.26 to obtain the effective global strain (Figure 5.1(left)) as well as the non-dimensional contact gap (Figure 5.1(right)).

As seen in Figure 5.1, smaller  $t/l$  ratios favor more effective strain and bigger initial contact gaps. Although smaller  $h/l$  is good for providing high effective strain, bigger ratios are useful for bigger contact gaps for high  $t/l$  ratios. This is consistent with the findings from Chapter 3. For further analysis and design  $h/l$  is therefore assumed to be 1.4 in this work. A smaller wall thickness provides more effective strain. However, a thicker wall can have a larger contact gap. Due to this tradeoff, the wall thickness is designed based on the maximum aspect ratio. Since  $h > l$ , from Equation 5.1, the aspect ratio becomes

$$AR = \frac{h}{t} = \frac{h}{l} \frac{l}{t} \quad (5.2)$$

The ratio  $t/l$  can be calculated as the following.

$$t/l = \frac{1}{AR} \frac{h}{l} \quad (5.3)$$

Equations. 3.22 and 3.26 can now be used with these geometric parameters along with the material constants described earlier. To determine the dimensional values for the cellular geometry, the non-dimensional initial contact gap ( $\gamma/l$ ) and the minimum possible contact gap ( $\gamma_{\min}$ ) are considered as given in the following equation.

$$l = \frac{\gamma_{\min}}{\gamma/l} \quad (5.4)$$

Once the length of the oblique wall ( $l$ ) is known, the length of the horizontal wall ( $h$ ) and the in-plane thickness ( $t$ ) can be obtained from the ratios  $h/l$ , and  $t/l$ , respectively. If the in-plane thickness ( $t$ ) found by this approach is less than the

manufacturable value ( $t_{\min}$ ), then

$$t = t_{\min} \quad (5.5)$$

$$(5.6)$$

With this in-plane thickness ( $t$ ), the lengths of the oblique wall and of the horizontal wall can be determined using the non-dimensional ratios  $t/l$ , and  $h/l$ , respectively.

The preceding approach ensures that all manufacturing constraints are addressed. The overall length ( $L$ ) and the overall width ( $W$ ) of a cellular structure at no load are given as the following.

$$L = 2n(h + l \sin \theta) \quad (5.7)$$

$$W = 2ml \cos \theta \quad (5.8)$$

where  $n$  and  $m$  are the number of rows and columns in a cellular structure, respectively. The geometrical equations derived earlier are employed to estimate the overall length ( $L$ ) and the overall width ( $W$ ) of a single cell ( $n = 1, m = 1$ ) for different values of aspect ratios ( $AR$ ) and minimum contact gaps ( $\gamma_{\min}$ ). The results are shown in Figures 5.2 and 5.3. The figures show that a cell gets smaller for large aspect ratios and small contact gaps. Manufacturing at the meso-scale allows only either high aspect ratios (e.g., using 316L stainless steel) or small contact gaps (e.g., using 3YSZ). To resolve this conflict, two separate designs are selected. One design has a higher aspect ratio but a larger contact gap – specifically suitable for fabricating 316L stainless steel components. Another design has a lower aspect ratio and a smaller contact gap – particularly suitable for 3YSZ components. The geometric parameters for these designs are summarized in Table 5.2. Here  $M = \epsilon_x^{global} / (\sigma_{all} / E)$  is a “magnification factor”, which represents a magnification of strain in the overall sense from the local allowable strain of the constitutive material. The contact mechanism increases the magnification ratio by about 240% for geometry I and by about 24% for geometry II than the corresponding cellular structure without contact. Notably, one could potentially choose a single design with a lower aspect ratio and larger contact gap. The size of such a cell, however, is about four times bigger than the ones in Table 5.2.

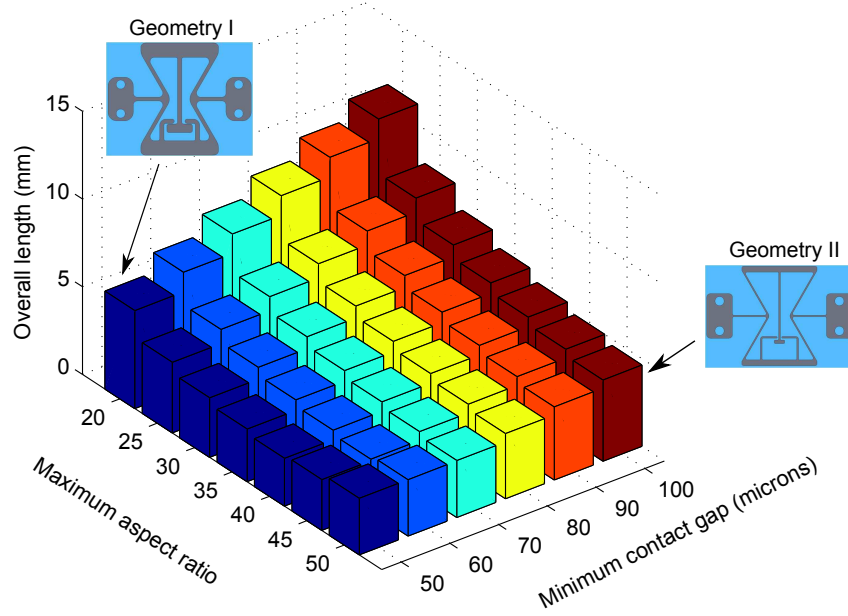


**Figure 5.2.** The overall length of a single cell for different aspect ratios and minimum possible initial contact gaps

The LMRIF process is employed to fabricate the meso-scale cellular structures. Three material systems have also been successfully incorporated into the process: 316L stainless steel (Figure 5.4b), 3mol%yttria stabilized zirconia (3YSZ), and a composite 316L stainless steel with 3YSZ (Figure 5.4a).

### 5.3 Experiments

This section describes an experimental setup to estimate the elastic modulus of 316L stainless steel. Additionally, some of the fabricated components are tested for their force-displacement characteristics using a custom test rig. The experimental results are compared with those predicted by the numerical model.

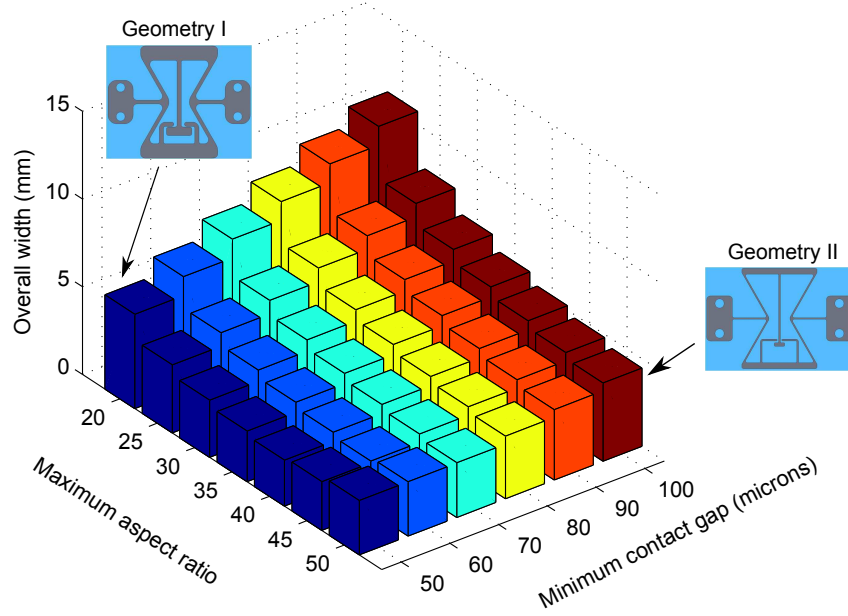


**Figure 5.3.** The overall width of a single cell for different aspect ratios and minimum possible initial contact gaps

### 5.3.1 Estimation of Elastic Modulus of 316L Stainless Steel

Although the elastic modulus of the bulk stainless steel is known, no data is available for the modulus of meso-scaled stainless steel parts fabricated using LMRIF process. To estimate the modulus, custom test bars were prepared using 316L stainless steel. A photo of one such test bar is shown in Figure 5.5 along with its nomenclature. A total of seven such bars were prepared and tested. The average width and thickness of these bars were  $0.94 \pm 0.07$  mm, and  $0.33 \pm 0.02$  mm, respectively. A screw-driven Instron 5866 material testing machine was used for the testing. A load cell of 100 N was used to measure the stretching force. A non-contact laser extensometer (E-I-R, model: LE-05) was employed to measure the strains. The experimental setup is shown in Figure 5.6. As shown in the figure, pneumatic grips were used to clamp the test specimen. Reflective tapes are needed to measure the strain using the laser extensometer, and the distance between these tapes constitute the gage length of the specimen. The loading speed was 0.1 mm/min. All seven test bars were tested and a typical stress-strain plot

**Table 5.2.** Two candidate geometries for meso-scale cellular contact-aided compliant mechanisms

Parameter	Geometry I	Geometry II
$AR$	20	50
$\gamma$	100 microns	50 microns
$h$	5.4 mm	4.1 mm
$l$	3.8 mm	2.9 mm
$t$	269 microns	82 microns
$\theta$	$-30^\circ$	$-30^\circ$
$M$ (non-contact)	4.7	11.8
$M$ (contact-aided)	16.5	14.5

is shown in Figure 5.7. There is noise at relatively low values of strain (less than about 0.2%). This noise is not only due to the inherent resolution and nonlinearity of the extensometer for small gage lengths (about 6-7 mm), but also due to the factors arise from the surrounding such as vibrations and fluorescent lights. However, the data demonstrates a typical strain-hardening behavior, and the slope of a best-fit line through the linear range of data gives an estimate of the elastic modulus. The data having strains less than 0.2% was used to get the best-fit estimate. With seven samples, the average modulus was found to be 110 GPa with a standard error of  $\pm 40$  GPa. This value can now be used to validate the cellular contact-aided compliant mechanism results with the numerical model. The bulk stainless steel modulus is about 200 GPa. A lower value of modulus for meso-scale stainless steel 316L components can be attributed to the manufacturing process and the material systems implemented.

### 5.3.2 Experimental Setup

Since the cellular components are only a few millimeters wide and few hundred microns thick, commercially available tensile testing machines cannot be used. A custom test rig is therefore developed. A photo of this rig is shown in Figure 5.8. The test fixture consists of a movable platform supported by two guide rails. A digital force gage (Imada DPS-1) is mounted on this platform to measure the stretching force. This force gage can measure up to 4.903 N with an accuracy of



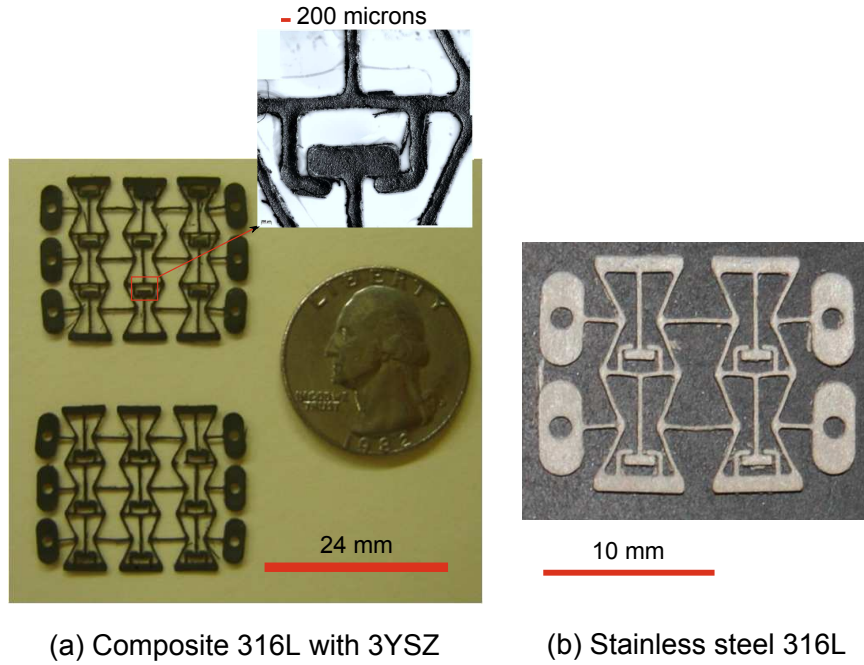


**Figure 5.4.** Photos of fabricated components (a) using composite 316L stainless steel with 3YSZ (b) using 316L stainless steel only

$\pm 0.2\%$  full scale. The force gage is connected to a set of grippers. The grippers are equipped with ball bearings to allow for free lateral movement, since cellular structures also deform in the lateral direction due to the effective Poisson's ratio. Another set of grippers are placed in front of the first set and are attached to a spring-loaded plate. Both sets of grippers are supported vertically on high precision balls so that the grippers create a horizontal plane on which to mount the components. The other side of the moving platform is rigidly connected to a micrometer shaft (Fowler 54-815-001). The body of the micrometer is attached to a fixed plate. This arrangement enables the micrometer not only to measure the stretching displacement, but also to drive the stretching process.

The grippers have an array of holes on their top surface as shown by the close-up view in Figure 5.8(right). To mount a specimen, it is placed on the horizontal plane created by the grippers. The parts also have a set of holes on each side. One set of holes on the specimen is aligned with those of the grippers attached to the force gage. Appropriate sized pins are used to fix the component to the grippers. The grippers attached to the spring-loaded plate are manually moved using a screw

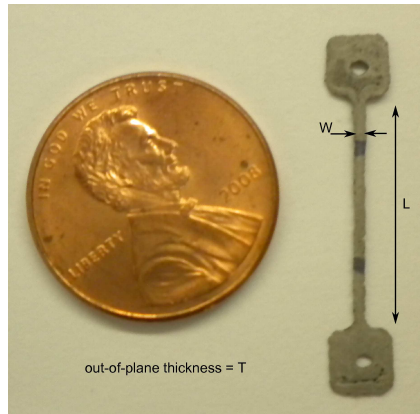


**Figure 5.5.** A 316L stainless steel bar that is used for the determination of the elastic modulus

and wing-nut arrangement until the other set of holes on the specimen aligns with those on the grippers. Pins are used again to fix the component on this side.

Both the force gage and the micrometer are connected to a computer using a RS-232 cable and a Human Interface Device (HID) cable, respectively. A software program based on Visual Basic 6.0 is developed to acquire force and displacement data at specified intervals.

To test a component, the micrometer thimble is slowly rotated to stretch the component. The force gage measures the stretching force. Both the force and displacement data are recorded on a computer for plotting as well as for further analysis. Moreover, to validate the stretching displacements, a digital camera (Nikon D90) is placed over the specimen. The resolution of the camera is  $4288 \times 2848$  pixels, and a 60mm micro lens is utilized to capture the images from a short distance (approximately 30mm). Images are taken at discrete values of stretching forces, and the corresponding extensions are estimated by post-processing these images.

### 5.3.3 Force-Displacement Testing

Since the displacements involved in the testing of the meso-scale components are relatively small, deformations of various parts of the fixture could be a significant factor in the measurements. To characterize the deformations caused solely by the

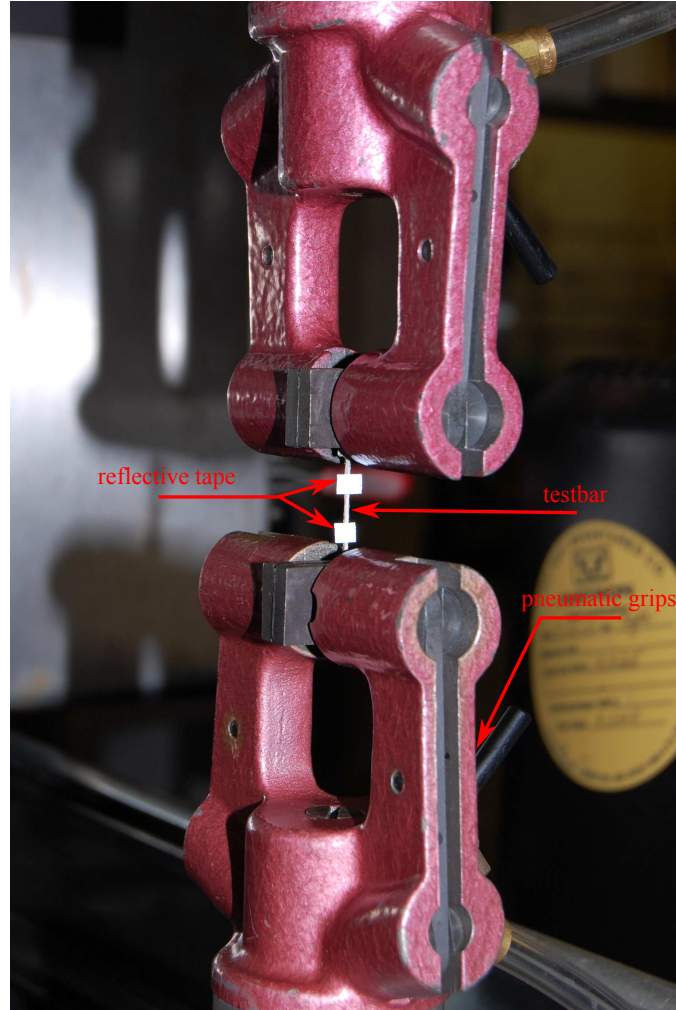


**Figure 5.6.** Experimental setup to estimate the elastic modulus of 316L stainless steel

fixture, the connectors were coupled to each other by a relatively rigid plate and the force-displacement characteristics were found. The rigid plate was made of commercial stainless steel and about 16 mm long, 9 mm wide, and 1.6 mm thick. For a stretching force of 5 N, the maximum strain is estimated to be less than 0.0001% and can therefore be neglected. With this rigid plate, the displacements observed for various stretching forces are found, and a typical plot is shown in Figure 5.9 along with a best-fit line. The relation between the stretching force and the nominal displacement can be linearly represented as the following.

$$F_s = k_f \delta_0 \quad (5.9)$$

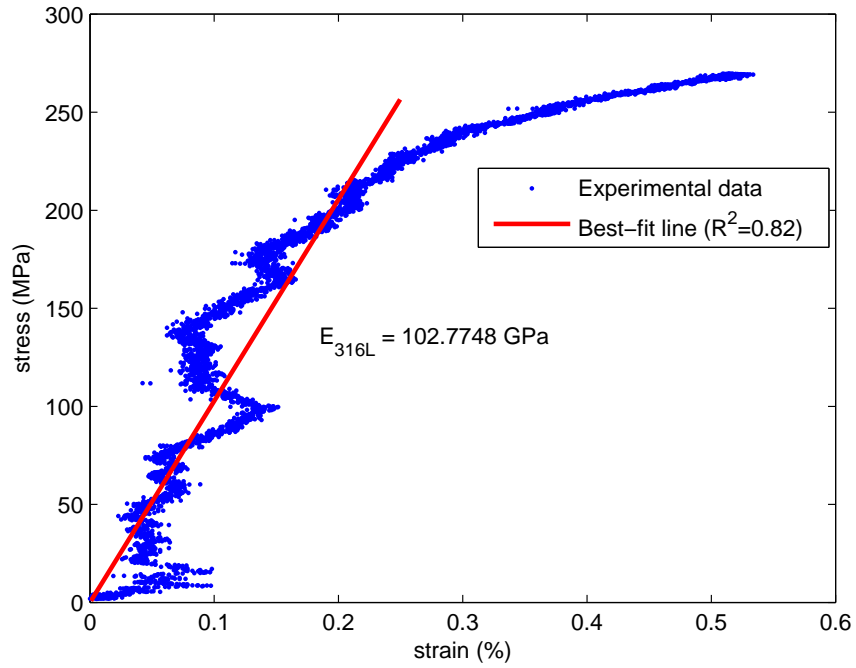


**Figure 5.7.** A plot of stress-strain characteristics for test bars using Instron testing machine

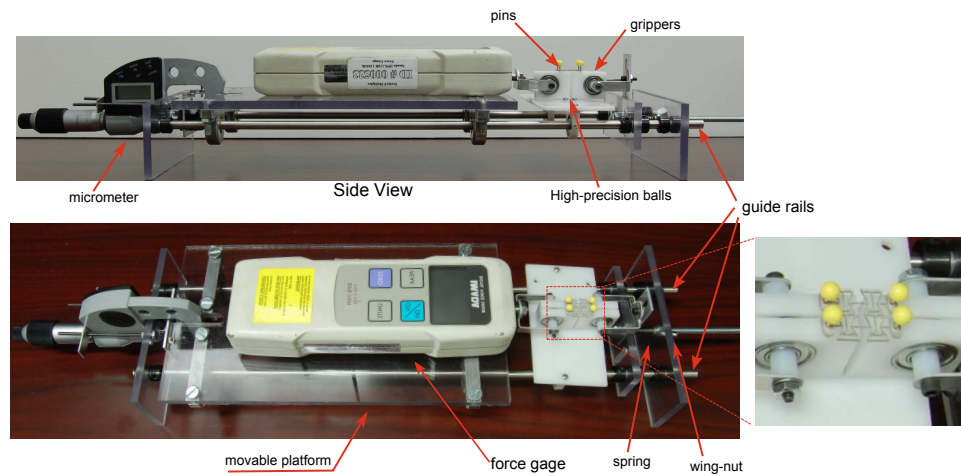


**Figure 5.8.** Photo showing the experimental setup for testing meso-scale cellular contact-aided compliant mechanisms

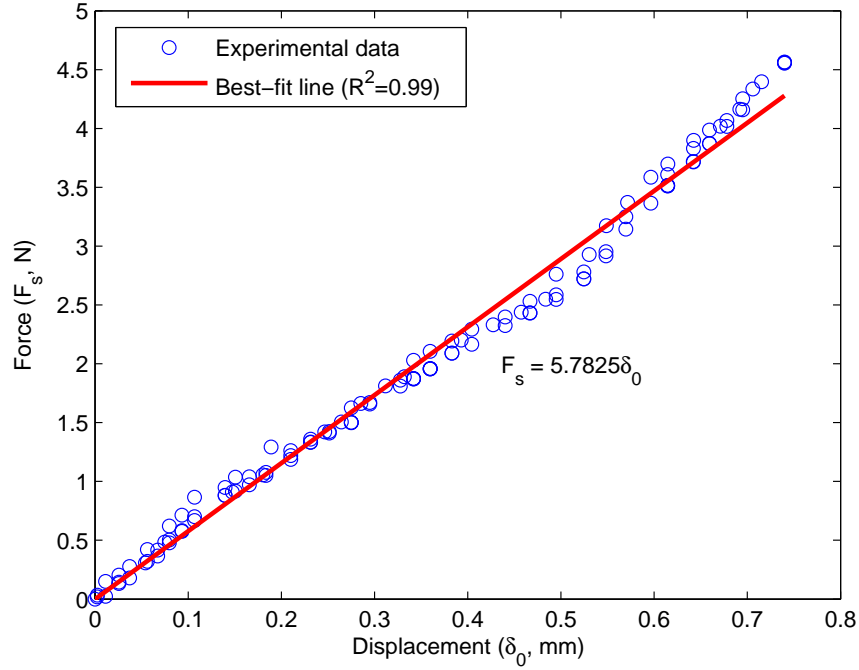


**Figure 5.9.** A typical characteristic of the fixture when connectors are coupled together by a rigid plate

where  $F_s$  is the stretching force measured in N and  $\delta_0$  is the nominal displacement in the fixture having units of mm.  $k_f$  represents the nominal fixture stiffness having units of N/mm. A total of 30 trials were conducted, and  $k_f$  was determined to be  $5.75 \pm 0.06$  N/mm.

Contact-aided mechanisms shown in Figure 5.4(b) are tested for their force-displacement characteristics. These mechanisms correspond to Geometry I in Table 5.2, and are fabricated using particulate 316L stainless steel. The final manufactured mechanisms were about 15 mm long in the X-direction and about 13 mm wide in the Y-direction. The lengths of the horizontal wall ( $h$ ) and that of the oblique wall ( $l$ ), the in-plane and the out-of-plane thickness were approximately 4.95 mm, 3.68 mm, 200 microns, and 260 microns, respectively. The micrometer thimble was rotated at a rate such that the stretching speed was approximately 0.01 mm/sec. The interfacing software was configured to record the force and displacement readings in 1s intervals. Every reading, therefore, corresponds to a

stretching increment of about 0.01 mm. Digital images were obtained every 1 N of stretching force to get another estimate of the extension.

The part dimensions described in the preceding were used to model contact-aided cellular mechanisms in ANSYS using beam elements for finite element analysis. BEAM23 elements were used to model different walls of the mechanism, while contact was modeled using CONTA172 along with TARGE169 as target elements. The boundary conditions for the analytical model (as shown in Figure 3.2) represent infinite rows and columns. The experimental specimen, on the other hand, has finite number of rows and columns. The cellular mechanism was, therefore, modeled as a finite sheet in FE simulation to emulate the boundary effects and the experimental setup. Five cells were modeled and no boundary condition is applied to top-most and bottom-most cell walls. To ensure that the top-most and bottom-most walls do not bend while testing, these walls were fabricated and modeled three times thicker than the rest of the walls. The left-most nodes are fixed in the X-direction and a displacement constraint is applied at the right-most nodes.

The elastic modulus was assumed to be  $110 \pm 40$  GPa in the finite element analysis, as estimated previously. The micrometer reads the total displacement ( $\delta$ ), which includes both the nominal fixture deformation ( $\delta_0$ ) and the specimen deformation ( $\delta_s$ ), such that

$$\delta = \delta_0 + \delta_s \quad (5.10)$$

The stretching force ( $F_s$ ) is the same for fixture as well as for the specimen, but since  $\delta_0 = F_s/k_f$ ,

$$\delta_s = \delta - F_s/k_f \quad (5.11)$$

where,  $k_f$  is the fixture stiffness. The overall cellular lengths ( $L$ , as shown in Figure 3.2) at various stretching forces can be estimated in pixels using any image processing software. In this work, freely available tpsDIG v2.14 (©2009 F. James Rohlf) was utilized. These digitized lengths gives another measure of specimen displacements. The stretching forces are plotted against such specimen displacements, and they are compared to finite element analysis.

Initially, the contact mechanisms in one such specimen were removed to further investigate the elastic modulus of meso-scale 316L stainless steel. The force-displacement characteristics for this ‘non-contact’ cellular mechanism is shown in

Figure 5.10. The experimental data (shown by blue circles) lies between the finite element prediction assuming the modulus to be 70 GPa and that assuming the modulus to be 150 GPa, which confirms the elastic modulus of meso-scale 316L stainless steel established in the preceding section. The figure also shows that experimental data found using the micrometer is very similar to that obtained using image processing. This validates the fixture assembly and the measurement methodology. Moreover, the elastic modulus of meso-scale 316L stainless steel found by a best-fit of both the experimental and image processed data is about 137 GPa. Notably, when the load is removed from the mechanism, it returns to its original configuration signifying no local permanent deformation and a global strain of about 4.7%. This value is four times higher than the theoretically predicted, and shows that further investigation is needed to find more accurate yield strength of the meso-scale 316L stainless steel components.

In the preceding analysis, the model is changed to fit the experimental data to estimate the elastic modulus. This process is similar to ‘theta testing’ [97].

Two cellular contact-aided compliant mechanisms were tested and typical force-displacement characteristics are shown in Figure 5.11. The solid lines represent the force-displacement characteristics of a contact-aided cellular mechanism estimated using FE analysis and assuming different values of elastic modulus. The experimental data is shown by blue circles, and the image processed data is shown by black diamonds. Clearly, both methods of measuring the specimen extensions yield similar characteristics. Both the experimental data and the image processed data show a significant change in slope, indicating the presence of contact. However, this change in slope does not occur at a specimen displacement predicted by the FE analysis. The contact surfaces in the fabricated mechanisms are very close to each other, due to burrs present in the contact gap. When the mechanism is stretched, the burrs in the contact gap are pressed together. The contact is therefore occurring gradually as seen in Figure 5.11. The burrs also reduce the effective contact gap, which causes the change in slope earlier than the predicted value.

Notably, when the load is removed from the mechanism for specimen displacements less than 0.30 mm (2.0% global strain), it returns to its original configuration signifying no local permanent deformation. This is illustrated in Figure 5.12, which shows the data for both the loading as well as unloading. The global strain for



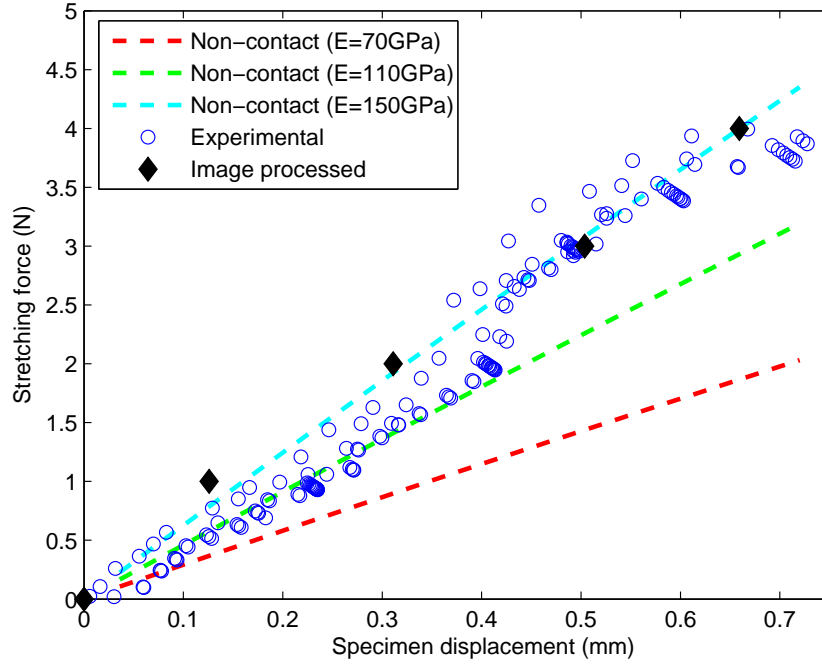


**Figure 5.10.** Force-displacement characteristics of a meso-scale 316L stainless steel non-contact cellular mechanism and comparison to FEA prediction

contact-aided compliant mechanisms is smaller than that of corresponding non-contact mechanisms. However, the contact-aided structures were not stretched further than 0.30 mm, due to the maximum force capacity of the force gage (4.9 N). Since the material properties (the elastic modulus and the yield strength) of meso-scale 316L stainless steel were not known, the designs are also not optimal. However, the experimental force-displacement characteristics match well with the finite element prediction, validating the design, fabrication, and testing methodology.

There are various parameters that can affect the modulus of elasticity of meso-scale components. LMRIF process consists of mold fabrication, colloidal preparation, casting, and sintering. Variations at each of these steps can potentially change the modulus of 316L stainless steel. The material used for photo resists and the types of mask induce burring in the final parts. The concentrations of various material systems as well as binders in the colloidal preparation change the final microstructure of the components. An uneven cast (having non-smooth



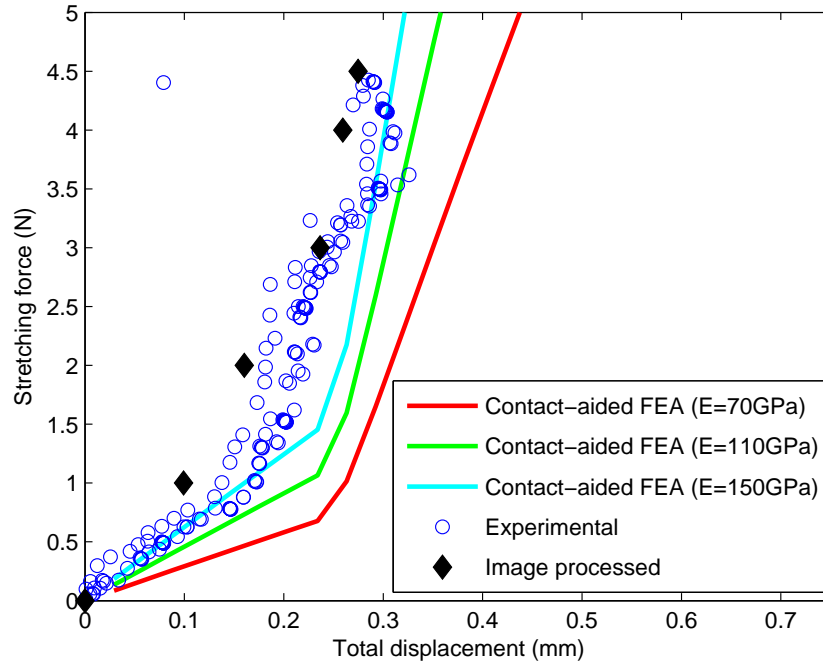


**Figure 5.11.** Force displacement characteristics of a meso-scale 316L stainless steel contact-aided cellular mechanism and comparison to FEA prediction

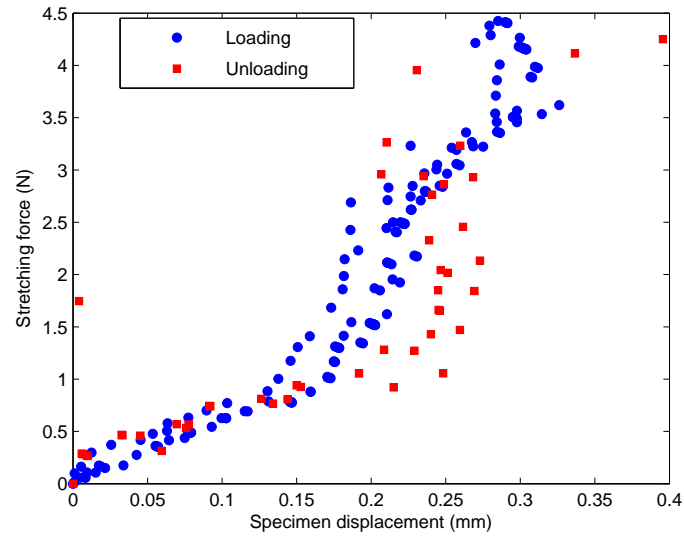


**Figure 5.12.** Force-displacement characteristics of a meso-scale 316L stainless steel contact-aided mechanism for both loading and unloading

edges and surfaces) can reduce the modulus of final parts substantially. Sintering involves complex thermodynamic and chemical processes. The different rates of heating and cooling cause reduction or oxidation in the material system causing a change in the material modulus.

## 5.4 Summary

This chapter investigates another application of the proposed cellular mechanism to meso-scaled components. The chapter presents a design methodology and the testing procedure suitable for meso-scaled parts. This application demonstrates that the proposed mechanism along with the novel fabrication process has the potential for creating a new micro-structure for high-strength, high-strain materials. The last two applications discussed involved a specific cellular contact-aided compliant mechanism. The next chapter discusses the design and synthesis issues for generalized cellular contact-aided compliant mechanisms.

# Synthesis of Cellular Contact-Aided Compliant Mechanisms

## 6.1 Introduction

Although there has been work related to topology optimization of cellular structures as well as contact-aided compliant mechanisms, synthesis of contact-aided cellular mechanisms utilizing stress relief has not been addressed. In the work so far, a contact-aided compliant cellular mechanisms with pre-determined topology was presented. This topology exhibits stress relief [5]. In this chapter, topology optimization methods are used to design more general mechanisms for desired properties.

The synthesis of contact-aided cellular mechanisms is a complex problem. Methods focusing on the synthesis of cellular structures employ linear finite element analysis [76,81], while nonlinear analysis is necessary to address contact and large deformation. Topology optimization schemes for contact mechanisms assume a known location for contact pairs [69,82]. If the contact surfaces and initial contact gaps are not predetermined, the optimization problem becomes more complex. As mentioned earlier, contact mechanisms can be used to reduce the maximum stress in a cellular structure [5]. However, a unified optimization procedure cannot indicate whether any such contact mechanism reduces the maximum stress in a cellular structure. Apparently, one needs to design a cellular

**Table 6.1.** Comparison of two stages used in the synthesis of contact-aided cellular mechanisms

	Stage I	Stage II
	Non-contact cellular structure	Contact-aided mechanism
Objective function	Inverse homogenization	Stress relief
Constraint	Maximum local strain	Non-overlapping members
Finite element	Quad elements	Frame elements
FE analysis	linear	non-linear
Modeling	SIMP	Ground structure
Optimizer	MMA	DE

structure without contact to start. Contact mechanisms can then be added to such a structure to reduce the maximum stress.

A two-step approach is implemented here. A non-contact cellular structure is designed first using classical topology optimization tools, which is followed by the addition of one or more contact mechanism(s) for stress relief. The optimization problems, methods, and optimizers are different for these two stages as summarized in Table 6.1. The methodology is further illustrated in Figure 6.1. The flow chart shows that the methodology initially designs the non-contact cellular structure using inverse homogenization as the objective function and the maximum local strain as the constraint. This stage is executed with planar elements and the SIMP approach. The non-contact continuum topology is then converted into its frame equivalent, and a constraint is utilized to find all the non-overlapping designs. All of the non-overlapping designs are investigated for potential stress relief. Initial contact gaps for the designs that yield stress relief are optimized to maximize the stress relief and to obtain the final cellular contact-aided compliant mechanism. This chapter presents the synthesis process for both non-contact and contact-aided cellular mechanisms and some results based on that.

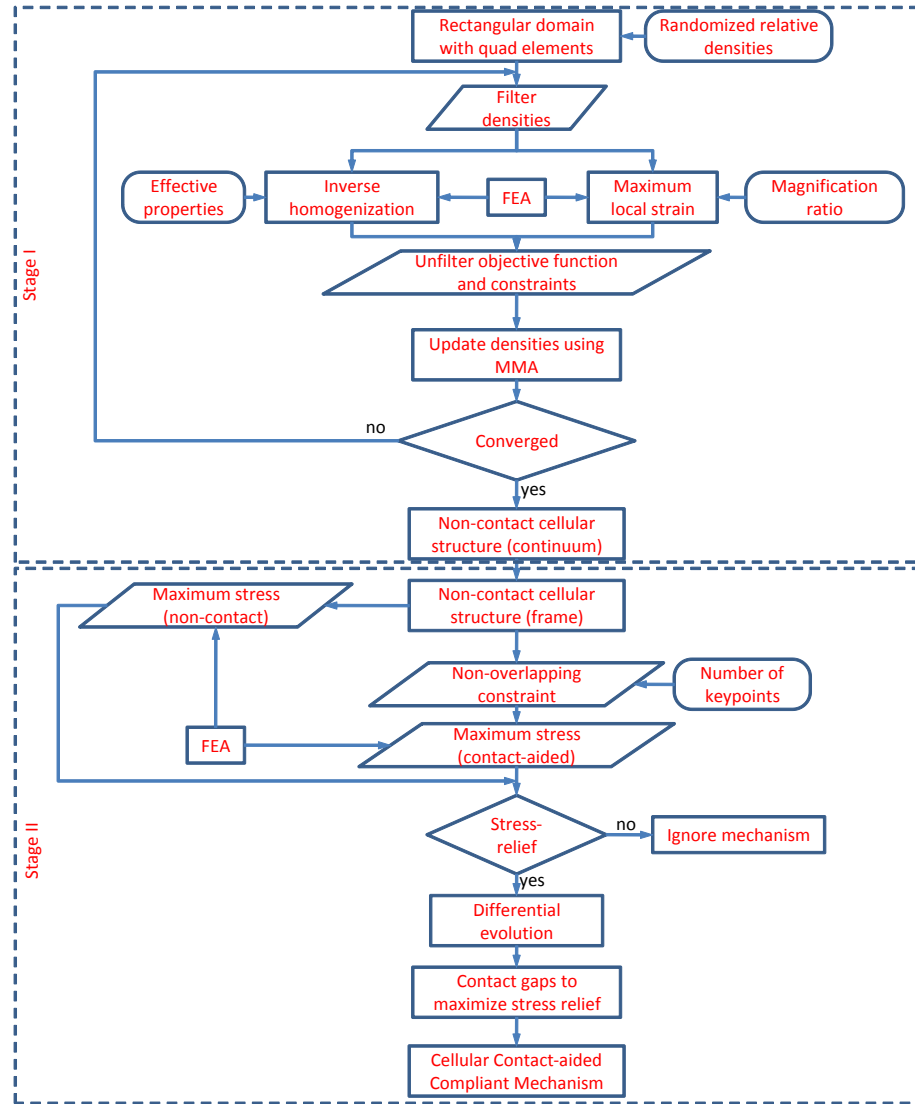


**Figure 6.1.** A flow chart showing the two-stage topology optimization methodology for designing cellular contact-aided compliant mechanisms

## 6.2 Topology Optimization of Non-Contact Structures

The first stage for synthesizing stress-relieving cellular mechanisms is to develop a baseline non-contact cellular structure. The scheme described in this stage is similar to a classic inverse homogenization problem. To enforce topologies for high strain applications, an additional strain constraint is incorporated. This section

develops the basic tools required to formulate and solve the optimization problem for such non-contact designs. It presents a topology optimization method, a scheme to find the homogenized elasticity coefficients, and a strategy to estimate the maximum local strain. It also describes the optimization problem and the corresponding solution methodology.

### 6.2.1 Solid Isotropic Material with Penalization (SIMP)

SIMP is a popular method used to tackle topology optimization problems [70]. In this method, the domain is discretized into a number of finite elements. In the present work, a rectangular domain is considered and discretized using uniform rectangular elements as shown in Figure 6.2. The number of elements in the X-direction is  $N_x$  and that in the Y-direction is  $N_y$ . Quadrilateral elements with two degrees of freedom at each node are chosen for the analysis. The length and width of each element is  $\Delta_x$  and  $\Delta_y$ , respectively. In the SIMP approach, the elastic modulus of each element is penalized using a power law on the constitutive elastic parameters. The relative density of each element is then a variable in a layout optimization problem. Mathematically, the modulus of elasticity of  $e$ -th element ( $E_e$ ) is given by

$$E_e = E x_e^p \quad (6.1)$$

where  $E$  is the Young's modulus of the constitutive isotropic material,  $x_e$  is the relative density of the  $e$ -th element, and  $p$  is the penalty factor [70]. Appropriate boundary and loading conditions are applied to calculate the objective function using the finite element (FE) method. Linear FE analysis is employed for topology optimization of the cellular structures without contact, since most SIMP-based schemes assume linear modeling and linear analysis is computationally fast. In this work,  $p$  is assumed to be 3, and  $\Delta_x$ ,  $\Delta_y$  are assumed to be unity. For visualization, an element with a relative density close to 1 is shown by black color, while that with a relative density close to 0 is shown by white color. The intermediate densities are indicated by gray color.

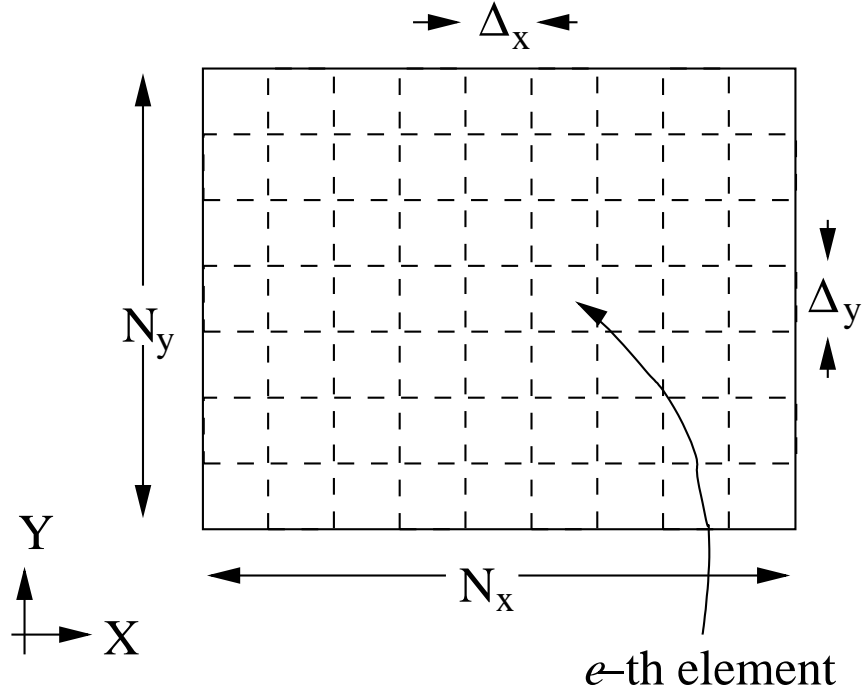


**Figure 6.2.** Finite element meshing for SIMP model

### 6.2.2 Homogenization

For a transversely isotropic material, the generalized Hooke's law (in planar 1-2 coordinates) can be given as follows

$$\begin{Bmatrix} \sigma_1 \\ \sigma_2 \\ \tau_{12} \end{Bmatrix} = \begin{bmatrix} C_{11} & C_{12} & 0 \\ C_{21} & C_{22} & 0 \\ 0 & 0 & C_{33} \end{bmatrix} \begin{Bmatrix} \epsilon_1 \\ \epsilon_2 \\ \gamma_{12} \end{Bmatrix} \quad (6.2)$$

where  $\sigma_1$ ,  $\sigma_2$ , and  $\tau_{12}$  are the normal stresses in the X- and Y-directions and shear stress, respectively. Similarly  $\epsilon_x$ ,  $\epsilon_y$ , and  $\gamma_{12}$  are the normal strains in the X- and Y-direction and the shear strain, respectively. The  $C_{ij}$  represent the effective elastic constants for the material. These effective elasticity coefficients depend on the material microstructure or the unit cell of a cellular structure. The process of finding such effective or homogenized coefficients for a given microstructure is called homogenization. Homogenization theory and its implementation using

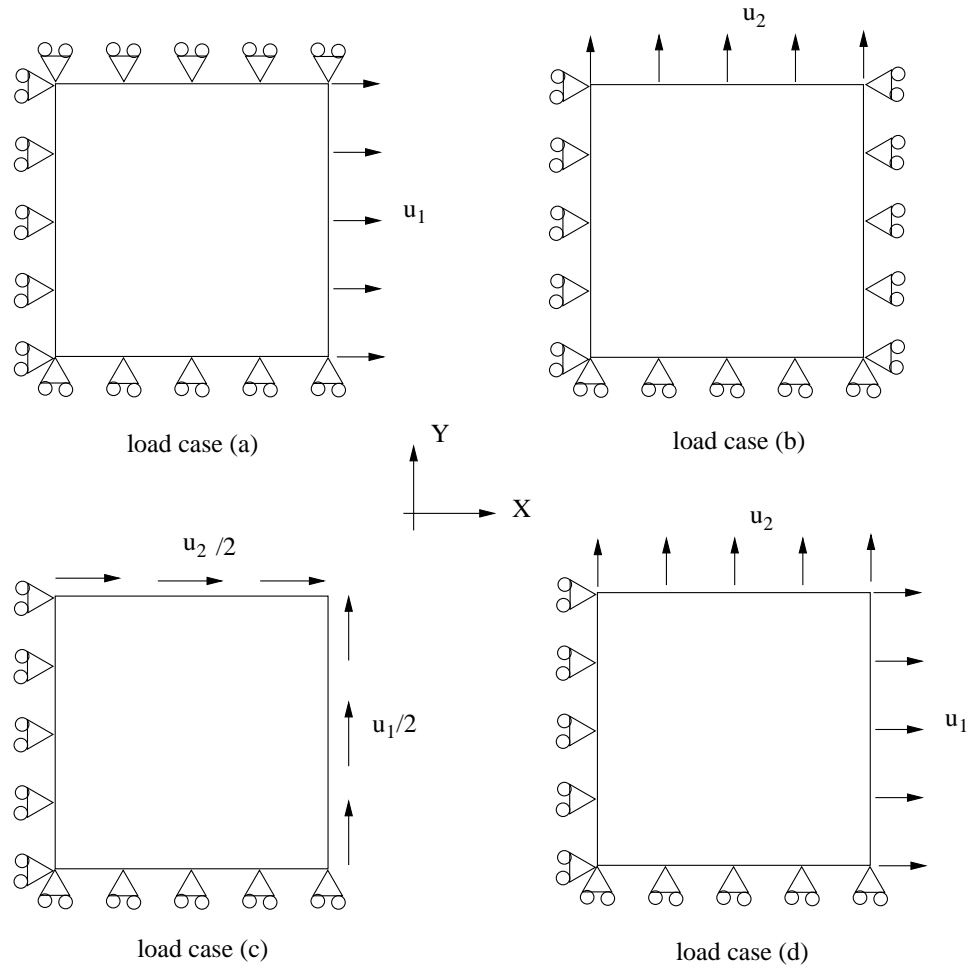


**Figure 6.3.** Load cases required to determine the homogenized elastic coefficients

finite element analysis is described in [74, 75]. Another implementation, which employs the so-called strain energy based approach to estimate the homogenized coefficients is presented in [98]. The strain energy-based method has a relatively simpler implementation and the sensitivity calculation is also straightforward. This approach is therefore adapted here to perform the homogenization. It comprises four different load cases as shown in Figure 6.3. These load cases and the strategies used to calculate the effective properties based on the strain energy are described in the following.

1. *Load case (a):* The boundary conditions are shown in the figure.  $u_1$  is the applied displacement in the X-direction. The boundary conditions represent



$\epsilon_1 = u_1/(\Delta_x N_x)$ ,  $\epsilon_2 = 0$  and  $\gamma_{12} = 0$ . If  $E_a$  is the strain energy for this load case, the effective value of  $C_{11}$  ( $C_{11}^H$ ) is given by

$$C_{11}^H = \frac{2E_a}{V\epsilon_1^2} \quad (6.3)$$

where  $V = \Delta_x N_x \Delta_y N_y$  is the total volume of the domain assuming unit thickness.

2. *Load case (b)*: As shown in the figure,  $u_2$  is the applied displacement in the Y-direction. Therefore,  $\epsilon_1 = 0$ ,  $\epsilon_2 = u_2/(\Delta_y N_y)$  and  $\gamma_{12} = 0$ . If  $E_b$  is the strain energy for this load case, the effective value of  $C_{22}$  ( $C_{22}^H$ ) is

$$C_{22}^H = \frac{2E_b}{V\epsilon_2^2} \quad (6.4)$$

3. *Load case (c)*: In this load case,  $u_1$  and  $u_2$  represent the shear displacements in the X and Y-direction, respectively. For such a loading,  $\epsilon_1 = 0$ ,  $\epsilon_2 = 0$  and  $\gamma_{12} = 1/2 (u_1/(\Delta_x N_x) + u_2/(\Delta_y N_y))$ . If  $E_c$  is the strain energy for this load case, the effective value of  $C_{33}$  ( $C_{33}^H$ ) is

$$C_{33}^H = \frac{2E_c}{V\gamma_{12}^2} \quad (6.5)$$

4. *Load case (d)*: To determine the off-diagonal terms, normal displacements  $u_1$  and  $u_2$  are applied as shown in the figure. In this case,  $\epsilon_1 = u_1/(\Delta_x N_x)$ ,  $\epsilon_2 = u_2/(\Delta_y N_y)$  and  $\gamma_{12} = 0$ . If  $E_d$  is the strain energy for this load case, the effective value of  $C_{12}$  ( $C_{12}^H$ ) is given by

$$C_{12}^H = \frac{1}{\epsilon_1 \epsilon_2} \left( \frac{E_d}{V} - \frac{1}{2} C_{11} \epsilon_1^2 - \frac{1}{2} C_{22} \epsilon_2^2 \right) \quad (6.6)$$

Here,  $u_1$  and  $u_2$  need not be unity. The sensitivity analysis of the homogenized coefficients using the preceding approach is straightforward as described in the Appendix A.

### 6.2.3 Maximum Local Strain

Cellular structures intended for high strain applications permit a large effective global strain before local failure occurs. This requires estimation of the maximum local strain in the structure for given loading conditions. Although a strain-based constraint is rarely used (e.g., [81]), topology optimization with stress constraints have been considered in the literature. There are two principal approaches to tackle stress constraints: either by considering the stress for every finite element [99] or by estimating the maximum stress for entire structure [100,101]. The calculation of local von Mises strain is very similar to the calculation of local von Mises stress. Since the local shear strains in the anticipated cellular structures are relatively small, their contribution towards the von Mises strain is neglected. Following [101], the elemental von Mises strain ( $\epsilon_{VM}$ ) is adapted as,

$$\text{Let, } S = \begin{bmatrix} 1 & -1/2 & 0 \\ -1/2 & 1 & 0 \\ 0 & 0 & 0 \end{bmatrix} \quad (6.7)$$

$$\text{and } M = B^T S B \quad (6.8)$$

$$\Rightarrow \epsilon_{VM}^2 = u^T M u \quad (6.9)$$

where  $B$  is the strain-displacement matrix and  $u$  is the vector of nodal displacements for  $e$ -th element. A void element can also have a non-zero strain with such an approach. To circumvent this problem, the elemental strain is penalized using the element density. The effective elemental strain ( $\epsilon_e$ ) for an element  $e$  is given by

$$\epsilon_e = \epsilon_{VM} x_e^{p/2} \quad (6.10)$$

where  $p$  is penalty factor, which is same as Eqn. 6.1. The maximum local strain ( $\epsilon_{\max}^{local}$ ) in the structure can be represented mathematically using the concept of vector norm [101] as follows

$$\epsilon_{\max}^{local} = \max_{e=1,\dots,N} \epsilon_e = \lim_{q \rightarrow \infty} \left( \sum_{e=1}^N \epsilon_e^q \right)^{1/q} \quad (6.11)$$

where  $N$  is the total number of elements in the domain. The norm representation gives a regularized expression for the maximum strain. In the actual implementation the exponent  $q$  is finite and, therefore, the measure of maximum local strain is a conservative estimate, i.e.,

$$\epsilon_{\max}^{local} = \left( \sum_{e=1}^N \epsilon_e^q \right)^{1/q} > \max_{e=1, \dots, N} \epsilon_e \text{ for } q \ll \infty \quad (6.12)$$

Higher values of  $q$  yield more accurate estimates for the maximum local strain, but also tend to exhibit numerical instabilities during the optimization process. In the present study,  $q$  is fixed at 4 to be consistent with the literature [101]. The sensitivity analysis for the maximum local strain is carried out using the adjoint method [102] and is summarized in Appendix A.

#### 6.2.4 Optimization Problem

Cellular structures may be characterized by their effective elastic properties. These elastic properties can therefore dictate the topology of a cellular structure. An inverse homogenization method is applied to find such a cellular topology. The optimization problem formulation is given as follows.

$$\begin{aligned} \min \quad & \left( 1 - \frac{C_{11}^H}{C_{11}^*} \right)^2 + \left( 1 - \frac{C_{12}^H}{C_{12}^*} \right)^2 + \left( 1 - \frac{C_{22}^H}{C_{22}^*} \right)^2 \\ & + \left( 1 - \frac{C_{33}^H}{C_{33}^*} \right)^2 \\ \text{s.t.:} \quad & f - \frac{\Delta_x \Delta_y}{V} \sum_{e=1}^N x_i \geq 0 \\ & 0 < x_{\min} \leq x_i \leq 1 \text{ for } i = 1, \dots, N \end{aligned} \quad (6.13)$$

where  $C_{11}^*$ ,  $C_{12}^*$ ,  $C_{22}^*$ , and  $C_{33}^*$  are the desired elastic properties of the resulting mechanism, and  $C_{11}^H$ ,  $C_{12}^H$ ,  $C_{22}^H$ , and  $C_{33}^H$  are the homogenized elastic properties of the structure.  $f$  is the volume fraction, which determines the quantity of material available for the distribution.  $x_{\min}$  is a small number to avoid singularity in the finite element formulation. The optimization problem in Eqn. 6.13 is the same as that in the literature (e.g., [76, 98]). Although such a formulation generates cellu-

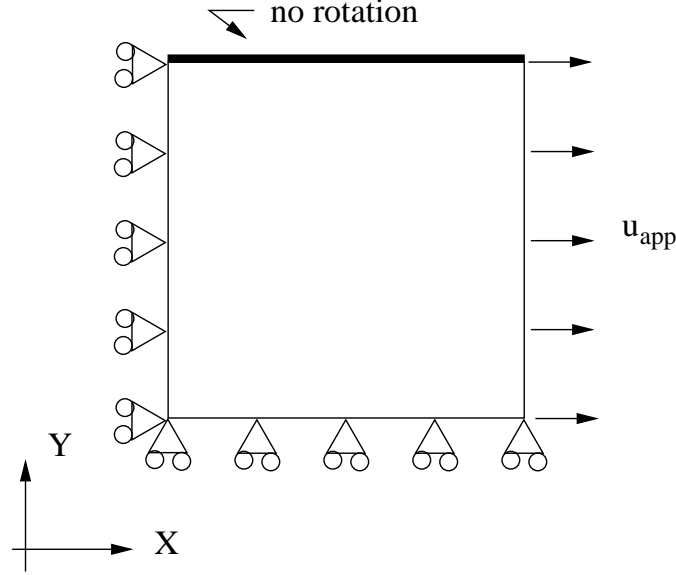


**Figure 6.4.** Boundary conditions and loads for local strain calculation

lar topologies, it does not explicitly address the maximum local strain. Cellular topologies which exhibit high overall strains are sought in this research; therefore, an additional strain constraint becomes necessary.

The boundary conditions and loads needed to find the maximum local strain are shown in Figure 6.4. As part of a cellular structure, the domain experiences periodic boundary conditions. The left and the bottom edges are constrained in the X- and Y-directions, respectively. The nodes along the top edge are coupled to move together in the Y-direction, without rotation. An external displacement of magnitude  $u_{app}$  is applied at the right edge. The overall effective uniaxial strain of the structure ( $\epsilon^{global}$ ), therefore, is  $u_{app}/(N_x \Delta_x)$ . The maximum local strain ( $\epsilon_{max}^{local}$ ) is calculated using the methods described earlier in the work. If  $\epsilon^{all}$  denotes the allowable local strain based on the constitutive material properties, then the strain constraint becomes

$$\epsilon_{max}^{local} \leq \epsilon^{all} \quad (6.14)$$

$$\Rightarrow \frac{\epsilon^{global}}{\epsilon_{max}^{local}} \geq M \quad (6.15)$$

$$\Rightarrow \epsilon^{global} - M \epsilon_{max}^{local} \geq 0 \quad (6.16)$$

where  $M = \epsilon^{global}/\epsilon^{all}$  is the magnification of local strain in a global sense and called ‘magnification ratio’. Since the applied external displacement ( $u_{app}$ ) is constant throughout the optimization, the magnification ratio dictates the maximum local strain.  $M$  is a measure of how effectively the cellular structure can deform compared to the bulk material. For structures demonstrating stress relief, the maximum local strain is reduced – increasing the magnification ratio. When Eqn. 6.16 is added to the optimization problem (see Eqn. 6.13) as a constraint, it completes the formulation for the design of cells without contact (stage I).

$$\begin{aligned}
\min \quad & \left(1 - \frac{C_{11}^H}{C_{11}^*}\right)^2 + \left(1 - \frac{C_{12}^H}{C_{12}^*}\right)^2 + \left(1 - \frac{C_{22}^H}{C_{22}^*}\right)^2 \\
& + \left(1 - \frac{C_{33}^H}{C_{33}^*}\right)^2 \\
\text{s.t.} \quad & \epsilon^{global} - M\epsilon_{\max}^{local} \geq 0 \\
& f - \frac{\Delta_x \Delta_y}{V} \sum_{e=1}^N x_i \geq 0 \\
& 0 < x_{\min} \leq x_i \leq 1 \text{ for } i = 1, \dots, N
\end{aligned} \tag{6.17}$$

where  $f$  and  $M$  are specified.

### 6.2.5 Optimizer

The optimization problems defined in Eqns. 6.13 and 6.17 consist of several variables and a number of constraints. Different optimizers have been suggested in the literature including sequential linear programming [76], optimality criteria [70], or genetic algorithms [81]. The Method of Moving Asymptotes (MMA) is a popular choice as an optimizer in the structural optimization community. The MMA optimizer approximates the problem as a convex solvable subproblem [103]. The MATLAB version of the MMA subroutine was obtained for academic purposes from Prof. K. Svanberg, KTH Royal Institute of Technology, Sweden.

The boundary conditions and the loads for the objective function and for the constraints are homogenous. If the initial state for the optimizer is uniform density over the entire domain, the sensitivity for both the objective function and the constraints have the same values for each design variable. This ‘locks’ the optimizer at

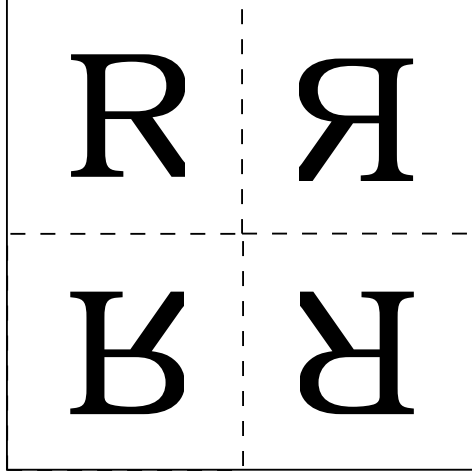


**Figure 6.5.** Periodic perturbations for random initial guess

the initial value without any change in the variables and without any improvement in the objective function. To overcome this problem, the uniform initial state is perturbed by small random values ( $< x_{\min}$ ). Moreover, to retain periodicity in the structure, the random perturbations are made in a quarter of the domain and these perturbations are reflected in the other quarters. This concept is depicted in Figure 6.5.

### 6.2.6 Filtering Technique

Ideally the final topology should consist of only solid elements (density = 1) and void elements (density = 0 or  $x_{\min}$ ), but usually there are many elements with intermediate densities (grey elements) when using the SIMP approach. Other problems with the SIMP approach include mesh dependent design and checkerboarding. These problems can be tackled using different ‘filtering’ techniques. A comprehensive review of such filtering methods can be found in [104] and [105]. Evidently, the Heaviside density filters and modified Heaviside density filters are often chosen in view of their performance and relatively low computational cost. These filters were originally presented by Guest et al. [106]. Since such filters are not volume preserving; Sigmund [105] has suggested cascading these filters to obtain a volume preserving filter.

A basic density filter can be given as [104],

$$\tilde{x}_e = \frac{\sum_{i \in N_e} w(x_i) x_i}{\sum_{i \in N_e} w(x_i)} \quad (6.18)$$

where  $N_e$  is the neighborhood of  $e$ -th element of radius  $R$  and  $w(x_i) = R - \|x_i - x_e\|$  represents a weighting function that depends on the distance between  $e$ -th element and a neighboring  $i$ -th element. These densities ( $\tilde{x}_e$ ) are further revised using a Heaviside step function and a modified Heaviside step function. The expressions are given as follows.

Heaviside step function:

$$\bar{x}_e = 1 - e^{-\beta \tilde{x}_e} + \tilde{x}_e e^{-\beta} \quad (6.19)$$

Modified Heaviside step function:

$$\bar{x}_e = e^{-\beta(1-\tilde{x}_e)} - (1 - \tilde{x}_e) e^{-\beta} \quad (6.20)$$

where the parameter,  $\beta$ , determines the sharpness of the Heaviside step function. Higher values of  $\beta$  imply more 0-1 designs, but they destabilize the convergence process. A value of 0.5 is used in this work. In the optimization process, the MMA optimizer updates the design variables. A density filter based on the Heaviside step function is first applied, which is followed by the density filter based on the modified Heaviside step function. The FE analysis is carried out using the filtered densities and the objective function, constraints, and their sensitivities are found. Since the sensitivities are based on the filtered densities, the sensitivities with respect to the original densities are calculated using the chain rule of differentiation.

## 6.3 Topology Optimization of Contact-Aided Mechanisms

Stage II of the synthesis process involves the determination of contact mechanisms in the cellular structure. As described in Table 6.1, the topology optimization approach, the modeling, and optimization problem for stage II are different than

those of stage I. This section defines the optimization problem, methodology, and optimizer for designing the contact mechanisms.

### 6.3.1 Frame Structure

As described in the preceding sections, non-contact cellular structures were found using continuum topology optimization approach. The continuum approach allows many more passive arrangements of members than a discrete topology optimization [70]. Linear FE analysis was also used to design non-contact structures. Contact, being a nonlinear phenomenon, requires a nonlinear FE analysis involving large displacements, which implies significantly higher computational cost for the analysis. Consequently, models used in contact-related topology optimization are best represented in a discrete form. [69, 82].

The maximum local strain is estimated using the norm approach (cf., Eqn. 6.12). This technique provides an approximate global measure as opposed to the exact maximum value. In applications involving stress relief, such a technique may not be able to capture small reductions in the maximum local strain. Moreover, in our conceptual design, stress relief involves an interaction between bending stress and normal stress [5]. In a continuum structure, it is not easy to separate these stresses. This is another reason to pursue stress-relieving contact mechanism in discrete form.

Cellular structures have been modeled using planar frame elements (i.e., 3 DOF per node) in the literature [2, 5, 7, 18]. The continuum cellular structures without contact developed in stage I are, therefore, converted to such frame structures. This idea is illustrated in Figure 6.6. The frame structure is created by defining a few ‘keypoints’ (say,  $n_k$ ) as shown in the figure. The number and location of these keypoints are determined by the designer. Contact is assumed to take place in a contact mechanism between any two keypoints. There are a total of  $\mathbf{C}_2^{n_k}$  single contact pairs possible in such a structure and, if any number of contact pairs are allowed, there are  $2^{\mathbf{C}_2^{n_k}} - 1$  possible solutions for the design of contact mechanism. Here  $\mathbf{C}$  represent the combinatorial operator. This approach is similar to a ‘ground structure’ approach [70]. Any such designs are analyzed using ANSYS as a FE software with nonlinear analysis. BEAM23 elements are used to model the frame



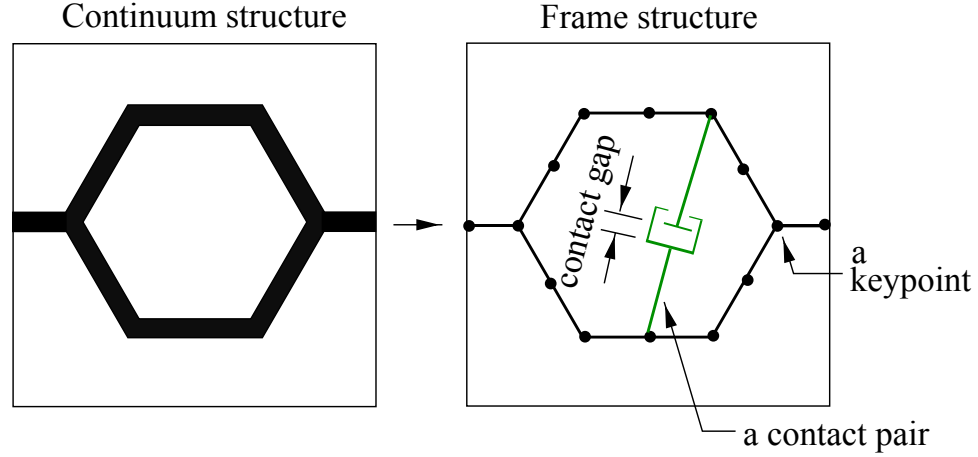


**Figure 6.6.** Conversion of continuum model into a frame structure

structure and CONTA172 along with TARGE169 elements are used for the contact pair. The boundary conditions and loads are the same as given in Figure 6.4.

### 6.3.2 Optimization Problem

Contact mechanisms that provide stress relief are investigated in this work. Because of stress relief, the maximum stress in the contact-aided cellular mechanisms is lower than that in the corresponding cellular structures without contact. To maximize stress relief, the normalized difference between the maximum stress in a contact-aided cell ( $\sigma_{\max}^{CA}$ ) and that in the corresponding non-contact cell ( $\sigma_{\max}^{NC}$ ) is considered as an objective function. An integer variable ( $y_j$ ) represents the existence of a contact pair between two prescribed keypoints: 1 indicating presence, 0 indicating absence. For each contact pair, there is a continuous variable that represents its initial contact gap ( $\gamma_j$ ). This contact gap is normalized by the total change in distance between the corresponding keypoints ( $\delta_j$ ) observed in the deformation of the non-contact structures and is given by

$$\rho_j = 1 - \frac{\gamma_j}{\delta_j}$$

When  $\rho_j$  is close to 0, the contact surfaces barely contact each other even after the cellular mechanism is fully deformed and, when  $\rho_j$  is close to 1, the contact surfaces are in contact during the entire deformation process.

Contact mechanisms that overlap each other or the base cellular structure may not be manufacturable and, therefore, are not considered here. The optimization problem can then be represented as the following.

$$\begin{aligned}
\min \quad & \frac{\sigma_{\max}^{CA} - \sigma_{\max}^{NC}}{\sigma_{\max}^{NC}} \\
\text{s.t. :} \quad & \text{no overlapping members} \\
& 0 \leq \rho_j \leq 1 \\
& y_j \in [0, 1], \text{ where } j = 1, 2, \dots, \mathbf{C}_2^{n_k}
\end{aligned} \tag{6.21}$$

where  $y_j$  is an integer variable, which is 1 if contact is present for  $j$ -th contact pair and 0 otherwise. Evidently, the optimization problem in Eqn. 6.21 is mixed-integer, nonlinear, non-differentiable, and non-convex. A gradient-based optimizer is not possible to implement and stochastic schemes are needed here. Since every feasible design is not necessarily related to another, finding the best design only using an evolutionary strategy requires many random initial guesses and is not likely to be effective in finding stress-relieving designs. To obtain the global optimum of the problem, an exhaustive yet systematic approach is implemented as described in the following.

### 6.3.3 Investigation of Stress Relieving Designs

The implementation of the non-overlapping constraint is described in Appendix B. Although the non-overlapping constraint reduces the problem size by several orders of magnitude, investigating all such feasible designs for stress relief using finite element analysis is still very cumbersome. As mentioned earlier, evolutionary or genetic algorithms are not guaranteed to yield a solution for every random initial guess. An exhaustive scheme is therefore presented.

Initially, non-overlapping designs having only one contact pair are considered. The sensitivity of the initial normalized contact gap ( $\rho$ ) to the maximum stress is different for each contact pair. Therefore, the initial contact gap is increased,

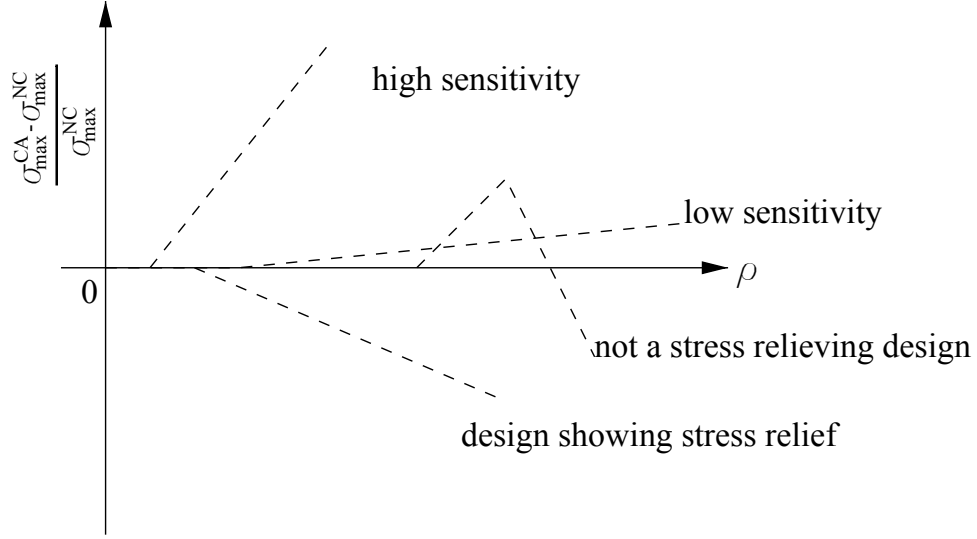


**Figure 6.7.** Schematic showing the effect of sensitivity of initial contact gap to the maximum stress in a contact-aided mechanism

keeping the applied displacement the same until a significant change ( $\pm 1\%$ ) in the maximum stress is observed. The corresponding values of the contact gaps are recorded. Since the applied displacement is the same for contact-aided mechanisms and the corresponding non-contact structures, stress-relieving designs must demonstrate a reduction in the maximum stress for the lowest possible initial contact gap. All such designs are recorded. This concept of the sensitivity of the maximum stress to contact gap is shown in Figure 6.7. A normalized difference between the maximum stress of a contact-aided cellular mechanism ( $\sigma_{\max}^{\text{CA}}$ ) and that of the corresponding non-contact structure ( $\sigma_{\max}^{\text{NC}}$ ) is schematically shown for different cases in this figure. Such a normalized measure must be less than 0 for minimum possible contact gap ( $\rho$ ) for a stress relieving mechanism – characterized by a negative sensitivity. A mechanism demonstrating a positive sensitivity for the lowest possible contact gap is not considered as a stress relieving design.

Non-overlapping designs with two contact pairs are considered next. The initial contact gaps found for single contact pairs are used here. For example, the design with contact pairs at the  $k$ -th and  $l$ -th locations uses the initial contact pairs obtained from the sensitivity analyses for a design having a single contact pair at the  $k$ -th location and another at the  $l$ -th location individually. If a design

exhibits stress relief, then its subset containing fewer contact pairs is considered for comparison. Using the preceding example, if a design with two contact pairs shows stress relief, the individual designs with a single contact pair at the  $k$ -th location and another at the  $l$ -th location are compared. If any design with a single contact pair exhibits more stress relief, then the additional contact pairs are not evidently needed. Such a design is discarded. Those two contact pair designs for which subset single pair designs either do not provide stress relief or provide less stress relief are added to the list of stress relieving designs.

The preceding process can be repeated inductively for larger numbers of contact pairs. In the present work, designs having up to four contact pairs are considered.

### 6.3.4 Differential Evolution

Once a contact mechanism is found, the contact gaps that yield maximum stress relief can now be found using differential evolution. Differential evolution (DE) is a heuristic approach to solve non-linear, non-differentiable, but continuous functions [107]. Since the maximum stress in the cellular structure changes continuously with contact gaps, DE can be implemented. A DE strategy also eliminates the sensitivity analysis needed for a gradient-based optimizer. A parameter vector ( $\rho$ ) consists of the non-dimensional contact gaps. The size of such a vector is, therefore, equal to the number of contact pairs (CP) present in the mechanism. The parameter vector at a generation  $G$  is given by

$$\rho_{ji,G} \text{ where, } i = 1, 2, \dots, \text{NP and } j = 1, 2, \dots, \text{CP}$$

where NP is the population size. Initially the parameter vector is populated with random numbers from 0 to 1. For every generation, a new generation ( $v$ ) is created from by adding a weighted difference between two mutually different parameters vectors into another vector. This process is termed ‘mutation’ and is mathematically represented as

$$v_{ji,G+1} = \rho_{jr1,G} + F \cdot (\rho_{jr2,G} - \rho_{jr3,G}) \quad (6.22)$$

where  $r_1$ ,  $r_2$ , and  $r_3$  indices are mutually different and  $\in \{1, 2, \dots, NP\}$ .  $F$  is a positive weighting factor,  $\in [0, 2]$ . A ‘crossover’ operation is introduced to increase the diversity in the population. The parameter vector after crossover ( $u$ ) is formed using the following process

$$u_{ji,G+1} = \begin{cases} v_{ji,G+1} & \text{if } randb(j) \leq CR \text{ or } j = rnbr(i) \\ \rho_{ji,G} & \text{if } randb(j) > CR \text{ and } j \neq rnbr(i) \end{cases} \quad (6.23)$$

where CR is the crossover probability,  $randb(j)$  is a random number  $\in [0, 1]$ , and  $rnbr(j)$  is a randomly chosen index  $\in \{1, 2, \dots, CP\}$ . A greedy criterion is used in the selection process, and it is given as follows

$$\rho_{ji,G+1} = \begin{cases} u_{ji,G+1} & \text{if } \sigma_{\max}^{CA}(u_{ji,G+1}) \leq \sigma_{\max}^{CA}(\rho_{ji,G}) \\ \rho_{ji,G} & \text{if } \sigma_{\max}^{CA}(u_{ji,G+1}) > \sigma_{\max}^{CA}(\rho_{ji,G}) \end{cases} \quad (6.24)$$

The preceding description is the basic structure of DE. Other variants are explained in [107]. In the present work, basic DE with random dither in every generation is implemented.  $F$  and CR are kept at 0.9 and 0.99, respectively. Also  $NP = 20 \times CP$ . The termination criterion is the maximum difference in the root mean square value of the generation  $G + 1$  and that of generation  $G$ . Convergence is assumed when such value is less than 5%.

## 6.4 Results

This section presents some cell topologies obtained for non-contact cellular structures and contact-aided cellular mechanisms. Homogenization coefficients, magnification ratio, and volume fraction are varied to obtain different topologies for non-contact cellular structures. Every such non-contact topology is further processed to find contact mechanisms that provide stress relief.

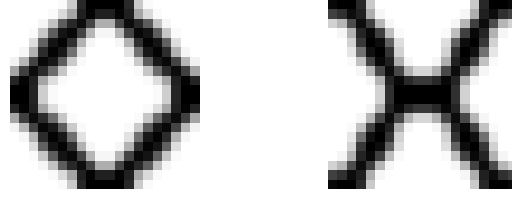


**Figure 6.8.** Unit cell topologies similar to honeycombs

### 6.4.1 Honeycomb-Similar Cell

The desired elastic properties of the structure are given as follows:

$$\begin{bmatrix} C_{11} & C_{12} & 0 \\ C_{21} & C_{22} & 0 \\ 0 & 0 & C_{33} \end{bmatrix} = \begin{bmatrix} 30 & 20 & 0 \\ 20 & 30 & 0 \\ 0 & 0 & 10 \end{bmatrix} \quad (6.25)$$

These properties were established using linear cellular material theory of honeycombs with a cellular angle of  $37^\circ$  [4]. The modulus of elasticity ( $E$ ) and Poisson's ratio ( $\nu$ ) for the base material were assumed to be 100 and 0.3, respectively. The target magnification ratio ( $M$ ) was 2.50. For a volume fraction ( $f$ ) of 0.35, the resulting topologies are shown in Figure 6.8. These topologies are similar to honeycombs. The cellular angles in these resulting topologies are also very close to the expected value ( $37^\circ$ ). The seemingly different topologies are a result of different randomized initial guesses. These topologies are essentially different ways to represent the same unit cell. A cellular structure formed by arranging such topologies in a periodic fashion is shown in Figure 6.9, which confirms that the different unit cells yield the same cellular pattern.

Notably, if the strain constraint is removed, satisfactory results are not found unless the volume fraction was increased to 0.65. One such topology is shown in Figure 6.10. The strain magnification ratio for this topology is 0.81 – significantly lower than the topologies found with the strain constraint. This indicates the importance of a strain constraint while designing cellular structures for high strain applications.

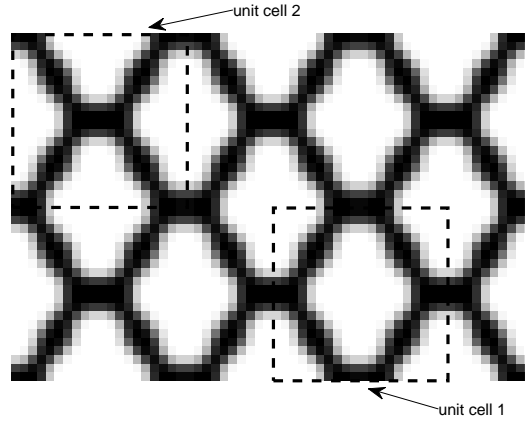


**Figure 6.9.** Cellular structure formed by different unit cells

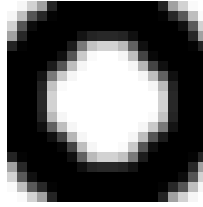


**Figure 6.10.** Honeycomb similar unit cell without the local strain constraint

The continuum model from Figure 6.8, left, is selected for further design. Fourteen total keypoints are chosen and connected using frame elements as shown in Figure 6.11. The in-plane thickness of the frame elements is selected to match the magnification ratio from continuum analysis. Such a frame model has  $\mathbf{C}_2^{14} = 91$  possible single contact pairs and a total of  $(2^{91} - 1)$  possible designs for contact mechanisms. The non-overlapping constraint is utilized to reduce the number of feasible designs to 35,657,727.

Two stress-relieving mechanisms are found using the exhaustive search method and are schematically shown in Figure 6.12. DE is employed further to maximize stress relief. The optimal non-dimensional contact gap for the contact-aided cellular mechanism shown in Figure 6.12, left, is 0.24, and the magnification ratio increases to 2.58 – about a 3% increase from the non-contact cellular structure. All the optimal non-dimensional contact gaps for the cell shown in Figure 6.12, right,

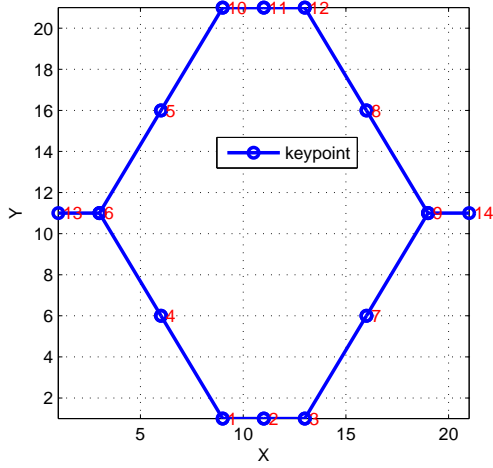


**Figure 6.11.** Frame structure for honeycomb similar cell

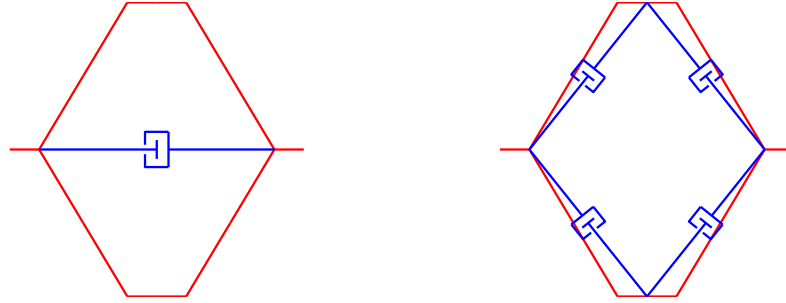


**Figure 6.12.** Stress relieving contact mechanisms for honeycomb similar cell with arbitrary contact gaps

are 0.62 and the magnification ratio increases to 2.80 – about a 12% increase from the non-contact cellular structure. The cellular configurations formed using these mechanisms are shown in Figure 6.13. Notably, some cells in the contact-aided cellular configuration do not possess a contact mechanism because of the nature of the unit cell. The non-contact cellular structures, therefore, have higher symmetry than the contact-aided cellular mechanisms.



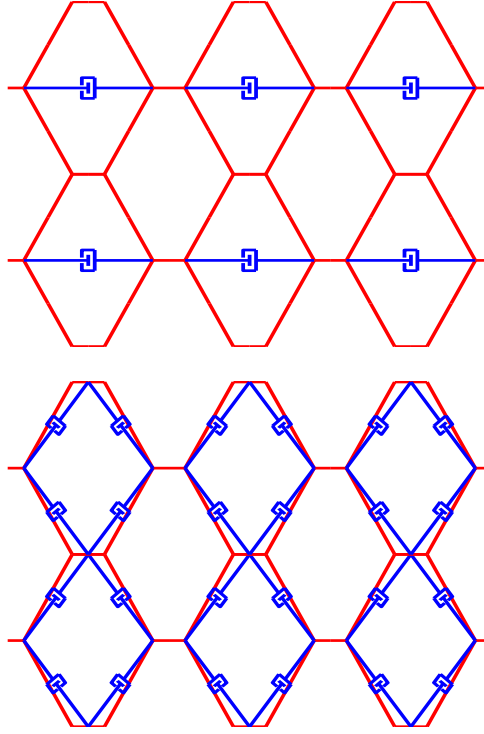


**Figure 6.13.** Cellular structure formed using the contact-aided cellular mechanisms for honeycomb-similar unit cells

### 6.4.2 Auxetic Cell

Another design is based on the following effective elastic properties of the structure. These properties depict a negative Poisson's ratio material, since the cross-diagonal terms in the effective elastic parameters ( $C_{12}$ ) are negative. Such a material would also be stiffer in the 2-direction than the 1-direction.

$$\begin{bmatrix} C_{11} & C_{12} & 0 \\ C_{21} & C_{22} & 0 \\ 0 & 0 & C_{33} \end{bmatrix} = \begin{bmatrix} 1.44 & -2.25 & 0 \\ -2.25 & 7.96 & 0 \\ 0 & 0 & 0.37 \end{bmatrix} \quad (6.26)$$

All the other parameters are same as those of the previous example. The unit cell topologies are shown in Figure 6.14. These topologies are similar to that of an auxetic cell, which exhibits a negative effective Poisson's ratio. The cellular structure formed using such unit cells is shown in Figure 6.15.

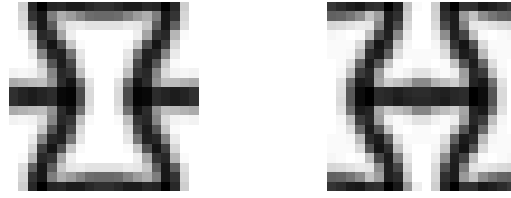


**Figure 6.14.** Unit cell topologies for negative effective Poisson's ratio

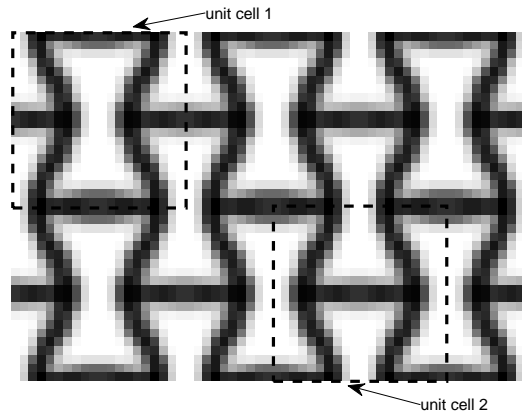


**Figure 6.15.** Cellular structure formed by auxetic unit cells

The non-contact continuum model from Figure 6.14 (left) is converted into a frame model using 14 keypoints as shown in Figure 6.16. Application of the non-overlapping constraint followed by stress relief investigation leads to 27 different designs exhibiting stress relief. In this work only symmetric designs are pursued because of the periodic nature of the desired structures. DE is employed on such symmetric designs to maximize the stress relief. The final set of three contact-aided unit cells is shown in Figure 6.17. The optimal non-dimensional contact gaps are 0.18, 0.99, and 0.44 (all contact pairs), respectively, from left to right. The magnification ratios increase to 2.78, 3.25, and 3.1, respectively – corresponding to 10.9%, 29.6%, and 24.1% increases from structures without any contact mechanism. The cellular configurations resulting from the unit cells are shown in Figure 6.18.

Although the present work limits the maximum number of contact pairs to four, it is interesting to note some designs having five contact pairs. Such designs are shown in Fig 6.19. These designs, being hybrids of those shown in Figure 6.17,

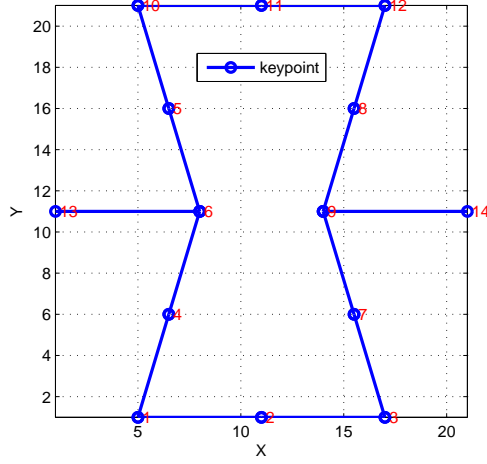


**Figure 6.16.** Frame structure for an auxetic cell

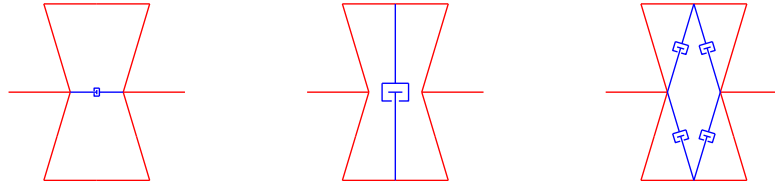


**Figure 6.17.** Stress relieving contact mechanisms for auxetic cell with arbitrary contact gaps

provide additional stress relief. The mechanism on left increases the magnification ratio by about 28%, while the one on right improves the ratio by about 36%.

### 6.4.3 Diamond Cell

Another non-contact unit cell and its effective material properties are shown in Figure 6.20 along with the cellular configuration. The resulting cellular structure has relatively low shear modulus (because of small  $C_{33}$ ) and is represented by a diamond-shaped unit cell connected by octagonal cells. The frame model is formed using 12 keypoints as shown in Figure 6.21. The non-overlapping constraint and the stress-relieving methodology yields one contact-aided cellular topology. Such a contact-aided unit cell and its cellular configuration is presented in Figure 6.21.

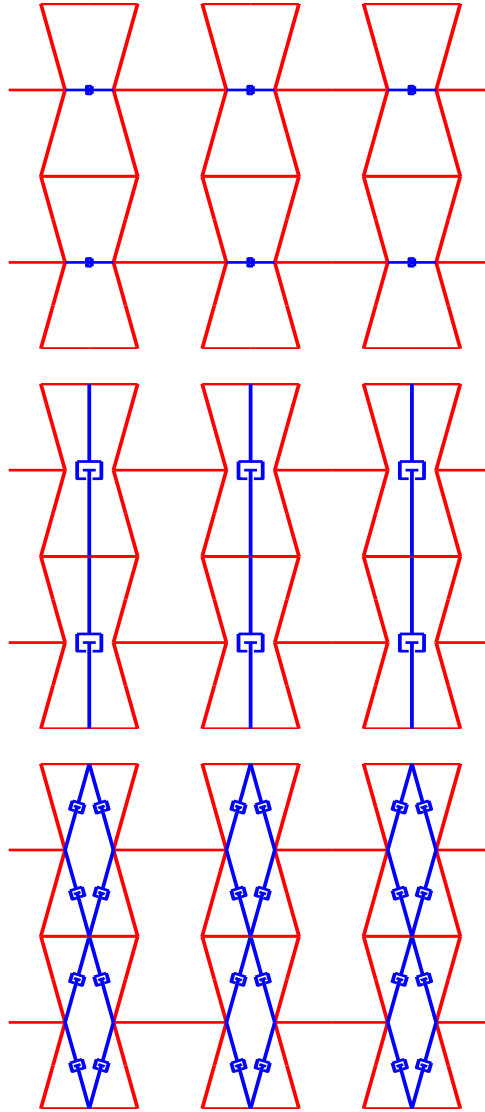


**Figure 6.18.** Cellular structure formed using the contact-aided cellular mechanisms for auxetic unit cells

The DE maximizes the stress relief, increasing the magnification ratio to 2.04 – about a 16.5% increase from the non-contact structure. The required initial non-dimensional contact gap is 0.46.

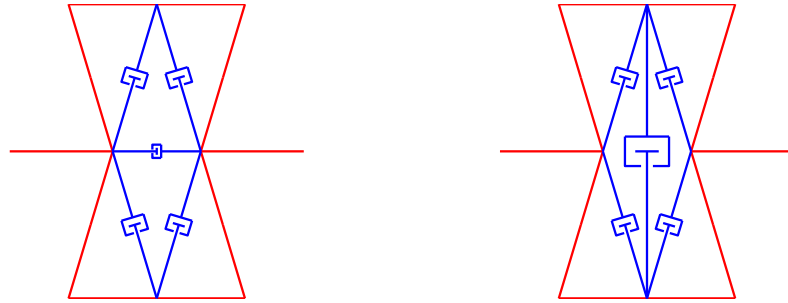


**Figure 6.19.** Stress relieving contact mechanisms with five contact pairs for auxetic cell

$$C_{11} = 3.50$$

$$C_{12} = 4.00$$

$$C_{22} = 5.00$$

$$C_{33} = 0.25$$

$$M = 1.75$$

$$E = 100$$

$$\nu = 0.3$$

$$f = 0.25$$

$$N_x = 30$$

$$N_y = 30$$

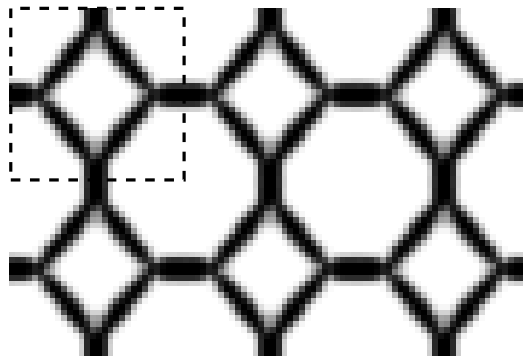
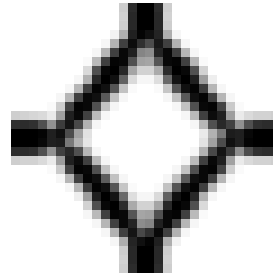


**Figure 6.20.** A diamond shaped unit cell along with the unit cell and the effective properties

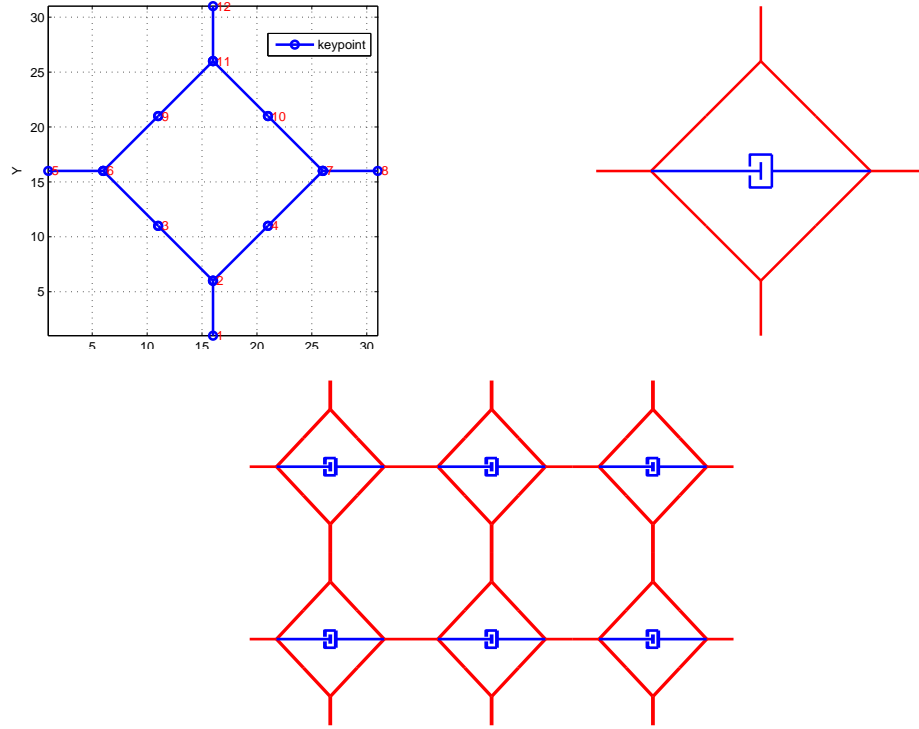


**Figure 6.21.** Frame structure, contact-aided unit cell, and contact-aided cellular configuration for the diamond-shaped unit cell

#### 6.4.4 Doubly Auxetic Cell

Another non-contact unit cell along with its properties and the corresponding cellular configuration is shown in Figure 6.22. Such a structure exhibits a negative Poisson's ratio, but its stiffness in both the 1-direction and 2-direction are similar. It also has a relatively low shear modulus. The frame model is formed using 20 key-points as shown in Figure 6.23. Such a frame model has 190 potential single contact pairs or  $(2^{190} - 1)$  total possible contact mechanism designs. Because of the large problem size, it takes hundreds of hours just to enforce the non-overlapping constraint.

To reduce the problem size, only symmetric designs are considered for this unit cell. Designs consisting of either one contact pair or two pairs are considered without any symmetry constraint. Designs with four contact pairs are obtained by reflecting the designs with two contact pairs. Both horizontal and vertical axes of

$$\begin{aligned}
C_{11} &= 1.10 \\
C_{12} &= -0. \\
C_{22} &= 1.7 \\
C_{33} &= 0.00
\end{aligned}$$

$$\begin{aligned}
M &= 2.0 \\
E &= 10 \\
\nu &= 0. \\
f &= 0.2 \\
N_x &= 30 \\
N_y &= 30
\end{aligned}$$

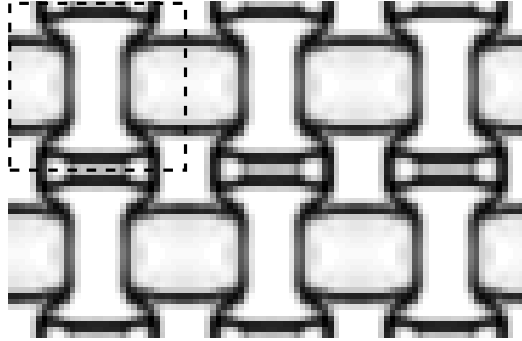
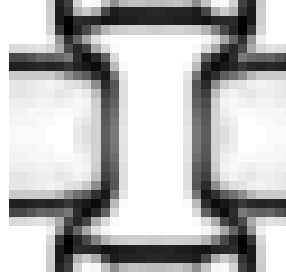


**Figure 6.22.** Another cellular structure with negative Poisson's ratio

symmetry are considered for the reflection. In the reflection process, if any of the contact pairs lie on the symmetry axis, then the resulting topology has three contact pairs. In general, other designs with three contact pairs are neglected. The previously described methodology is employed to obtain stress-relieving designs for such a symmetric subset. The designs are shown in Fig 6.24. The magnification ratio increases to 2.05 and 2.07 respectively – corresponding to an increase of only 2.35% and 3.66% as compared to the non-contact structures. The non-dimensional contact gaps for these designs are 0.19 and  $[0.15, 0.13]$ , respectively. The bi-symmetric versions of the preceding designs are presented in Figure 6.25. These designs, with greater numbers of contact pairs, do not provide additional stress relief.

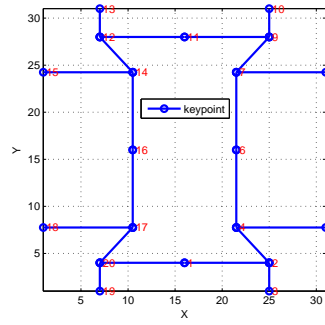


**Figure 6.23.** Frame structure for another unit cell with negative Poisson's ratio

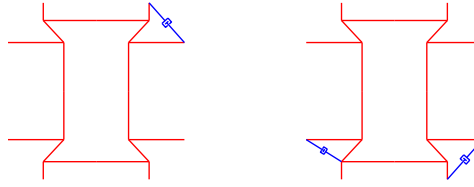


**Figure 6.24.** Stress relieving contact-aided unit cells

## 6.5 Summary

A strategy for the synthesis and design of contact-aided cellular mechanisms for high-strain applications is presented in this chapter. A two-step approach is implemented: a non-contact cellular structure is synthesized first using the inverse homogenization method along with a strain constraint. The maximum value of von Mises strain is determined using a norm approach. The Method of Moving Asymptotes (MMA) optimizer is employed for the non-contact topology optimization problem along with a hybrid filter consisting of Heaviside and modified Heaviside step functions.

The continuum non-contact cellular structure is converted to a frame mechanism in the second step in order to design a contact mechanism. A computationally efficient constraint is utilized to eliminate the overlapping designs and an exhaustive scheme is implemented to investigate the stress-relieving contact mechanisms. Results are presented for various effective material properties.



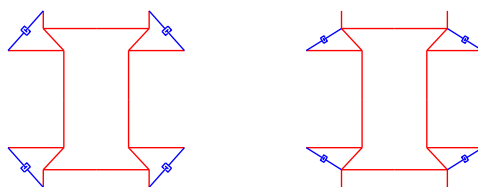


**Figure 6.25.** Stress relieving symmetric contact-aided unit cells

## Conclusions

This work focuses on developing lightweight compliant mechanisms for high strain and high strength applications. Cellular configurations and contact-aided compliant mechanisms are integrated to obtain such mechanisms. The analysis of one such cellular mechanism, its applications to morphing skin and meso-scaled structures, and finally a design methodology were described in the preceding chapters. This chapter summarizes the key findings and results. This chapter also describes the contributions made to the field as well as recommendations for future work.

### 7.1 Summary

Contact is used to redistribute loads and to provide stress relief in periodic compliant mechanisms. A theoretical formulation was developed to assist in understanding the effect of contact and to obtain preliminary but accurate results quickly. This model was founded on classical beam equations amended by correction factors to address large deflections and contact. This analytical model is compared with FE analysis and the errors in the prediction of maximum overall strain and the initial contact gap were less than 11% and 9%, respectively. Application of this concept using two different materials yields an improvement in the global strain capacity by more than 100% relative to cellular structures without contact.

Experiments conducted on aluminum models showed encouraging results, while validating the concept of stress relief and the simulation results. The analysis was further extended by optimizing the non-dimensional size for the proposed cellular

geometry to maximize the maximum overall strain, stress relief, and the required contact gap. The results indicate that an overall strain as high as 43 times the capability of the bulk material can be achieved using these mechanisms.

The analysis provides insights into the concept of stress relief while solidifying the idea of using cellular structures and contact-aided compliant mechanisms for high strain and high strength applications. Stress relief is obtained when the axial direct stress interacts with the bending stresses, thereby reducing the maximum tensile stresses. The failure stress for many alloys and ceramics in the compressive mode is significantly higher than that in tension. Stress relief is particularly useful for cellular structures fabricated using such materials to increase their effective strain. The size optimization illustrates a trade-off between the output performance and the manufacturing capabilities.

A case study focused on morphing skin was considered as an application of the high strain materials. In this application, the contact-aided compliant cellular structures performed better than the non-contact structures in terms of both the global strain and the structural mass. A methodology was proposed to design a cellular skin for a variable span morphing wing. An integer optimization problem was formulated and an ad-hoc algorithm was devised to tackle the problem. Results are presented for a small aircraft for both non-contact and the contact-aided cellular mechanisms. For a strain-hardening material, the local strain is lower than the allowable value. Contact stiffens the structure by putting cell walls into tension, which yields smaller transverse deflections for the same loading. Designs having smaller mass are thus possible. For a linearly elastic model, however, the stresses are high. Contact-induced stress relief can be used in such cases to make designs feasible. In all cases, the contact-aided cellular structure is a light-weight design and, therefore, a potential candidate for use as a morphing skin. Using contact-aided cellular mechanisms, the global strain capability is increased by as much as 37%. For a fixed global strain, the optimum contact-aided structure is 15% lighter than an optimum non-contact structure.

Another application, related to the design of meso-scaled mechanisms, is also considered. A novel manufacturing method, which can be used to fabricate millimeter-sized parts with micron-sized features, is utilized to fabricate the proposed cellular structure. The fabrication process imposes several

manufacturing constraints such as a maximum aspect ratio, a minimum contact gap, and a minimum wall thickness. The analytical model as well as the size optimization approach described earlier are employed and suitable designs are found to address the manufacturing conflicts. A fixture is developed to test the meso-scaled parts and to obtain their force-displacement relations.

The preceding two applications are only a few examples, but they illustrate the potential of the proposed cellular concept. Although the design approach for morphing skin is computationally expensive, it incorporated the out-of-plane aerodynamic loads as well as the constraints associated with the attachment of skin to the underlying actuators. The skin thickness resulted from this out-of-plane analysis proved to be a crucial factor in the determination of structural mass. Contact-aided cellular skin improves the performance of the morphing skin, while keeping the structure as light weight as possible. Meso-scaled compliant mechanisms can be fabricated using alloys, ceramics, or composites. All these bulk materials exhibit excellent strength. Utilizing the benefits of cellular configuration and contact-induced stress relief, their effective allowable strain is improved. Such mechanisms can be viewed as the macro structure of a high strength and high strain material. The approach to the reduction of local stresses in cellular structures merits continued investigation for other applications.

A strategy for the synthesis of contact-aided cellular mechanisms for high-strain applications is also presented. A two-step approach is implemented: a non-contact cellular structure is synthesized first using the inverse homogenization method along with a strain constraint. The maximum value of von-Mises strain is determined using a norm approach. The Method of Moving Asymptotes optimizer is employed for the non-contact topology optimization problem along with a hybrid filter consisting of Heaviside and modified Heaviside step functions. The continuum non-contact cellular structure is converted to a frame mechanism in the second step in order to design a contact mechanism. A computationally efficient constraint is utilized to eliminate the overlapping designs and an exhaustive scheme is implemented to investigate the stress relieving contact mechanisms.

Different resulting cellular topologies are presented in the work. Moderately high effective properties yield a topology that resembles a honeycomb cell. This topology offers two stress-relieving contact-aided cellular mechanisms: one with a

single contact pair, and the other with four contact pairs. The latter demonstrates more stress relief, corresponding to about a 12% higher strain magnification ratio than the structures without contact. A cellular structure with negative Poisson's ratio yields an auxetic cellular structure. Such a structure has 27 potential stress-relieving designs. One such design increases the magnification ratio by about 30%. In this case, cellular structures with more stress relief can also be obtained by forming hybrid designs incorporating larger numbers of contact pairs. Another cellular topology is obtained by enforcing low values of effective shear modulus. Adding an appropriate contact mechanism improves the magnification ratio by about 17%. Additional cellular structure is designed for negative Poisson's ratio but with relatively low shear modulus. The stress-relieving contact mechanism marginally improves the magnification ratio.

The final contact-aided cellular mechanism obtained through this process depends on several factors. The cellular structure without contact is governed by not only the homogenized coefficients, but also the desired magnification ratio, volume fraction, penalty factor. The strain constraint helps to obtain the cellular topologies at a lower volume fraction. Higher exponents result in more black and white designs and more accurate representation of local strain, but result in numerical instabilities. The design of contact mechanism relies on the number and location of keypoints chosen by a human designer for continuum-to-frame conversion. More keypoints represent the continuum non-contact structure more precisely. However, this exponentially increases the problem size. The choice of these different parameters is very important in the topology optimization process.

The methodology presented here is a fusion of a variety of techniques including ones developed in-house and those available in the literature. The results presented in this work are some examples of application of the proposed methodology. More cellular shapes can be obtained by assuming desired homogenized properties. Since contact is a very complex phenomenon, instead of traditional topology optimization procedures, an exhaustive yet practical scheme is introduced. Although high strain is the main objective of the suggested methodology, it could also be extended to other objective functions such as high thermal resistance, high bending stiffness, or high torsional stiffness.

## 7.2 Contributions

The present study contributes to the design of high strength and high strain cellular materials in the following ways.

- This work introduced a novel compliant mechanism integrating the benefits of the cellular configuration and the contact-aided compliant mechanisms. The contact mechanism was used to reduce the maximum failure-causing tensile stresses in the cellular structures, thereby enabling such structures to be stretched more than the corresponding structures without contact. The contact mechanism was also utilized as an additional load-carrying member and to increase transverse stiffness of the cellular structure.
- A planar analytical model comprising of contact-aided compliant mechanism was developed in this study. This analytical model can predict the stress relief and prescribe a suitable contact gap to obtain the maximum overall strain for a given geometry of cellular structure.
- A methodology was devised to design a cellular skin for a variable span morphing wing. The transverse aerodynamic loads were considered in the analysis and the concept of attaching the skin to underlying mechanism at a discrete number of points was introduced.
- Meso-scaled contact-aided cellular mechanisms using stainless steel and zirconia were developed. A custom fixture was also designed to test these components.
- A general topology optimization procedure was developed to synthesize contact-aided cellular mechanisms that provide stress relief. For illustration of the power of the approach, many cellular designs were developed. This procedure should be useful in many other applications where high strain is required.

### 7.3 Recommendations for Future Work

This study provides new avenues for further research in the related field. Some of these recommendations are described as follows:

- The work in this dissertation focused on cellular structures with sharp corners. Many manufacturing methods including meso-fabrication are not very suitable for structures with corners. Structures with corners are susceptible to thermal cracks while drying and sintering. Cellular designs with either fillets or curved walls are preferred. Although some cellular structures in the literature have curved walls (e.g., chiral [6]), utilizing contact in such structures can increase the load carrying capacity. Further investigation regarding cellular contact-aided compliant curved mechanisms is needed.
- The analytical model developed for a proposed cellular structure assumes that the wall thicknesses are very small compared to their lengths. This assumption allowed shear strains to be neglected. Meso-fabrication constrains the aspect ratio and the minimum possible wall thickness. For a thicker wall, the shear contributions may not be neglected and a further modifications are needed in the analytical model.
- The topology optimization, required to maximize the stress relief in the cellular structures, consists of a two-stage process. Stress relief is the difference between the maximum stress in the contact-aided compliant mechanism and that in the corresponding non-contact cellular structure. The knowledge of the non-contact cellular structure is essential for determining the stress relief. This is very similar to a bi-level programming problem [108], where the “leader” problem would be the design of non-contact cellular structures and the “follower” problem would be the synthesis of the contact-aided compliant mechanisms around the non-contact cellular structure. Methods tackling the hierarchical optimization problems can be employed here to address the topology optimization problem. Many such methods are based on genetic algorithms or simulated annealing [108]. The present problem is computationally cumbersome due to finite element analysis, and it may not be suitable for such methods; however, further attention is needed to explore the pos-

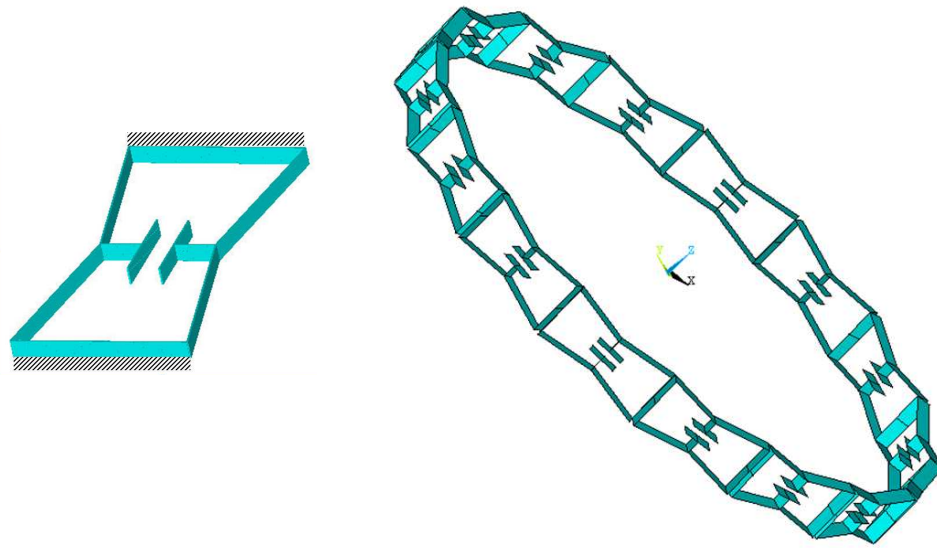


**Figure 7.1.** A contact-aided unit cell (left) for thermal shock resistance and schematic representation of a nozzle using such unit cells

sibility of using hierarchical solution methods for the topology optimization and find a solution using a single stage.

- The objective function for topology optimization was maximization of stress relief. One could use other objective functions to explore the benefits of contact in other applications, e.g., to maximize thermal shock resistance, to maximize shear strength, to maximize transverse stiffening. When a constrained material is heated, thermal stresses are developed. If these stresses are above the allowable value for that material, then cracking or spalling occurs. A conceptual design of a cellular structure to be used for improving the thermal shock resistance is shown in Figure 7.1 along with a structural application (a circular nozzle). Contact occurs when such a structure is heated, which allows the redistribution of thermal stresses in the cellular mechanism. Because of this redistribution, it can be heated more – increasing the thermal shock resistance.
- The design of morphing skin was limited to only a few discrete designs. This is due to high computational cost associated with the modeling of an entire wing in ANSYS. Such analysis was required to estimate the transverse de-



flections under the aerodynamic loads. An analytical model that can predict the transverse deflection for a uniform loading can make the design of morphing skin more efficient. There is an extensive literature for determining the effective flexural stiffness of sandwich plates (e.g., [109]). These studies either assume a very flexible cellular core (so that their contribution to the flexural stiffness is minimal) or consider only a regularly shaped honeycomb core (i.e. isotropic effective properties). The cellular structures required for high strain applications have shapes other than regular honeycombs. An initial study was done regarding such a model. Small deflection theory for orthotropic plates [94] has the following flexural stiffness in the X-direction ( $D_x$ )

$$D_x = \frac{E_x}{1 - \nu_x \nu_y} \quad (7.1)$$

where  $E_x$ ,  $\nu_x$ , and  $\nu_y$  are the modulus of elasticity in X-direction, Poisson's ratio in X-direction, and Poisson's ratio in Y-direction, respectively. Expressions for other components of flexural stiffness can be written as well. Linear cellular theory without shear contribution [4] or with shear [7] claims  $\nu_x \nu_y \approx 1.0$ . This creates a near-singularity in the model. The results obtained using such a model, therefore, are inconsistent with those from the numerical model. A modified analytical model for determining the deflections of cellular plates is needed.

## Sensitivity Analysis for Inverse Homogenization

One needs to calculate the sensitivities of the strain energy to derive the sensitivities for the homogenized coefficients. The strain energy for a given boundary conditions ( $E$ ) is given as

$$E = \sum_{e=1}^N x_e^p u^T k u$$

where  $k$  is the element stiffness matrix. For the displacement based loading the sensitivities can be given as [70]

$$\frac{dE}{dx_e} = p x_e^{p-1} u^T k u$$

The sensitivities for the maximum local strain are found using the adjoint method [102]. The general expression for the modified maximum local strain is as follows.

$$\epsilon_{\max}^{local} = \left[ \sum_{e=1}^N \left( x_e^{p/2} \sqrt{u^T M u} \right)^q \right]^{1/q}$$

The partial differentiation of the preceding term with respect an element density, after simplification, yields

$$\frac{\partial \epsilon_{\max}^{local}}{\partial x_e} = \frac{p}{2} \left[ \sum_{e=1}^N \left( x_e^{p/2} \sqrt{u^T M u} \right)^q \right]^{1/q-1} x_e^{pq-1} \sqrt{u^T M u} \quad (\text{A.1})$$

The adjoint equation is

$$K\lambda = \frac{\partial \epsilon_{\max}^{local}}{\partial u}^T$$

$$= \left\{ \left[ \sum_{e=1}^N \left( x_e^{p/2} \sqrt{u^T M u} \right)^q \right]^{1/q-1} \frac{\left( x_e^{p/2} \sqrt{u^T M u} \right)^{q-1}}{\sqrt{u^T M u}} x_e^{p/2} M u \right\}^T$$

where  $\lambda$  is the adjoint displacement. The loading conditions are not function of the element densities. The sensitivity of the maximum local strain is, therefore,

$$\frac{d\epsilon_{\max}^{local}}{dx_e} = \frac{\partial \epsilon_{\max}^{local}}{\partial x_e} - \lambda_e^T k u \quad (\text{A.2})$$

where  $\lambda_e$  is the vector of nodal adjoint displacements for element  $e$ .

## Non-Overlapping Constraint

The non-overlapping constraint is independent of the objective function in Eqn. 6.21 and the corresponding continuous variables ( $\rho_j$ 's). Enforcing this constraint reduces the problem size substantially.

The equations of lines representing the members of the frame cellular structure are obtained. Two members overlap each when the point of intersection of their governing lines lies on either of the members between their endpoints. This approach can be used for all the possible  $2^{\mathbf{C}_2^{n_k}} - 1$  designs to investigate the non-overlapping members. However, this approach is computationally very costly. An efficient strategy is implemented in this work. It involves formulating a compatibility matrix ( $A$ ) of size  $\mathbf{C}_2^{n_k} \times \mathbf{C}_2^{n_k}$ . If each keypoint are connected to every another, the total number of contact pairs are  $\mathbf{C}_2^{n_k}$ . These contact pairs are numbered from 1 through  $\mathbf{C}_2^{n_k}$ . Assuming  $k$  and  $l$  are the numbers of two arbitrarily chosen contact pairs,

$$A_{kl} = \begin{cases} 1, & \text{if } k\text{-th pair does not overlap with } l\text{-th pair} \\ 0, & \text{otherwise} \end{cases} \quad (\text{B.1})$$

where  $A_{kl}$  is an element of the compatibility matrix, located at  $k$ -th row and  $l$ -th column. A diagonal element ( $A_{kk}$ ) is 1 only if  $k$ -th pair can exist without overlapping the base non-contact cellular structure.

For bookkeeping, any contact-aided design ( $b$ ) is represented by a  $\mathbf{C}_2^{n_k}$  long binary string, where 1 at  $k$ -th location stands for the presence of  $k$ -th contact pair

in the design and 0 otherwise. With this nomenclature, the following algorithm is used to determine all the non-overlapping designs using a compatibility matrix ( $A$ ).

```

recursive function nonoverlap( $A, b, k$ )
if  $k = \mathbf{C}_2^{n_k}$  then
    store  $b$  as a non-overlapping design
else
    if  $b_k = 1$  then
         $b^{new_1} \leftarrow b$ 
         $b_k^{new_1} = 0$ 
        call nonoverlap( $A, b^{new_1}, k + 1$ )
         $b_k^{new_2} = b \cdot A_k$ ,
        call nonoverlap( $A, b^{new_2}, k + 1$ )
    else
        call nonoverlap( $A, b, k + 1$ )
    end if
end if

```

where  $b_k$  and  $b_k^{new_1}$  represents  $k$ -th element of the designs  $b$  and  $b^{new_1}$  respectively.  $A_k$ , stands for the  $k$ -th row of  $A$  and  $\cdot$  represents an element-wise multiplication. The function **nonoverlap** is initially called with  $A, b = [1, \ 1, \ \dots \ 1]$  and  $k = 1$  as the input arguments. The function recursively finds all the non-overlapping designs. Since only  $\mathbf{C}_2^{n_k} \times \mathbf{C}_2^{n_k}$  matrix inverse calculations are needed in this approach, the overall computation time is relatively very small.

# Bibliography

- [1] ASHBY, M. F. (2005) *Materials Selection in Mechanical Design*, 3 ed., Elsevier Butterworth-Heinemann, Boston, MA.
- [2] HENRY, C. and G. MCKNIGHT (2006) “Cellular Variable Stiffness Materials for Ultra-Large Reversible Deformations in Reconfigurable Structures,” in *Smart Structures and Materials 2006: Active Materials: Behavior and Mechanics*, Proceedings of SPIE 6170, pp. 1–12.
- [3] KORNBLUH, R., H. PRAHLAD, and R. PELRINE (2004) “Rubber to Rigid, Clamped to Unclamped: Towards Composite Materials with Wide Range of Controllable Stiffness and Damping,” in *Smart Structures and Materials 2004: Industrial and Commercial Applications of Smart Structures Technologies*, Proceedings of SPIE Vol. 5388, Bellingham, WA, pp. 372–386.
- [4] GIBSON, L. J. and M. F. ASHBY (1997) *Cellular Solids - Structure and Properties*, 2 ed., Cambridge University Press, Cambridge, UK.
- [5] MEHTA, V., M. FRECKER, and G. A. LESIEUTRE (2009) “Stress Relief in Contact-aided Compliant Cellular Mechanisms,” *ASME Journal of Mechanical Design*, **31**(9), pp. 1–11.
- [6] BORNENGO, D., F. SCARPA, and C. REMILLAT (2005) “Evaluation of Hexagonal Chiral Structure for Morphing Airfoil Concept,” *Proceedings of Institute of Mechanical Engineering, Part G: Journal of Aerospace Engineering*, **219**(3), pp. 185–192.
- [7] OLYMPIO, K. R. and F. GANDHI (2009) “Flexible Skins for Morphing Aircraft using Cellular Honeycomb Cores,” *Journal of Intelligent Material Systems and Structures*, **0**, pp. 1–17.
- [8] GUERINOT, A. E., S. P. MAGLEBY, L. L. HOWELL, and R. H. TODD (2005) “Compliant Joint Design Principles for High Compressive Load Situations,” *ASME Journal of Mechanical Design*, **127**(4), pp. 774–781.

- [9] ROARK, R. J. and W. C. YOUNG (1975) *Formulas for Stress and Strain*, 5 ed., McGraw-Hill, New York.
- [10] BITZER, T. (1997) *Honeycomb Technology: Materials, Design, Manufacturing, Applications and Testing*, 1 ed., Chapman and Hall, London, UK.
- [11] CORPORATION, H., “<http://www.hexcel.com>,” Website.
- [12] DUPONT, “<http://www2.dupont.com>,” Website.
- [13] SHAW, J. A., D. S. GRUMMON, and J. FOLTZ (2007) “Superelastic NiTi Honeycombs: Fabrication and Experiments,” *Smart Materials and Structures*, **16**, pp. 170–178.
- [14] ZHEJIANG GKO DECORATION MATERIAL CO., L., “<http://www.gkozs.com/eabout.asp>,” Website.
- [15] PLANTEMA, F. J. (1966) *Sandwich Construction: The Bending and Buckling of Sandwich Beams, Plates and Shells*, Wiley, New York.
- [16] ALDERSON, A. and K. L. ALDERSON (2007) “Auxetic Materials,” *Journal of Aerospace Engineering: Part G*, **221**, pp. 565–575.
- [17] SCARPA, F. and G. TOMLINSON (1999) “Theoretical Characteristics of the Vibration of Sandwich Plates with In-plane Negative Poisson’s Ratio Values,” *Journal of Sound and Vibrations*, **230**(1), pp. 45–67.
- [18] SCARPA, F., P. PANAYIOTOU, and G. TOMLINSON (2000) “Numerical and Experimental Uniaxial Loading on In-plane Auxetic Honeycombs,” *Journal of Strain Analysis*, **35**(5), pp. 383–388.
- [19] LAKES, R. (1987) “Foam Structures with a Negative Poisson’s Ratio,” *Science*, **235**, pp. 1038–1040.
- [20] OLYMPIO, K. R. and F. GANDHI (2009) “Modeling and Numerical Analyses of Skin Design Concepts,” in *50th AIAA/ASME/ASCE/AHS/ASC Structures, Structural Dynamics, and Materials Conference*, AIAA 2009-2115, Palm Springs, CA.
- [21] LARSEN, U. D., O. SIGMUND, and S. BOUWSTRA (1997) “Design and Fabrication of Compliant Micromechanisms and Structures with Negative Poisson’s Ratio,” *Journal of MicroElectroMechanical Systems*, **6**(2), pp. 99–106.
- [22] OLYMPIO, K. R. and F. GANDHI (2009) “Zero Poisson’s Ratio Cellular Honeycombs for Flex Skins Undergoing One Dimensional Morphing,” *Journal of Intelligent Material Systems and Structures*, **20**, pp. 1–17.

- [23] WANG, A. J. and D. L. MCDOWELL (2004) "In-Plane Stiffness and Yield Strength of Periodic Metal Honeycombs," *Journal Engineering Materials and Technology*, **126**, pp. 137–156.
- [24] JHA, A. K. and J. N. KUDVA (2004) "Morphing Aircraft Concepts, Classifications and Challenges," in *Smart Structures and Materials 2004: Industrial and Commercial Applications of Smart Structure Technologies*, Proceedings SPIE 5388, pp. 213–224.
- [25] JOSHI, S., Z. TIDWELL, W. A. CROSSLEY, and S. RAMKRISHNAN (2004) "Comparison of Morphing Wing Strategies Based upon Aircraft Performance Impacts," in *45th AIAA/ASME/ASCE/AHS/ASC Structures, Structural Dynamics & Materials Conference*, AIAA 2004-1722, Palm Springs, CA.
- [26] LESIEUTRE, G. A., J. A. BROWNE, and M. I. FRECKER (2006) "Scaling and Performance, Weight and Actuation of a 2-D Compliant Cellular Frame Structure for a Morphing Wing," in *17th International Conference on Adaptive Structures and Technologies*, Proceedings of ICAST2006, Taipei, Taiwan, pp. 1–8.
- [27] MURRAY, G., F. GANDHI, and C. BAKIS (2007) "Flexible Matrix Composite Skins for One Dimensional Wing Morphing," in *Proceedings of 48th AIAA/ASME/ASCE/AHS/ASC Structures, Structural Dynamics, and Materials Conference*, AIAA 2007-1737, Honolulu, Hawaii.
- [28] SAMUEL, J. B. and D. PINES (2007) "Design and Testing of Pneumatic Telescopic Wing for Unmanned Aerial Vehicles," *Journal of Aircraft*, **44**(4), pp. 1088–1099.
- [29] SANDERSON, T. (2007) "Analysis of Actuator Requirements for Micro UAV Telescopic Wings," in *Proceedings of IMECE, 2007 ASME International Mechanical Engineering Congress and Exposition*, vol. IMECE 2007- 43535, Seattle, Washington.
- [30] JOHNSON, T., M. FRECKER, M. ABDALLA, Z. GURDAL, and D. LINDNER (2009) "Nonlinear Analysis and Optimization of Diamond Cell Morphing Wings," *Journal of Intelligent Material Systems and Structures*, **20**(7), pp. 815–824.
- [31] CADOGAN, D., T. SMITH, F. UHELSKY, and M. MACKUSICK (2004) "Morphing Inflatable Wing Development for Compact Package Unmanned Aerial Vehicle," in *45th AIAA/ASME/ASCE/AHS/ASC Structures, Structural Dynamics & Materials Conference*, AIAA 2004-1807, Palm Springs, CA.



- [32] KOTA, S., J. HETRICK, and R. OSBORN (2003) "Design and Application of Compliant Mechanisms for Morphing Aircraft Structures," in *Smart Structures and Materials 2003: Industrial and Commercial Applications of Smart Structures Technologies* (E. H. Anderson, ed.), vol. 5054 of *Proceedings of SPIE*, pp. 24–33.
- [33] BOWMAN, J., B. SANDERS, B. CANNON, J. KUDVA, S. JOSHI, and T. WEISSHAAR (2007) "Development of Next Generation Morphing Aircraft Structures," in *Proceedings of 48th AIAA/ASME/ASCE/AHS/ASC Structures, Structural Dynamics, and Materials Conference*, AIAA 2007-1730, Honolulu, Hawaii.
- [34] RAMRAKHYANI, D. S., G. A. LESIEUTRE, M. I. FRECKER, and S. BHARTI (2005) "Aircraft Structural Morphing Using Tendon-Actuated Compliant Cellular Trusses," *Journal of Aircraft*, **42**(6), pp. 1615–1621.
- [35] (Visited Jan 30, 2008), "<http://www.nextgenaero.com/>," Website.
- [36] (Visited Jan 30, 2008), "<http://www.lockheedmartin.com/>," Website.
- [37] THILL, C., J. ETCHES, I. BOND, K. POTTER, and P. WEAVER (2008) "Morphing Skins," *The Aeronautical Journal*, **112**(1129), pp. 117–139.
- [38] MANZO, J., E. GARCIA, A. WICKENHEISER, and G. C. HORNER (2004) "Adaptive Structural Systems and Compliant Skin Technology for Morphing Aircraft Structures," in *Smart Structures and Materials 2004: Smart Structures and Integrated Systems* (A. B. Flatau, ed.), vol. 5390 of *Proc. SPIE*, pp. 225–234.
- [39] REED, J. L., C. D. HEMMELGARN, B. M. PELLE, and E. HAVENS (2005) "Adaptive Wing Structures," in *Smart Structures and Materials 2005: Industrial and Commercial Applications of Smart Structures Technologies* (E. V. White, ed.), vol. 5762 of *Proceedings of SPIE*, pp. 132–142.
- [40] MCKNIGHT, G. and C. HENRY (2005) "Variable Stiffness Materials for Reconfigurable Surface Applications," in *Smart Structures and Materials 2005: Active Materials: Behavior and Mechanics*, Proceedings of SPIE 5761, pp. 1–8.
- [41] MAUTE, K. and G. W. REICH (2006) "Integrated Multidisciplinary Topology Optimization Approach to Adaptive Wing Design," *Journal of Aircraft*, **43**(1), pp. 253–263.
- [42] REICH, G. W., B. SANDERS, and J. J. JOO (2007) "Development of Skins for Morphing Aircraft Applications via Topology Optimization," in *Proceedings of 48th AIAA/ASME/ASCE/AHS/ASC Structures, Structural Dynamics, and Materials Conference*, AIAA 2007-1738, Honolulu, Hawaii, pp. 1–13.

- [43] INOYAMA, D., B. P. SANDERS, and J. J. JOO (2007) "Topology Synthesis of Distributed Actuation Systems for Morphing Wing Structures," *Journal of Aircraft*, **44**(4), pp. 1205–1213.
- [44] YOKOZEKI, T., S. TAKEDA, T. OGASAWARA, and T. ISHIKAWA (2006) "Mechanical Properties of Corrugated Composites for Candidate Materials of Flexible Wing Structures," *Composites A: Applied Science and Manufacturing*, **37**, pp. 1578–1586.
- [45] CHRISTIAN and P. J. A. KENIS (2007) "Fabrication of Ceramic Microscale Structures," *Journal of American Ceramic Society*, **90**(9), pp. 2779–2983.
- [46] ZHANG, Z., B. LIU, and F. F. LANGE (2005) "Increasing Wet Green Strength of Alumina Body During Microfabrication by Colloidal Isopressing," *Journal of American Ceramic Society*, **88**(6), pp. 1411–1414.
- [47] HEULE, M. and L. J. GAUCKLER (2001) "Gas Sensors Fabricated from Ceramic Suspensions by Micromolding in Capillaries," *Advanced Materials*, **13**(23), pp. 1790–1793.
- [48] MAEDA, R., J. J. TSUAR, S. H. LEE, and M. ICHIKI (2004) "Piezoelectric Microactuator Devices," *Journal of Electroceramics*, **12**(1–2), pp. 89–100.
- [49] ANTOLINO, N. E., G. HAYES, R. KIRKPATRICK, C. L. MUHLSTEIN, M. I. FRECKER, E. MOCKENSTURM, and J. H. ADAIR (2009) "Lost Mold Rapid Infiltration Forming of Mesoscale Ceramics: Part 1, Fabrication," *Journal of American Ceramic Society*, **92**(s1), pp. S63–S69.
- [50] ANTOLINO, N. E., G. HAYES, R. KIRKPATRICK, C. L. MUHLSTEIN, M. I. FRECKER, E. MOCKENSTURM, and J. H. ADAIR (2009) "Lost Mold Rapid Infiltration Forming of Mesoscale Ceramics: Part 2, Geometry and Strength Improvement," *Journal of American Ceramic Society*, **92**(s1), pp. S70–S78.
- [51] LEWIS, J. A., J. E. SMAY, J. STUECKER, and J. CESARANO (2006) "Direct Ink Writing of Three-Dimensional Ceramic Structures," *Journal of the American Ceramic Society*, **89**(12), pp. 3599–3609.
- [52] TAY, B. Y., J. R. G. EVANS, and M. J. EDIRISINGHE (2003) "Solid Freeform Fabrication of Ceramics," *International Materials Reviews*, **48**(6), pp. 341–370.
- [53] HEULE, M., S. VUILLEMIN, and L. J. GAUCKLER (2003) "Powder-based ceramic meso- and microscale fabrication processes," *Advanced Materials*, **15**(15), pp. 1237–1245.

- [54] XIA, Y. N. and G. M. WHITESIDES (1998) “Soft Lithography,” *Annual Review of Materials Science*, **28**, pp. 153–184.
- [55] HEULE, M., U. P. SCHONHOLZER, and L. J. GAUCKLER (2004) “Patterning Colloidal Suspensions by Selective Wetting of Microcontact-Printed Surfaces,” *Journal of the European Ceramic Society*, **24**(9), pp. 2733–2739.
- [56] ZHAO, X. M., Y. N. XIA, and G. M. WHITESIDES (1996) “Fabrication of Three-Dimensional Micro-Structures: Microtransfer Molding,” *Advanced Materials*, **8**(10), p. 837.
- [57] LAWES, R. A. (2007) “Manufacturing Costs for Microsystems/MEMS Using High Aspect Ratio Microfabrication Techniques,” *Microsystem Technologies-Micro-and Nanosystems-Information Storage and Processing Systems*, **13**(1), pp. 85–95.
- [58] HONG, G., A. S. HOLMES, and M. E. HEATON (2004) “SU8 Resist Plasma Etching and Its Optimisation,” *Microsystem Technologies-Micro-and Nanosystems-Information Storage and Processing Systems*, **10**(5), pp. 357–359.
- [59] HEULE, M. and L. J. GAUCKLER (2001) “Microfabrication of Ceramics Based Colloidal Suspensions and Photoresist Masks,” *Journal of Photopolymer Science and Technology*, **14**(3), pp. 449 – 452.
- [60] AGUIRRE, M. E., G. HAYES, M. FRECKER, J. ADAIR, and N. ANTOLINO (2008) “Fabrication and Design of a Nanoparticulate Enabled Micro Forceps,” in *Proceedings of ASME IDETC/CIE*, pp. 1–10.
- [61] YUANGYAI, C., H. B. NEMBHARD, G. HAYES, N. ANTOLINO, and J. H. ADAIR (2009) “Yield Improvement for Lost Mold Rapid Infiltration Forming Process by a Multi-Stage Fractional Factorial Split Plot Design,” *International Journal of Nanomanufacturing*, **3**(4), pp. 351–367.
- [62] YUANGYAI, C., H. B. NEMBHARD, G. HAYES, and J. H. ADAIR (Submitted) “Robust Parameter Design for Multiple Stage Manufacturing,” *Journal of Quality Technology*.
- [63] HAWKINS, G., M. O’BRIEN, R. ZALDIVAR, and H. VONBREMEN (2002) “Machine Augmented Composites,” in *Smart Structures and Materials 2002: Industrial and Commercial Applications of Smart Structures Technologies*, vol. 4698 of *Proceedings of SPIE*, pp. 231–236.
- [64] CADDOCK, B. D. and K. E. EVANS (1989) “Microporous materials with negative Poisson’s ratios. I. Microstructure and mechanical properties,” *Journal of Physics D: Applied Physics*, **22**, pp. 1877–1882.

- [65] ALDERSON, A. and K. EVANS (1995) "Microstructural Modeling of Auxetic Microporous Polymers," *Journal of Materials Science*, **30**(13), pp. 3319–3332.
- [66] LEVY, O., S. KRYLOV, and I. GOLDFARB (2006) "Design Considerations for Negative Poisson's Ratio Structures under Large Deflections for MEMS Applications," *Smart Materials and Structures*, **15**, pp. 1459–1466.
- [67] MANKAME, N. D. and G. K. ANANTHASURESH (2004) "A Novel Compliant Mechanism for Converting Reciprocating Translation Into Enclosing Curved Paths," *ASME Journal of Mechanical Design*, **126**, pp. 667–672.
- [68] CANNON, J. R. and L. L. HOWELL (2005) "A Compliant Contact-Aided Revolute Joint," *Mechanism and Machine Theory*, **40**, pp. 1273–1293.
- [69] MANKAME, N. D. and G. K. ANANTHASURESH (2007) "Synthesis of Contact-Aided Compliant Mechanisms for Non-smooth Path Generation," *International Journal of Numerical Methods in Engineering*, **69**(12), pp. 2564–2605.
- [70] BENDSOE, M. P. and O. SIGMUND (2003) *Topology Optimization Theory, Methods and Applications*, Springer, Germany.
- [71] SIGMUND, O. (1997) "On Design of Compliant Mechanisms using Topology Optimization," *Mechanics of Structures and Machines*, **25**(4), pp. 493–524.
- [72] SWAN, C. C. and J. S. ARORA (1997) "Topology Design and Material Layout in Structured Composites of High Stiffness and Strength," *Structural Optimization*, **13**, pp. 45–59.
- [73] JOO, J. and S. KOTA (2004) "Topological Synthesis of Compliant Mechanisms using Nonlinear Beam Elements," *Mechanics Based Design of Structures and Machines*, **32**(1), pp. 17–38.
- [74] BOURGAT, J. F. (1977) "Numerical Experiments of the Homogenization Method for Operators with Periodic Coefficients," in *Lecture Notes in Mathematics*, Springer Verlag, Berlin, pp. 330–356.
- [75] GUEDES, J. M. and N. KIKUCHI (1990) "Preprocessing and Postprocessing for Materials based on the Homogenization Method with Adaptive Finite Element Methods," *Computer Methods in Applied Mechanical Engineering*, **83**, pp. 143–198.
- [76] SIGMUND, O. (1994) "Materials with Prescribed Constitutive Parameters: An Inverse Homogenization Problem," *International Journal of Solids and Structures*, **31**(17), pp. 2313–2329.

- [77] SIGMUND, O. (1995) "Tailoring Materials with Prescribed Elastic Properties," *Mechanics of Materials*, **20**, pp. 351–368.
- [78] SIGMUND, O. (2000) "A New Class of External Composites," *Journal of Mechanics and Physics of Solids*, **48**, pp. 397–428.
- [79] ZHANG, W. and S. SUN (2006) "Scale-Related Topology Optimization of Cellular Materials and Structures," *International Journal of Numerical Methods in Engineering*, **68**, pp. 993–1011.
- [80] QIU, K., W. ZHANG, M. DOMASZEWSKI, and D. CHAMORET (2009) "Topology Optimization of Periodic Cellular Solids Based on Superelement Method," *Engineering Optimization*, **41**(3), pp. 225–239.
- [81] OLYMPIO, K. R. and F. GANDHI (2010) "Skin Designs using Multi-Objective Topology Optimization," *Journal of Intelligent Material Systems and Structures*, (In print).
- [82] KLARBRING, A., J. PETERSSON, and M. RONNQVIST (1995) "Truss Topology Optimization involving Unilateral Contact," *Journal of Optimization Theory and Applications*, **87**(1), pp. 1–31.
- [83] WAN, H., H. OHTAKI, S. KOTOSAKA, and G. HU (2004) "A Study of Negative Poisson's ratios in Auxetic Honeycombs Based on a Large Deflection Model," *European Journal of Mechanics A/Solids*, **23**(1), pp. 95–106.
- [84] HOWELL, L. L. (2002) *Compliant Mechanisms*, John Wiley & Sons, Inc., New York, NY.
- [85] TIMOSHENKO, S. and J. GERE (1961) *Theory of Elastic Stability*, 2nd ed., McGraw Hill, New York.
- [86] BRICK, R. M., A. W. PENSE, and R. B. GORDON (1977) *Structure and Properties of Engineering Materials*, 4 ed., McGraw-Hil.
- [87] DEB, K., A. PRATAP, S. AGARWAL, and T. MEYARIVAN (2002) "A Fast and Elitist Multiobjective Genetic Algorithm: NSGA-II," *IEEE Transactions on Evolutionary Computation*, **6**(2), pp. 182–197.
- [88] DEB, K. and S. JAIN (2002) *Running Performance Metrics for Evolutionary Multi-Objective Optimization*, KanGAL 2002004, Indian Institute of Technology, Kanpur, India.
- [89] JOO, J. J., B. SANDERS, T. JOHNSON, and M. I. FRECKER (2006) "Optimal Actuator Location within a Morphing Wing Scissor Mechanism Configuration," in *Smart Structures and Materials 2006: Active Materials: Behavior and Mechanics* (D. K. Lindner, ed.), vol. 6166 of *Proc. of SPIE*, pp. 1–12.

- [90] JACOBS, E. N. (1934) *Airfoil Section Characteristics as Affected by Protuberances*, *Tech. Rep. 46*, NACA Report.
- [91] GANDHI, F. and P. ANUSONTI-INTHRA (2008) "Skin Design Studies for Variable Camber Morphing Airfoils," *Smart Materials and Structures*, **17**, pp. 1–8.
- [92] (Visited Jan 30, 2008), "<http://www.ansys.com>," Website.
- [93] (Visited Jan 30, 2008), "<http://www.materialdatacenter.com>," Website.
- [94] VENTSEL, E. and T. KRAUTHAMMER (2001) *Thin Plates and Shells: Theory, Analysis and Applications*, Marcel Dekker, Inc., New York, NY.
- [95] MATWEB, "<http://www.matweb.com>," Website.
- [96] AGUIRRE, M. E., G. HAYES, M. FRECKER, J. ADAIR, and N. ANTOLINO (2009) "Fabrication and Strength-Based Design of a Meso Forceps," in *Proceedings of ASME IDETC/CIE*, pp. 1–9.
- [97] QUINN, G. D., E. FULLER, D. XIANG, A. JILLAVENKATASA, L. MA, D. SMITH, and J. BEALL (2008) *A Novel Test Method for Measuring Mechanical Properties at the Small-Scale: The Theta Specimen*, vol. 26 of *Ceramic Engineering and Science Proceedings*, Wiley InterScience.
- [98] ZHANG, W., G. DAI, F. WANG, S. SUN, and H. BASSIR (2007) "Using Strain Energy based Prediction of Effective Elastic Properties in Topology Optimization of Material Microstructures," *Acta Mechanica Sin*, **23**, pp. 77–89.
- [99] DUYSINX, P. and M. P. BENDSOE (1998) "Topology Optimization of Continuum Structures with Local Stress Constraints," *International Journal of Numerical Methods in Engineering*, **43**(8), pp. 1453–1478.
- [100] YANG, R. J. and C. J. CHEN (1996) "Stress Based Topology Optimization," *Structural Optimization*, **12**, pp. 98–105.
- [101] DUYSINX, P. and O. SIGMUND (1998) "New Developments in Handling Stress Constraints in Optimal Material Distribution," in *AIAA/USAF/NASA/ISSMO Symposium on Multidisciplinary Analysis and Optimization*, St. Louis, pp. 1501–1510.
- [102] HAUG, E. J., K. K. CHOI, and V. KOMKOV (1986) *Design Sensitivity Analysis of Structural Systems*, Academic Press, Inc., Orlando, FL.



- [103] SVANBERG, K. (1987) “The Method of Moving Asymptotes: A New Method for Structural Optimization,” *International Journal of Numerical Methods in Engineering*, **24**(2), pp. 359–373.
- [104] SIGMUND, O. and J. PETERSSON (1998) “Numerical Instabilities in Topology Optimization: A Survey on Procedures Dealing with Checkerboard, Mesh-independancies and Local Minima,” *Structural Optimization*, **16**, pp. 68–75.
- [105] SIGMUND, O. (2007) “Morphology-based Black and White Filters for Topology Optimization,” *Structural and Multidisciplinary Optimization*, **33**, pp. 401–424.
- [106] GUEST, J., J. PREVOST, and T. BELYTSCHKO (2004) “Achieving Minimum Length Scale in Topology Optimization using Nodal Design Variables and Projection Functions,” *International Journal of Numerical Methods in Engineering*, **61**(2), pp. 238–254.
- [107] STORN, R. and K. PRICE (1997) “Differential Evolution – A Simple and Efficient Heuristic for Global Optimization over Continuous Spaces,” *Journal of Global Optimization*, **11**, pp. 341–359.
- [108] ANANDALINGAM, G. and T. FRIESZ (1992) “Hierarchical Optimization: An Introduction,” *Annals of Operations Research*, **34**, pp. 1–11.
- [109] LIBOVE, C. and S. B. BATDORF (1948) *A Generalized Small Deflection Theory for Flat Sandwich Plates*, Tech. Rep. 899, NACA Report.

## **Vita**

### **Vipul Mehta**

Vipul Mehta was born in Pune, India. He received his Bachelor's and Master's degree in Mechanical Engineering from Indian Institute of Technology, Bombay at Mumbai, India. He joined Penn State University in Fall 2005 to pursue a Ph. D. in Mechanical Engineering. He will be working with Intel Corp. in Chandler, AZ after completion of his degree.